Numerical Simulation of Transient Performance of Viscous Micropumps

By

Mohamed Omar Abdelgawad

A Thesis

in the Department of

Mechanical and Industrial Engineering

Presented in Partial Fulfillment of the Requirements

for the Degree of Master of Applied Science at

Concordia University

Montreal, Quebec, Canada

August 2003

National Library
of Canada

Acquisitions and
Bibliographic Services

395 Wellington Street
Ottawa ON K1A 0N4
Canada

Bibliothèque nationale
du Canada

Acquisisitons et
services bibliographiques

395, rue Wellington
Ottawa ON K1A 0N4
Canada

Your file Votre référence
ISBN: 0-612-83879-X
Our file Notre référence
ISBN: 0-612-83879-X

ABSTRACT

Numerical Simulation of Transient Performance of Viscous Micropumps

Mohamed Omar Abdelgawad

The current trend in today's technology is the miniaturization of the mechanical components to the extent that they are about to compete with the electronics used to control their performance. In the present study, the transient performance of viscous micropumps will be investigated numerically. The viscous micropump operation depends mainly on viscous forces, and can operate in any situation where viscous forces are dominant. It consists of a cylinder placed eccentrically inside a microchannel with its axis perpendicular to the channel axis. When the cylinder rotates, a net force is transferred to the fluid due to the unequal shear stresses on the upper and lower surfaces of the cylinder, thus causing the fluid to displace.

The effect of the microchannel height, rotor eccentricity, Reynolds number, and pump load on the transient performance of the viscous micropump has been studied in detail. The rotor eccentricity was determined to be the parameter that affected the transient performance of the micropump the most significantly. Multi rotor configurations were also examined and proved to enhance the micropump performance. The steady state performance was compared with the available experimental data and was found to be in a very good agreement. This work provides a foundation for future research on the subject of fluid phenomena in viscous micropumps.

Table of contents

List of figures.....vi

List of tables.....x

Nomenclature.....xi

1 Introduction.....1

2 Literature review.....6

2.1 Viscous micropumps.....6

2.2 Viscous microturbines.....10

2.3 Nature of flow around immersed bodies.....11

2.3.1 Flow around cylinders.....11

2.3.2 Flow around spheres.....27

2.3.3 Flow around square cylinders.....31

2.4 Objectives.....34

3 Mathematical modeling and numerical solution.....36

3.1 Pump geometry and flow parameters.....36

3.2 Governing equations and boundary conditions.....39

3.3 Numerical solution.....40

3.3.1 Grid independence.....42

3.3.2 Convergence.....50

3.3.3 Time step size.....52

4 Single-rotor viscous micropump.....56

4.1 Comparison with previous results.....56

4.2 Effect of micropump channel height.....58

4.3 Effect of rotor eccentricity....76
4.4 Effect of Reynolds number....93
4.5 Effect of pump load....101
5 Multi-rotor viscous micropump....111
5.1 Dual horizontal rotor....111
5.2 Triple horizontal rotor....121
5.3 Dual vertical rotor....124
5.3.1 Symmetrical dual vertical rotor viscous micropump....128
5.3.2 8-shaped dual vertical rotor viscous micropump....135
6 Conclusion and future directions....143
6.1 Conclusion....143
6.2 Future directions....145
References....149
Appendix....152

List of Figures

Figure 3.1: Schematic of the micropump geometry...37

Figure 3.2: Different meshes used for the grid dependence test..............................45

Figure 3.3: X-Velocity on plane $x^* = 9$ on different meshes.................................46

Figure 3.4: X-Velocity on plane $x^* = 9$ on different meshes.................................47

Figure 3.5: Change of the drag coefficient with time on different meshes.................48

Figure 3.6: Variation of the drag coefficient with time on different meshes................49

Figure 3.7: Effect of residuals on the change of u^* with time...............................53

Figure 3.8: Effect of time step size on the change of u^* with time.........................55

Figure 4.1:. Comparison of average velocity vs. channel height.............................57

Figure 4.2: Comparison of average velocity vs. eccentricity at $\Delta P^* = 1$and Re = 1.......58

Figure 4.3: Flow rate vs. pump load at Re = 0.5 and $\in = 0.9$.................................60

Figure 4.4: Start-up operation for different channel heights..................................61

Figure 4.5: Change of time constant with increasing channel height........................63

Figure 4.6: Steady state stream lines at different channel heights...........................64

Figure 4.7: Stream lines at different times (S = 1.5, $\in = 0.95$, $\Delta P^* = 0$, Re = 1)...........65

Figure 4.8: Pressure contours (S = 2.5, $\in = 0.95$, $\Delta P^* = 0$, Re = 1)...........................66

Figure 4.9: Pressure distribution on cylinder surface at different channel heights.........68

Figure 4.10: Change of drag coefficient with time at different channel heights............69

Figure 4.11: Shear stress distribution on cylinder surface at different S.....................71

Figure 4.12: u-velocity distribution at $x^* = 8$ for different channel heights.................72

Figure 4.13: Lift coefficient vs. time at different channel heights...........................73

Figure 4.14: Moment coefficient vs. time at different channel heights......................75

Figure 4.15: Pumping efficiency development with time at different S....................77

Figure 4.16: Average velocity vs. time at different rotor eccentricities....................79

Figure 4.17: Steady state streamlines at different eccentricities..............................80

Figure 4.18: Streamlines at different times (S = 3, $\in = 0.6$, $\Delta P^* = 0$, Re = 1)..............82

Figure 4.19: Drag coefficient vs. time at different eccentricities...........................83

Figure 4.20: Viscous, pressure and total drag coefficient for $\in = 0.4$.......................85

Figure 4.21: Pressure distribution on cylinder surface at different times and $\in = 0.4$....86

Figure 4.22: Change of lift coefficient with time at different eccentricities...............88

Figure 4.23: Moment coefficient vs. time at different eccentricities.......................90

Figure 4.24: Shear stress distribution on cylinder surface at different eccentricities......91

Figure 4.25: Pumping efficiency at different eccentricities...................................92

Figure 4.26: Streamlines at different Reynolds numbers......................................94

Figure 4.27: Average velocity inside the channel vs time at different Re....................96

Figure 4.28: Streamlines at different times for Re = 50.......................................97

Figure 4.29: Moment coefficient vs. time at different Reynolds numbers.....................99

Figure 4.30: Efficiency development with time at different Reynolds numbers..........100

Figure 4.31: Average velocity vs. time at different backpressures...........................102

Figure 4.32: Streamlines at different backpressures..103

Figure 4.33: Pressure distribution on cylinder surface at different backpressures........106

Figure 4.34: Shear stress on cylinder surface at different backpressures..................107

Figure 4.35: Efficiency vs. time at different backpressures..................................108

Figure 4.36: Efficiency vs. backpressure at different eccentricities........................110

Figure 5.1: Mesh used for the dual rotor viscous micropump..............................113

Figure 5.2: Average velocity inside the micropump at different rotor spacing..............114

Figure 5.3: Streamlines at different λ ($S = 1.5$, $\in = 0.95$, $P = 10$, $Re = 1$)..................115

Figure 5.4: Streamlines at different times at $\lambda = 0.5$..117

Figure 5.5: Drag coefficient on rotors 1 and 2 at different λ....................................118

Figure 5.6: Moment coefficient on each rotor at $\lambda = 0.5$....................................119

Figure 5.7: Total moment coefficient at different L..120

Figure 5.8: Effeciency at different rotor spacing for the dual...............................122

Figure 5.9: Streamlines for single, dual and triple rotor micropump at $\lambda = 2$.............123

Figure 5.10: Effect of rotor spacing λ on total moment coefficient.........................125

Figure 5.11: u* vs backpressure for single, dual and triple rotor micropump.............126

Figure 5.12: The two configurations used in the vertical rotor viscous micropump......127

Figure 5.13: Streamlines inside the symmetrical vertical rotor pump at different t^*......129

Figure 5.14: Average velocity vs time for the symmetrical vertical rotor pump..........130

Figure 5.15: Drag coefficient on each rotor compared to the single rotor..................131

Figure 5.16: Total moment coefficient on rotors at different eccentricities...............133

Figure 5.17: Efficiency vs time at different eccentricities...................................134

Figure 5.18: Streamlines in the 8-shaped dual vertical rotor micropump.................136

Figure 5.19: Shear stress distribution on lower and upper.................................137

Figure 5.20: Moment coefficient on lower and upper rotors................................138

Figure 5.21: Efficiency for symmetrical and 8-shaed dual vertical rotor pump...........140

Figure 5.22: P^*-Q curves for all tested multi-rotor micropumps............................141

Figure 5.23: Efficiency of all tested multi-rotor micropumps..............................142

Figure A.1: V-velocity component on the horizontal centre line...........................154

Figure A.2: U-velocity on the vertical centre line..154

Figure A.3: Mesh of the constriction part in the pipe..155

Figure A.4: Stream lines near the constriction (drawing not to scale)..........................156

Figure A.5: Mesh of the constriction part in the pipe..159

Figure A.6: Stream lines near the constriction...159

List of tables

Table 3.1: Properties of different grids used..44

Table 3.2: The variation of the fluid average velocity with grid size..........................51

Table A.1: Experimental and analytical values of the separation and re-attachment distances..158

Nomenclature

C_D	Cylinder drag coefficient
C_L	Cylinder lift coefficient
C_M	Cylinder moment coefficient
d	Cylinder diameter, (m)
F_L	Lift force on cylinder, (N)
F_D	Drag force on cylinder, (N)
h	Channel height, (m)
M	Moment on cylinder, (N.m)
$\dot{m}$	Pump mass flow rate, (kg/s)
P_{in}	Pump inlet pressure, (Pa)
P_{out}	Pump outlet pressure, (Pa)
P^*	Non-dimensional pressure
ΔP	Pump pressure rise, (Pa)
$\Delta P*$	Non-dimensional pressure rise, ($\Delta P^* = \frac{P_{out} - P_{in}}{\frac{\rho \nu^2}{d^2}}$)
Q	Non-dimensional volume flow rate, ($Q = u^* S$)
Re	Reynolds number, ($\mathrm{Re} = \frac{\omega d^2}{2 \nu}$)
rms	Root mean square value
R	Computations residuals
S	Non-dimensional channel height, ($S = \frac{h}{d}$)
t	Time, (s)

t^*	Non-dimensional time, ($t^* = \frac{t}{\frac{2\pi}{\omega}} = \frac{t\,\omega}{2\pi}$)
Δt	Time step size, (s)
$\bar{u}$	Average velocity inside micropump, (m/s)
u^*	Non-dimensional average velocity, ($u^* = \frac{2u}{\omega d}$)
U	Cylinder surface velocity, (m/s)
$\vec{V}$	Fluid velocity vector, (m/s)
y_c	Distance from channel axis to cylinder center, (m)

GREEK LETTERS

α	Body forces per unit mass, (m/s^2)
$\in$	Cylinder eccentricity, ($\in = \frac{y_c}{\frac{h}{2} - \frac{d}{2}}$)
η	Pump efficiency, ($\eta = \frac{\Delta P^* u^* S}{C_m \mathrm{Re}^2}$)
μ	Fluid dynamic viscosity, (Pa.s)
ν	Fluid kinematic viscosity, (m^2/s)
ρ	Fluid density, (kg/m^3)
τ	Fluid shear stress, (Pa)
τ^*	Non-dimensional fluid shear stress, ($\tau^* = \frac{\tau}{\frac{\rho\,\nu^2}{d^2}}$)
ω	Cylinder angular velocity

Chapter I

Introduction

In the last decade, technology has provided us with several kinds of mini and micro machines that found their way into our daily life applications. These micro machines include micropumps, micro sensors and actuators and different other types of micro machines. These devices are called MEMS which stands for Micro Electro Mechanical Systems. The key advantage of MEMS, in addition to their small size, and hence practicality, is the great reduction in the manufacturing costs due to the mass production methods used.

Micropumps are among the most developed of all MEMS devices, and have already been implemented into the mainstream. For example, micropumps are used in ink jet printers to inject ink droplets, and as well as in fuel injector applications. Micropumps operate on completely different principles than those applied in traditional pumps like the axial or centrifugal pumps. Micro dimensions limit the effect of centrifugal forces and inertia forces in general, and the large surface-to-volume ratio amplifies the effect of viscous forces, rendering it the dominant force at the micro scale. According to the types of fluids used and ranges of flowrates in most micropumps, Reynolds number is basically in the range of 1:100, which means that the flow is always laminar (Nguyen et al., 2002). Positive displacement pumping is the most prevalent method used in micropumps, yet more than one principle is used to generate the force required for the pumping stroke. Thermo-pneumatic, piezo-electrical, and electrostatic actuations are just examples of the actuation methods used (Mastrangelo and Becker, 2001). In Thermo-pneumatic, the micropump diaphragm is operated by the sequential expansion and contraction of a small volume of air inside the micropump. This expansion and contraction are the result of the continuous heating and cooling of the trapped air. Piezo-electric actuation is one of the most commonly used actuation methods in positive displacement pumping. It operates on the special properties of some material to deform mechanically when they are subjected to voltage difference. Piezo-electricity provides fast response, relatively large actuation force and big stroke volume. On the other side, it requires high actuation voltage and a precise mounting inside the micropump. Electrostatic actuation depends on the force applied by an electric field on an electrically charged plat inside the pump. Electrostatic actuation is characterized by a very fast response that allows operation at high frequencies.

The problem with positive displacement micropumps is that they usually require check valves at the inlet and outlet ports. This adds to the complexity of design especially on such a small scale. Moreover, these check valves, being very small in size, are prone to wear and blockage by any impurities in the working fluid. To overcome this problem, in some designs, check valves were replaced by a nozzle at the inlet, and a diffuser at the exit (Nguyen et al., 2002). Yet, the idea is not practical since in order to operate properly, certain operating conditions are required, which do not apply at all the time.

Various other pumping ideas were proposed to overcome the valve problem associated with positive displacement pumps. Electrohydrodynamic pumps use Coulomb force to drive the fluid inside the channel. Dielectric fluids with induced charges at the fluid-solid interface are forced to displace due to a moving electric field sweeping through the fluid. Electrokinetic pumping, similar to electrohydrodynamic pumps, uses the moving electric field to displace the fluid. Yet, instead of introducing electrical charges in a dielectric fluid, charged ions in an electrolytes or in the electric double layer of the fluid are used. The liquid ions drag the rest of the fluid with it due to the viscosity, and hence the fluid moves with nearly a uniform velocity profile.

Sequential generation of thermal bubbles was also used to force liquids through microchannels (Kim et al., 2000). A bubble is first introduced to function as a check valve to prevent the fluid from moving backward. Afterwards, another heater generates an additional bubble, which grows in the opposite direction of the first bubble, pumping the liquid in the desired direction. The last heater generates a third bubble to push the fluid more and then to act as a check valve to prevent the liquid from flowing backward when the first and middle bubbles collapse to allow for more liquid to fill the pumping section. The process is then repeated by turning the heaters on and off to generate a continuous flow. The idea of using bubble generation as a pumping method was also mentioned by Beatty (1996) and Lin (1998).

Gear pumps were also mentioned by Dopper et al. (1997) as a possible method for dosing of very small flowrates. They manufactured a micro gear pump with gears of 596 μm diameter and reported the flowrate and pressure at different rotational speeds of the gears. They could achieve flowrates up to 1 ml/min and pressures up to 1200 hPa.

To summarize, many pumping techniques that may sound very unfamiliar, yet operable, were suggested in the last few decades to fill in the huge demand of micropumps required by the new MEMS industry. Yet, all the micropump concepts mentioned above, although applicable, are complex, expensive and involve the use of different auxiliary components in order to make the fluid environment suitable for pumping action to occur.

The viscous micropump, first introduced by Sen et al. (1996) incorporates both applicability at the micro scale and simplicity in design. The viscous micropump is simply a cylinder placed eccentrically inside a channel with its axis perpendicular to the channel axis. When the cylinder rotates, a net force is transferred to the fluid due to the unequal shear rates on the upper and lower surfaces of the cylinder, thus forcing the fluid to displace. Its operation depends mainly on viscous forces, and can operate in any application where viscous forces are dominant. This application would incorporate either low viscosity liquids in micro passages, due to the high surface-to-volume ratio characteristic of MEMS, or highly viscous liquids, such as heavy polymers, in macro ducts. Sen et al. performed an experiment to test the pump performance. The study focused on the effect of the channel height, rotor eccentricity, and angular velocity on the pump performance and on the fluid bulk velocity in the duct.

In later studies, the same research team performed a numerical simulation of the viscous micropump solving Navier-Stokes equations for the case of the cylindrical rotor (Sharatchandra et al., 1997; Sharatchandra et al., 1998; Decourtye et al., 1998). Critical values for optimum performance were calculated. Moreover, they studied the thermal effect of the viscous dissipation and included temperature dependent viscosity. They also included three-dimensional effects by introducing channel sides. The idea of the viscous microturbine as the reverse of the viscous micropump was also introduced yet, just as an idea without a complete study of all the parameters that affect its performance.

The present work will extend the previous studies mentioned above to account for the transient performance of the viscous micropump. The time required for the micropump to reach steady state, the time dependence of the drag and lift forces, and the viscous resisting torque on the cylinder will be computed. The pressure distribution on the cylinder surface will be also included in the study. As an indicator of the overall performance of the micropump, the efficiency will be reported for different geometries and operating conditions.

In order to increase the capabilities of the viscous micropump, dual and triple rotor viscous micropumps will also be tested. The rotors will be placed either horizontally or vertically relative to each other in order to find the orientation that provides the best performance. The flowrate-load curves will be plotted as well as the efficiency curves in order to find the percentage improvement for the multi-rotor micropump relative to the single-rotor one. It is believed that the present work will provide a good contribution to the study of viscous micropumps and will help giving a good idea about the feasibility of introducing them into commercial applications in the near future.

Chapter II

Literature review

2.1 Viscous micropumps

The idea of viscous micropumps started when Sen et al. (1996) suggested a new idea for pumping liquids in MEMS applications. They suggested using a cylinder (or generally speaking, a body) eccentrically placed inside channel to be used for pumping liquids under low Reynolds numbers. This would be the case for either low viscosity liquids in micro passages, such as in MEMS, or for highly viscous liquids, such as heavy polymers, in macro ducts. The reason, for which they suggested such pump, was the difficulties associated with ordinary pumping methods when used in micro scale. There are mainly three categories of pumps; each one depends in its operation on a unique principle, which is associated with some problems when applied in micro scale. The first category, positive displacement pumps, operates through forcing the liquid out of a closed space whose volume is decreasing (due to the action of a piston for example) or the interaction of two moving (or rotating) bodies. This type, though very effective, is not suitable for micro applications because it involves the fabrication of much smaller valves and ports which are also prone to wear and clogging through their operation. The second category, centrifugal pumps, depends on the transformation of the high kinetic energy, gained by the fluid through being accelerated radially in the impeller, to pressure energy in the diffuser. This principle is no longer effective in micro scale where the inertia effects are negligible. The third category, axial pumps, requires the motor to be immersed in the flow inside the channel or the use of a gearing system, which will complicate the configuration more, especially at such small scale. The solution Mihir et al suggested was the continuous transverse axis viscous pump, as they call it, which depends on viscous forces, developed by the rotation of a body placed eccentrically in the duct and driven from outside, in pushing the liquid through the duct.

An experiment was carried out to test the performance of this new pump. They used rotors of different shapes such as, cylinders of 0.898 cm diameter, square cylinders of 0.898 cm diagonal and rectangular cylinders of 0.898 cm x 0.1 cm cross section. The study included the effect of the channel height, rotor eccentricity and angular velocity on the pump performance and on the fluid bulk velocity in the duct. The flow pattern in the duct was also observed and two unique patterns were spotted depending on the gap between the rotor and the channel walls. When the gap between the rotor and the wall is relatively large, a single secondary vortex just above the rotor exists, while two small co-rotating vortices are observed for smaller gaps. In their experiment, the bulk velocity of the liquid was found to be proportional (approximately linearly) to the rotor surface speed. Bulk velocities in the order of about 10% of the rotor surface speed were measured. The velocity profile inside the duct was found to be nearly parabolic except for the sections near the rotor where it was found to deviate from this profile because of the existence of the rotor.

In a trial to get more information about this pump and the parameters that affect the performance, the same research team (Sharatchandra et al., 1997) made a numerical simulation of such pump solving Navier-Stokes equations for the case of the cylindrical rotor. In this study, it was possible to introduce new parameters and see how they are going to affect the flow and to change the values of existing parameters, which was not possible before because of the experimental difficulties. The parameters they tested, which are channel height, eccentricity, applied load and Reynolds number, were varied over wide range and the corresponding performance of the pump was depicted. Critical values for optimum performance were also calculated. The highest bulk velocity was achieved when the plates spacing is around one and half times the cylinder diameter for a fixed eccentricity and at the maximum eccentricity for a fixed plates spacing. The load-flowrate curve for the pump was also drawn with a part of it in the negative part of the flow rate axis, showing that the flow will change its direction if the load is increased beyond the pump capability. The maximum efficiency of the pump was found to be around 2.5 % for the optimum plate spacing. This very low efficiency is due to the high rates of viscous dissipation in the flow. A decrease in the bulk velocity was depicted when the slip boundary conditions were introduced as a result of the reduced traction of the fluid at the rotor surface. Of course the drag on the plate surfaces was reduced as well, but its effect did not make up for the reduction in traction at the rotor surface.

In order to make a complete study that includes all the parameters that affects the performance of the pump, the same research group expanded their efforts to cover the effect of viscous dissipation and temperature variation in the flow field and the three-dimensional aspects of the flow (Sharatchandra et al., 1998 and Decourtye et al., 1998). They noticed that the viscous dissipation might cause a significant temperature rise since viscous forces are the driving forces. In order to check the effect of viscosity on the temperature they solved the momentum equation with viscosity depending on the temperature and the energy equation with viscous dissipation terms retained all coupled together. Different types of thermal boundary conditions at the fluid-rotor interface were studied to check their effect on the pumping process. It was found that viscous dissipation could really cause significant temperature rise in the fluid temperature. A rise in temperature as much as 30 °C was calculated near the rotor where the shear stresses are maximum. Steep temperature gradients were calculated in the same region as well. They concluded that, in certain cases, neglecting the viscous dissipation effects would give inaccurate results about pump performance. When the three-dimensional effects were introduced through considering the effect of the side walls of the channel, the pump performance was, naturally, found to decrease in terms of bulk velocity, yet pumping action existed even for channel widths less than the rotor diameter. The sidewall effect was found also to reduce the channel height corresponding to maximum bulk velocity as well as increasing the backpressure at which back flow occurs. It has to be mentioned that there was some trials to apply the lubrication approximation for the viscous micropump. Day et al. (2000), studied the viscous micropump using the lubrication analysis and proved that this approximation is valid when the upper and lower gap size is small compared to the cylinder diameter. He reported that there is an optimum gap ratio for the maximum flowrate inside the micropump.

All the previously mentioned studies did not consider the unsteady performance of the viscous micropump although it is believed that the time dependence of the viscous micropump operation is of great importance. It has been mentioned that one of the most prominent applications for the viscous micropump is the drug dosing of minute amounts of drugs. In such a very sensitive application where any drop of liquid counts, the start up operation of the micropump is of great importance. Moreover, understanding the unsteady operation of the viscous micropump will, for sure, increase the understanding of its unique method of pumping. Consequently, this will help discover the best operating conditions which guarantee the most efficient operation.

The use of more than one rotor is also expected to enhance the performance of the viscous micropump in terms of the flowrate and pumping pressure. Using more than one rotor is analogous to connecting more than one pump either in series or in parallel depending on the relative orientation of the rotors relative to each other. The expected increase in the flowrate or the pressure will provide more flexibility to the number of application of the viscous micropump.

2.2 Viscous microturbines

The performance of the viscous micropump attracted the attention to investigate the validity of the same idea but in the opposite manner, i.e. as a turbine. In the last work published about viscous micropumps (Decourtye et al., 1998), the reverse performance of the micropump as a microturbine was investigated. It was found that a net torque could be generated by a bulk viscous flow around a cylinder eccentrically placed inside a duct. Rotor surface velocities as much as 0.37 of the bulk velocity of the fluid inside the channel was calculated. The turbine load was symbolized by a resisting torque on the rotor and the characteristic curve for the rotor angular velocity against turbine load was plotted and found to be linear as the case in the characteristic curve of the pump load against the rotor angular velocity. The three-dimensional effects in the turbine case were also investigated and showed that the sidewalls effect was to reduce the rotor speed for the same bulk velocity in the channel.

Although, the idea of the viscous pump was validated to work in the opposite sense as a turbine, not enough investigation was performed to get a better idea of its performance under different conditions. For example, it is not known whether the rotor motion will be steady or oscillatory as well as the direction of such rotation. Also, the effect of changing the geometrical parameters of the rotors and the boundaries such as channel height and rotor eccentricity need to be explored. Many other parameters and effects need to be studied in order to have a broader idea about the turbine capabilities and hence choosing the appropriate applications which suits these capabilities together with discovering the methods of assuring a reliable and efficient performance.

2.3 Nature of flow around immersed bodies

In order to be able to study the different parameters, which govern the flow in viscous micro pumps and turbines, the characteristics of flow around immersed bodies should be well understood. Many studies exist in the literature about flow around fixed, rotating or free to rotate immersed bodies. This includes both streamlined bodies such as cylinders and spheres and blunt bodies such as square and triangular cylinders. There are even some studies about the flow around non-uniform bodies generally like the study done by Hsu and Ganatos, (1989). Each shape has its own characteristics and governing parameters. This will be thoroughly discussed in the next few sections.

2.3.1 Flow around cylinders

Flow around a solid cylinder is one of the classical problems of fluid mechanics, which attracted much of the interest of researchers. Nearly all the parameters that govern the flow field together with the characteristics of the flow under different conditions were examined and still more studies are being done. Of these studies, Dennis et al. (1970) analyzed steady flow past a circular cylinder at Reynolds numbers up to 100. They used the Vorticity-Stream function model, with modified polar co-ordinates (ξ, θ) where

$\xi = \log r$, to solve the two dimensional Navier-Stokes equations. Oseen's assumption for the linearization of the inertia terms in the equations was also used to simplify the problem. Changing the Reynolds number between 5 - 100, it was found that the wake length L from the cylinder rear to the end of separation region increases nearly linearly with Reynolds number. This was an extension to the former results of Takami and Keller (1969) who found the same linear relation between Re and the wake length till Re = 60 which was the limit of their study. This was different from the results obtained by Kawaguti and Jain (1969) who reported deviation from the linear relation after $\mathrm{Re} = 20$. Yet, Kawaguti used a relatively coarse grid in the θ direction ($\Delta\theta = \pi / 30$), which might have led to inaccurate results. As a test for the effect of the grid size ($\Delta\theta$) on the results, Dennis used ($\Delta\theta = \pi / 40$) for Re = 100 and found that L reached a steady limit of 11 diameters and that the vortex pair had become very fat and distorted. When the grid size was reduced to ($\Delta\theta = \pi / 60$), the wake length L was found to be only 6.5 diameters which indicates that the mesh size used by Kawaguti was not small enough to get accurate results. Separation of the flow was found to start from $\mathrm{Re} = 7$ with a separation angle (θ_s) of 15.9° measured counter clockwise from the rear of the cylinder. The values of (θ_s) was calculated for all the values of Re and was found to be in excellent agreement with the calculations of Takami & Keller. The drag coefficient was calculated for all values of Re and was found to decrease as Re increase as expected. The maximum drag coefficient was found to be $C_D = 4.116$ corresponding to Re = 5 and the minimum was found to be $C_D = 1.056$ for Re = 100. The pressure coefficient Cp on the cylinder surface was also calculated for all values of Re. Of course, its maximum value was at the front stagnation point and this maximum value increased as Re decreases. On the cylinder rear surface, where the pressure coefficient is negative, the situation was reversed, as decreasing Re was found to decrease the pressure coefficient. A point of minimum value for C_P existed on the cylinder surface and it was found to shift upstream as Re is increased.

This work reported by Dennis covered the characteristics of the steady flow field around a cylinder for Re up to 100. In their work, Jordan et al. (1972) studied the problem of unsteady flow around a cylinder and extended the Reynolds number range from $\mathrm{Re} = 40$ to $\mathrm{Re} = 1000$, in which, the flow was found to experience a totally different behavior than it is for low Reynolds numbers. All the important parameters in the flow, such as the lift, drag and the torque on the cylinder surface, were found to become oscillatory in nature as a Von Karman vortex street develops. In order to make sure that Von Karman vortex street is formed, the flow was perturbed early in the beginning through an impulsive counterclockwise rotation of the cylinder followed by another clockwise one after which the cylinder was stopped again.

In his work, Stanley, used the Vorticity-Stream function model to solve the 2-D flow. The Log Polar co-ordinates system was used in order to take advantage of the nature of this type of co-ordinates, which pertains nearly the same form of equations as in rectangular co-ordinates. An additional advantage is that, the log-polar co-ordinates will make the mish finer close to the cylinder surface, where most of the gradients exist, which would of course increase the accuracy of the calculations.

When it comes to the results, the perturbations introduced too early in the flow totally changed the flow characteristics even though the cylinder was brought to stop again. The vortex street caused permanent oscillations in the drag, lift and torque coefficients. For example, the drag coefficient was found to rapidly decay with time till the perturbations were introduced at $t^* = 4$ ($t^* = \frac{t\,u}{a}$) after which the drag coefficient was found to oscillate with an average value much higher than the expected value for a steady flow at the same Re. Before the flow begins to oscillate, the stagnation streamline is horizontal and dividing the flow into two halves, one passing above and the other passing below the cylinder. Yet, when the cylinder is oscillating, the stagnation streamline starts to oscillate at half the Strouhal frequency indicating unequal flows above and below the cylinder. The separation angle of the flow suffers strong oscillations at the beginning till $t^* = 20$, after which the flow develops into a regular pattern of oscillations with average $\theta_s = 63°, 75°, 88°$ and oscillations of 3°, 8°, 7° for Re = 100, 400, 1000 respectively. The amount of drag, lift and torque oscillations as well as Strouhal number were found to depend on Re with Strouhal number increasing when Re increases.

When compared with experimental results, Stanley found that the computed drag coefficient at low Reynolds numbers was a bit lower than that reported from experiments. The opposite is present at high Reynolds number where the computed drag was higher than the experimental drag. The calculated Strouhal number is nearly the same as the experimental one at Re = 100 while small differences appear at high Re. Stanley referred this discrepancies between experimental results and the computed results to the fact that the flow past a cylinder is 3-D in nature at Re > 200 due to the generated turbulence. Yet, Stanley suggests that if Re < 400, the vortex street is only partially turbulent and the flow near the cylinder is nearly laminar. As a result of this, the presented results are accurate in describing the flow in the range of $100 < \mathrm{Re} < 400$ but not as much accurate for $\mathrm{Re} = 1000$.

In order to further gain more knowledge about the nature of flow around cylinders, many studies investigated the problem of uniform flow past a cylinder, which is forced to rotate with a certain angular velocity. Of course, such a flow will experience some differences from the flow past a fixed cylinder in terms of the drag, lift and torque coefficients and pressure distribution on the cylinder surface. For example, the lift coefficient will, certainly, be affected by the Magnus effect resulting from the cylinder rotation. The pressure distribution will also change as a result of the change that will happen both in the place of the stagnation and separation points. Also, the fluid will exert a net moment on the cylinder. Kimura et al. (1991) studied the wake behind a rotating cylinder in a linear flow. They found that when the spin parameter becomes large, the shedding in the wake becomes smaller amplitude wile the frequency of vortex shedding becomes large. They also reported the disappearance of the vortex street at some values of the spin parameter. This value of the spin parameter decreases with increasing Reynolds number. Badr and Dennis (1985) studied the flow past a rotating cylinder in which, the flow and rotation are started impulsively from rest. In this work, the flow was governed by two parameters which are Reynolds number (Re) and the dimensionless rotation α, where $\alpha = \frac{\omega u}{a}$, instead of depending on Re only. The calculations were confined to Re = 200, 500 and small rotation rates of $\alpha = 0.5, 1$. The Vorticity-Stream function model was used again in the analysis with the same log polar co-ordinate system which suites this flow geometry. The results obtained by their method showed excellent agreement with the experimental data available for Re = 200, such as that of Coutanceau and Menard (1985). This was very clear when the graphs they presented are compared with flow visualization pictures from the experimental work at the same conditions. Badr and Dennis described accurately the sequence of the formation of the vortex street downstream of the cylinder. In the case of Re = 200 and α = 0.5, the sequence of formation of the vortices is as follows; first a vortex is formed above the x-axis, then a second one is formed just below the x-axis. They both continue to grow till the first one detaches from the cylinder and is convected down stream from the cylinder. The second vortex continues to grow and is detached from the cylinder when two new vortices are formed above and below the x-axis. These two new vortices collapse into one vortex and then a new vortex is formed again below the x-axis. This was the time limit at which they terminated the calculations. When the rotation speed was increased to $\alpha = 1$, the vortices formation is a little different. No second vortex is formed even after the first one is detached from the cylinder and convected down stream. Then two new vortices are formed above the x-axis. The one nearest to the x-axis is then detached and moved down stream and another one is formed around the x-axis zone. This newly formed vortex together with the old one, which is still attached to the cylinder surface, are collapsed together and detached from the cylinder surface as one vortex. When the total drag coefficient (i.e. drag due to both pressure force and friction force) was plotted versus time, it was found to first decrease and then increase again but not to the first value it started from. The friction drag coefficient was found to decrease constantly with time to reach a constant steady state value at the end. The lift coefficient was found to increase constantly with time along the whole time length of the calculations and it was found to be proportional to the rotation parameter α. The torque coefficient was found to decrease, nearly inversely with time, along the time length of calculations. In all the cases studied there was only one stagnation point on the upstream face of the cylinder above the x-axis. This stagnation point, after reaching its place early when the flow starts, remains nearly stationary in its position with time.

In another study by, by Badr (1990) the range of Reynolds number, for which the flow was calculated, was raised to be between Re = 10^3 - 10^4, also the rotation speed α was increased to 3. This time, instead of making a numerical simulation only, the flow was investigated both experimentally and numerically and the results were compared together. For the numerical simulation, the Vorticity-Stream function model was used again with the log-polar co-ordinate system and the analysis is the same as the previous work done by Badr and Dennis (1985). For the experimental study, the motion of a cylinder (two cylinders were tested, 4 cm and 6 cm in diameter) moving and rotating simultaneously in a vertical tank, 46 x 56 cm in cross section and 1 m high, was visualized using a small solid plastic tracer particles of Rilson powder and photographed at pre-selected time intervals using a camera moving with the cylinder. The cylinder moved midway in the tank to simulate the infinite medium as much as possible and the clearance at its ends was reduced as much as possible to minimize the end effects.

One of the effects of the increase in Re to 10^3 was the formation of many secondary vortices attached to the larger ones at the cylinder downstream surface at all rotational velocities compared to the cases of smaller Re. The flow had a periodic nature associated with the vortex-shedding phenomenon. This is clear from the streamline patterns, which repeat themselves on intervals. This periodic nature of the flow caused both the lift and drag coefficients C_D & C_L to oscillate with time at low rotational rates. When α was increased to 3, the experimental results and numerical simulation show some discrepancies. The numerical simulation shows that the periodic flow pattern does not develop. At the beginning some vortices are formed but later the flow reaches a steady state. Consequently, the lift and drag coefficients oscillate at the beginning and then start to increase constantly with time till the steady state flow is reached. On the other hand, the experimental results, although showing good agreement with the numerical simulation for the early stages, show that the flow soon becomes turbulent, which leaves no place for any comparison with the numerical simulation.

At the end of his work, Badr, made the calculations again using the boundary layer approximation, which is associated with high Reynolds numbers. When the results of such simulation were compared to these of the solution of Navier-Stokes equations, it was found that they give totally misleading information. For example, the lift coefficient was totally in the wrong direction, which is due to the fact that the boundary layer calculations for the lift coefficient includes only the lift due to the skin friction and neglect that due to the pressure. Of course, the latter has the dominant effect in the present case. Also the drag coefficient calculations showed inconsistency with the results of solving Navier-Stokes equations. It is, thus, concluded that the boundary layer approximation will not give accurate results unless the pressure effect is considered in the calculations.

The behavior of the flow around cylinders, whether fixed or rotating, will certainly change if the flow field outside the cylinder is bounded by other boundaries. Some studies have investigated the flow around circular cylinders near a plane boundary or inside a duct. Of these studies, Liang et al. (1995) analyzed the flow field around a rotating cylinder near a plane boundary. Using the penalty finite element method, they solved Navier-Stokes equations for two-dimensional incompressible flow. They investigated the flow field around the cylinder for various rotational speeds and distances from the wall ranging from zero to 4.5 cylinder diameters. In each case, the pressure distribution and lift, drag and torque coefficients are calculated. They assumed the no slip boundary conditions, which means the fluid acquiring the cylinder velocity at its surface and assumed a parabolic velocity distribution at the upstream inlet eight diameters away from the cylinder. The used models were validated by comparing the results obtained for some cases with the corresponding results of Badr et al. (1990) and Ingham et al. (1983). The comparison showed good agreement with the validation models except with the maximum vorticity on the cylinder surface, which showed some small differences. In their work, they studied four cases, when the gap is more than one diameter with and without rotation and when it is less than one diameter with and without rotation.

The first case studied was a cylinder without rotation, a gap greater than one diameter and Re = 20. In this case, reducing the gap size would result in the increase in velocity in the gap and thus reducing the pressure on the cylinder surface till the gap is small enough to introduce the effect of the boundary layer on the flat plate. This causes a reduction in velocity and an increase in the pressure whose minimum value occurs on the upper surface. The place of maximum velocity was found to shift from the upper part toward the centre of the gap with decreasing its size. The lift coefficient was found to increase with decreasing the gap while the drag coefficient was found to first increase till the gap size equals two diameters then decreases when it becomes smaller. When Reynolds number was increased to 40, all the curves have the same trends with the values of C_D and C_L smaller than that for Re = 20. The torque coefficient was found to be nearly constant for a large gap and negatively increasing when the gap is getting narrower till it reaches the value of –0.01 when the gap equals 1D. Concerning the flow pattern, when the cylinder was far from the wall, a couple of symmetric wakes were present behind the cylinder. This symmetry was disturbed by the wall effect when the cylinder gets nearer to the wall causing the wake pair to be skewed upward.

In the second case, when a clockwise rotation is added to the cylinder, the pressure increases on the lower surface and decrease on the upper one contributing effectively to an increase in the lift force. When the cylinder rotation is increased, no variation in the trend of the pressure distribution is observed although the stagnation point on the cylinder surface shifts to the lower surface of the cylinder. On the other hand, while increasing the cylinder rotation obviously increases the lift force, the change in the drag coefficient is small and increasing when the gap is smaller. Also it was found that the cylinder rotation causes a backward flow in the upper part of the gap when it becomes smaller. Concluding, we might say that the effect of cylinder rotation was to increase the lift force, induces a backward flow in the gap near the cylinder, shifts the front stagnation point to the lower surface and shifts the upper separation point upstream and the lower separation point downstream.

In the third case, they studied the flow around a fixed cylinder with a gap smaller than 1D. The cylinder is totally inside the boundary layer of the flat plate in this case, thus the velocity around the cylinder is decreased. Because of the boundary layer effect, which makes the velocity on the lower surface lower than that on the upper surface, the pressure on the lower surface is greater than the pressure on the upper surface. When the gap size decreases, the velocity inside the gap decreases quickly. For $H < 0.8$ D, the velocity is always smaller than the free stream velocity. When the gap is less than 0.7 D, the wake zone behind the cylinder disappears and is replaced by a recirculation zone on the plane wall. This recirculation zone moves toward the cylinder when the gap is decreased. The drag coefficient is decreased with decreasing the gap while the lift coefficient first increases and then decreases. The effect of the wall on the drag and lift coefficients, when the gap is less than one diameter, is about 10 times that when the gap is greater than one diameter.

In the fourth case, rotation was added to the cylinder with a gap less than 1 D. It was found that as the gap decreases, the pressure on both the upper and lower surfaces of the cylinder increases due to the decrease in the velocity associated with the presence of the flat plate. Because of the clockwise rotation of the cylinder, the velocity gradient on the upper surface of the cylinder is greater than the velocity gradient on the lower surface. For $H < 0.2$ D the pressure was found to reach an extreme on the lower surface due to the full reverse flow in the gap. The maximum velocity in the gap was found to shift toward the plate when H decreases due to the effect of cylinder rotation. The lift coefficient was found to increase and the drag coefficient was found to decrease nonlinearly with increasing the rotation. When Re is increased to 40, all the variables behave similar to the case when $Re = 20$. The torque coefficient C_M was found to shift from negative values to positive values when the rotation increased.

In all the previously mentioned work, the cylinders studied were either fixed or forced to rotate with a certain angular velocity, which was changed as a parameter governing the flow. Yet, the study of a cylinder that is left to rotate freely according to the torque applied on it by the fluid was not mentioned before. In such case, the problem is a bit more difficult as the motion of the cylinder and consequently the boundary conditions on its surface are constantly changing. The literature is very rich with studies about flow past fixed and rotating cylinders, but it is so poor when it comes to the data available about flow past cylinders that are free to rotate. Till this present work, only two papers were cited about viscous flows around freely rotating cylinders. The first one was that of Juarez et al. (2000), in which he made a simulation of freely rotating cylinders in viscous flows by high-order finite element method. The second one is the study made by Decourtye et al. (1998) where the idea of viscous microturbines was introduced.

In his work, Juarez et al. studied the unsteady flow past a free to rotate cylinder placed in a channel. He studied mainly the effect of changing the cylinder position inside the channel at a fixed Reynolds number and the effect of changing Reynolds number while the cylinder position is fixed. In such problem, the flow exerts a viscous torque on the cylinder surface. This causes the cylinder to rotate in the direction of the exerted torque. As a result, the cylinder, in turn, influences the flow field through changing the fluid velocity on its surface as long as the no-slip boundary condition is assumed. From this brief description of the flow nature, it is realized that both the rotation of the cylinder and the flow profile are coupled together and a certain technique in the solution algorithm should be developed to separate them from each other in the simulation. In his work, Juarez et al. set his code to first calculate the viscous torque on the cylinder surface, and then the cylinder rotational velocity was calculated using Newton second law of motion $T = I_0 \frac{d\omega}{dt}$ together with the knowledge of the rotational velocity at the previous time step. The velocity boundary conditions on the cylinder surface were updated according to the new angular velocity and then the Navier-Stokes solver was recalled again to calculate the flow field. This procedure was repeated till the end of the computational time. The initial condition assumed at the beginning of the calculations was that of the flow around a fixed cylinder at the same Reynolds number and cylinder eccentricity. This means that the cylinder was assumed to be held fixed while the fluid is flowing till it reaches steady state, then the cylinder is released. Yet, Juarez et al. did not study the case when the whole flow field is started from rest together with the cylinder, which means that at $t = 0$ no flow field exists and only a pressure difference is applied between the channel ends, a case that will be more frequently encountered if this configuration is used as a flow meter for small drug dosages. In this simulation the channel height was taken to be four diameters and the length was 27.5 diameters with 7.5 diameters upstream and 20 diameters downstream of the cylinder.

In the first part of the results section, Juarez et al. reported results for different eccentricities at a fixed Reynolds number. Eight different values for the eccentricity, $\in = 0,\ \frac{1}{6},\ \frac{1}{3},\ \frac{1}{2},\ \frac{2}{3},\ \frac{3}{4},\ \frac{5}{6}$ and $\frac{11}{12}$, were considered while Reynolds number was fixed at Re = 100. Depending on the value of the eccentricity, the flow changed between clockwise cylinder rotation, counterclockwise rotation or oscillatory motion. The oscillatory motion was associated with eccentricities of 0, 1/6, 1/3 where the flow experienced vortex shedding downstream of the cylinder. When $\in$ = 0, the cylinder oscillated forward and backward continuously with zero average angular velocity. The amount of maximum ω^* in each direction, where $\omega^* = \frac{\omega a}{U}$, was about 0.0124. Of course this value depends on the moment of inertia and consequently the mass of the cylinder. In this work, the cylinder was assumed to have the same density of the fluid, but any change in this value will result in a change in the angular velocity of the cylinder. When the cylinder was displaced from the center of the channel corresponding to $\in = 1/6$ & $1/3$, the shear stress differed on the upper and lower surfaces of the cylinder causing a net viscous torque on the cylinder which generated a net rotation in the clock wise direction. Yet, the cylinder still oscillated, or better saying "Ratcheted" as Juarez et al. described, due to the vortex shedding downstream of the cylinder. The period of oscillation was 5.3, 5.34, 5.45 for $\in = 0$, 1/6, 1/3 respectively. The Strouhal number for vortex shedding was 0.188, 0.187 and 0.184 for the three eccentricities, which is the same as in the case of fixed cylinders. It was clear that both the frequency and the amount of oscillation were decreasing with the increase in the eccentricity. When the lift coefficient was studied, it was found to oscillate as well with a zero mean value when $\in = 0$ and a positive mean value when $\in = 1/6$ & $1/3$. The value of the lift coefficient , which increases with the eccentricity, was higher than its value corresponding to the fixed cylinder under the same conditions. The drag coefficient was found to be oscillating as well and decreasing when the eccentricity is increased. This is a result of the fact that when the cylinder is shifted from the centre line, the velocity ahead of the cylinder decreases. Nearly the drag coefficient in the rotating cylinder case is the same as in the fixed cylinder case.

When the eccentricity was increased to ½ and higher, a steady solution in terms of the angular velocity was achieved. Juarez et al. reported that the precise value of $\in$ at which the steady solution is achieved was not calculated in his work. For $\in = 1/2$, 2/3, 3/4, the angular velocity is steady and negative (clockwise) while for $\in = 5/6$, 11/12, the angular velocity is steady but positive (counterclockwise), and its values compared to the negative ones are relatively high. The reason for clockwise rotation for small eccentricity values is due to the high shear on the upper cylinder surface associated with the high fluid velocity in the gap. When the gap gets smaller as $\in$ increases, the blockage effect of the wall reduces the velocity significantly and, consequently, the shear rate, thus the cylinder is rotating counterclockwise. Juarez et al. studied the stream lines and the vortex formation behind the cylinder and concluded that clockwise rotation is associated with the vortices formation downstream of the cylinder when it is held fixed before it is released while counterclockwise rotation is associated with the blocking effect of the wall when $\in$ becomes relatively large. The lift force was found to reverse its direction to become downward as the eccentricity is increased above $\in = 2/3$ due to Magnus effect when the eccentricity is increased to the limit that causes counter clockwise rotation of the cylinder. The drag coefficient was found to decrease constantly with increasing the eccentricity regardless to the direction of rotation of the cylinder. This is because of the decrease in the velocity ahead of the cylinder due to the increasing wall effect.

In the second part of his work, Juarez et al. studied the effect of changing Reynolds number while the eccentricity is held constant at $\in = 2/3$. Six different values of Reynolds number were tested, namely Re = 20, 40, 60, 100, 200 and 600. Different flow patterns were found according to the value of Reynolds number. Counter clockwise steady rotation was found at Re = 20, 40, while clockwise steady rotation was found at Re = 60, 100. When Reynolds number was increased to Re = 200, 400, oscillatory solution was found as the cylinder had an average clockwise rotation with periodic oscillations (i.e. Ratcheting). Depending on Reynolds number, the eccentric position of the cylinder creates two effects. The first one is the blocking effect associated with low

Re where the velocity of the fluid is decreased in the gap, thus causing a counter clockwise rotation of the cylinder by the main fluid stream in the channel. The second one is the nozzle effect associated with high Re where the velocity of the fluid is increased in the gap, thus causing clockwise rotation of the cylinder. The blockage effect occurred at Re = 20, 40 while the nozzle effect occurred at Re = 60, 100. By quadratic interpolation, the value of Reynolds number at which the cylinder changed its rotation direction was found to be Re = 58.15. When Reynolds number was further increased to Re = 200, 400, oscillations are introduced to the cylinder rotation without changing its direction. Negative lift coefficients were associated with the blocking effect due to the increased pressure on the cylinder upper surface and the reversed Magnus effect as well, while positive oscillatory lift coefficients were associated with very high Reynolds number due to the decreases pressure on the cylinder upper surface and the positive Magnus effect. For Re = 60, 100, the cylinder was rotating clockwise, thus creating an upward lift by Magnus effect, yet the increased pressure on the upper surface of the cylinder created downward lift. At Re = 60, the pressure downward lift is higher than the Magnus upward lift and the total lift coefficient is negative, while at Re = 100, the Magnus upward lift is higher (because of the increase in the angular velocity) than the downward pressure lift, thus the total lift coefficient is positive. Unlike the lift coefficient, the drag coefficient was found to decrease constantly with increasing Reynolds number.

Juarez et al. work, till now, is the most complete work available about flows around freely rotating cylinders. Yet, there are still some points that need to be clarified. The exact value of the eccentricity at which the cylinder rotation changes from oscillatory to steady rotation is still not precisely specified. Also, it is required to figure how this value will vary with changing Reynolds number. We do not know till now whether hystersis will exist in these values or not, which means we don't know if the value of the Reynolds number at which transformation from oscillatory to steady solution will be the same as its value at which transformation from steady to oscillatory solution occurs. In his work, Juarez et al. assumed in all cases that the cylinder is held fixed till the flow around it reaches steady state and then it is released. This is why his initial conditions are taken from the corresponding cases of a flow around a fixed cylinder. Yet, he did not study the case where the overall motion is started from rest, which means that at $t = 0$, only a pressure gradient is applied between the channel ends. Different heights of the channel (relative to the cylinder diameter) need to be considered to check if the flow will pertain the same patterns predicted by Juarez et al. or new patterns might appear. All these new parameters need to be considered in order to gain full understanding of this type of flow and in order to be able to engage it into anticipated applications.

2.3.2 Flow around spheres

Flow around spheres is one of the phenomena that are encountered in many of the engineering applications such as those concerning air pollution, particle transport processes and particle sedimentation, (Feng et al., 1994). As a result, studying flow around spheres gained a lot of the attention in matters of drag and lift forces exerted on the sphere, moment coefficient and stability of the flow behind the sphere. It is believed that knowing the parameters that affect the flow pattern around spheres as well as their effect and the phenomena associated with their change would strongly enhance our understanding of the flow around different immersed bodies which, in turn, will enhance our understanding of viscous micro pumps and turbines.

One of the important studies made in the field of flow around spheres is that of Kurose and Komori (1999), where they had studied, both numerically and experimentally, the effect of the sphere rotation and the fluid shear on the drag and lift forces on the sphere for a wide range of Reynolds number ($1 \leq Re \leq 500$). They solved three 3-D cases of flow around a stationary sphere in a linear shear flow, a uniform unsheared flow around a rotating sphere and a linear shear flow around a rotating sphere. Parallel with the numerical simulations, they conducted a visualization experiment on a falling iron particle in a linear shear flow of a glycerin solution to verify the numerical results for the direction of lift force on a stationary sphere in a linear shear flow. In the first part of the study, uniform unsheared flow around a stationary sphere was investigated to compare the results with existing literature. Two vortices formed downstream of the cylinder with the separation points moving upstream gradually as Reynolds number is increased. At high Reynolds number ($Re > 300$), vortex shedding takes place downstream of the sphere with Strouhal number of 0.128, 0.138 and 0.170 for $Re = 300$, 400 and 500 respectively. The drag coefficient was found to decrease constantly with increasing Reynolds number while the lift coefficient was found to be zero. At higher Re, some fluctuations appeared in the lift coefficient due to the vortex-shedding phenomenon but the time-averaged lift coefficient was still zero. These results for a stationary sphere were found to be in good agreement with already existing literature. The first case Ryoichi studied was that of a stationary sphere in a linear shear flow in order to examine the effect of fluid shear on the drag and lift coefficients. The non-dimensional shear rate ($\alpha^* = \frac{a}{U}\frac{\partial u}{\partial y}$) was varied from 0 to 0.4 along with the variation of Re = 0 - 500. The first effect of the fluid shear was to introduce asymmetry to the wake shape downstream of the sphere as well as to the place of the upper and lower separation points on the sphere surface. The drag coefficient was still found to decrease with increasing Reynolds number at constant α^* but it was found to increase with increasing the shear rate at constant Re and this effect was most clear at higher Reynolds numbers. The difference in the drag coefficient between the sheared and unsheared flows at Re = 500 & $\alpha^* = 0.4$ reached about 10%. The lift coefficient was found to decrease with increasing Reynolds number till it becomes negative at Re > 60. Although the amount of fluid shear does not affect the value of Reynolds number at which the lift coefficient becomes negative, but it sure affects the lift coefficient itself as it increases negatively with the increase in the fluid shear. These results were a bit contradictory with some of the already existing studies, which reported the lift force being always from the low velocity side to the high velocity side (i.e. $C_L > 0$) even though there is some studies that also reported negative lift force. The experimental results reported in this study agreed with the numerical simulation as 80% of the iron particles in the experiment was found to fall toward the low velocity side meaning that the lift force is from the high velocity side to the low velocity side. Vortex shedding still existed in the case of shear flow at Re > 300 with the Strouhal number increasing with both increasing Reynolds number and the fluid shear.

In the case of a uniform unsheared flow around a rotating sphere, the effect of rotation was found to shift the upper separation point downstream and the lower separation point upstream. The drag coefficient was still found to decrease with increasing Reynolds number but increasing with increasing the rotational velocity with a 10% increase in the drag coefficient in the case of $\Omega^* = 0.25$ relative to the case with no rotation both at Re = 500. The lift coefficient was found to be always positive on the contrary to the case of a stationary sphere in a shear flow. It is varying with Reynolds number and reaching nearly a constant value, which is increasing with the increase in the rotational speed, at Re > 200. Vortex shedding also starts at Re = 300 with the effect of rotational speed on Strouhal number similar to that of α^*, which means increasing the rotational speed increases the Strouhal number.

In the third case when the flow field around a rotating sphere in a linear shear flow was investigated, Ryoichi tried to see whether the drag and lift coefficients around a rotating sphere in a linear shear flow can be predicted from the addition of the drag and lift forces for a stationary sphere in a linear shear flow at the same shear rate and the drag and lift forces for a rotating sphere in a uniform unsheared flow at the same rotational speed. In other words, he tried to check if the effects of sphere rotation and fluid shear are independent of each other or not. A comparison, made between the drag and lift forces for a rotating sphere in a linear shear flow and the summation of the drag and lift forces in the two cases of stationary sphere in linear shear flow and a rotating sphere in a uniform unsheared flow, showed $C_L^{\alpha+\Omega} = C_L^{\alpha} + C_L^{\Omega}$ and $C_D^{\alpha+\Omega} = C_D^{\alpha} + C_D^{\Omega}$ for Re = 1 while this was not the case for Re = 200 ($C_L^{\alpha+\Omega}$ = lift coefficient for rotating sphere in a sheared flow, C_L^{α} = Lift coefficient for rotating sphere in an unsheared flow, C_L^{Ω} = Lift coefficient for a stationary sphere in a sheared flow). In the conclusion of his work, Ryoichi summarized his results in the following few points: both the linear fluid shear and the rotational speed increases the drag force with their effect more clear at high Reynolds numbers; the lift force in the case of a stationary sphere in a linear shear flow acts from the low velocity side toward the high velocity side and reverses its direction when $\mathrm{Re} > 60$ due to flow separation behind the sphere; the frequency of vortex-shedding, and consequently, Strouhal number increases constantly with both increasing the fluid shear and the sphere rotational speed.

Kalro and Tezduyar, (1998) studied unsteady flow around spheres numerically. The flow was axisymmetric and attached up to Re = 20 after which it separates and vortex shedding starts at around Re = 24. They reported that the vortex shedding in their study was very similar to the one reported by Magarvey and Maclatchy, (1961). The shedding frequency was reported to be in the range of 0.12-0.16.

2.3.3 Flow around square cylinders

In many of the applications when a certain performance, in terms of some pre-specified parameters, is required, irregular or non-uniform shapes sometimes prove to have better performance than uniform or streamlined bodies. In the case of viscous micro pumps and turbines, non-streamlined shapes might give better performance than the streamlined circular cylinders and spheres. As a consequence of such fact, a study of the nature of viscous flows around these non-streamlined bodies is essential in discovering some new parameters, which are only associated with these non-uniform shapes that might enhance the performance. Of these non-streamlined bodies that might be used as a rotor in the proposed viscous micro pump and turbine, square cylinders appear to be worth studying for such application. Square cylinders have sufficient geometrical differences from the circular cylinder that are enough to trigger the appearance of new flow patterns and consequently new governing parameters, and in the same time, they will not require a major change in the problem geometry as it will be if we use a hollow or a porous rotor for example.

Flow around square cylinders is a common problem that attracted a considerable amount of research. Of course the existing literature is not as rich as that available for flow around circular cylinders, but it is quite enough to get an idea of the flow pattern and the existing differences from the flow around a circular cylinder. Of these studies, Sohankar et al. (1999) made a simulation for two and three-dimensional flow around square cylinders using the finite volume method. In a brief comparison of the flow around a circular or a square cylinder, Ahmad stressed the effect of the existence of sharp corners in the case of square cylinders, which increase the tendency of flow instabilities at high Reynolds numbers. Although, the stages of flow patterns development in both the case of a circular or a square cylinder is the same, the value of Reynolds number at which transition from one stage to another is different. The flow is characterized by no separation at the beginning, for Re less than unity, then a couple of vortices appear at the back of the square cylinder. This vortex pair starts to grow with increasing Re till a critical stage is reached and the vortex pair transfers into a Von Karman Vortex street. The critical value of Re at which this transformation occurs is Re~50. The value of Re_{cr} changed depending on the solid blockage amount β, where $\beta = \frac{D}{H}$, D = length of square side, H = channel height. When Re was increased more, a transition from 2-D flow to $3-D$ flow occurs at around Re = 170 - 190. In his work, Sohankar studied the 2-D and 3-D cases for values of Reynolds number ranging from $Re = 150$ to $Re = 500$. Till Re = 150, the flow pattern was two-dimensional with laminar vortex shedding. When number was increased till $Re = 200$, three-dimensional effects appeared. The lift and drag coefficients were found to oscillate with time and to change along the cylinder in the span wise direction. The amplitude of oscillations in the two-dimensional case was higher than in the three dimensional case.

Since the cause of the main differences in the flow between square and circular cylinders is the existence of the sharp corners in the square one, it was of much importance to study the effect of the corners shape on the flow around the cylinder. Tamura et al. (1998) studied, numerically, the flow around a square cylinder with different corner shapes. Tamura compared the flow patterns around three square cylinder with sharp corners, chamfered corners and rounded corners for $Re = 104$. The chamfer was at 45° and 1/6 B, where B is the side length, and the fillet radius, in the case or the round corners, was the same size. A parallel experimental study was performed to compare numerical and experimental results. In the experiment, the pressure was measured at one section around the circumference of the cylinder and along the cylinder span as well. Primarily, the effect of the chamfer or round corners was to narrow the wake region, which resulted in a more complicated pressure distribution pattern compared to the case of sharp corners. Compared to experimental results, computations gave higher values for the drag and lift coefficients. This, as explained by Tamura, might be due to the existence of small velocity fluctuations in the upcoming stream in the experiment, which was not present in the computational model. Also the existence of 3-D effects due to the passage walls boundary layer, sure, would cause a difference from a 2D simulation. The lift coefficient was found to oscillate, so its rms value was calculated. The drag coefficient and rms lift coefficient were found to decrease in the case of chamfered corners and to decrease more in the case of round corners. Despite the geometric difference, which affected drag, lift and pressure, the Strouhal number was found to be constant between 0.1 and 0.15 in the three cases. Regarding the pressure distribution, the chamfered and round corners were found to cause drastic decrease in the pressure compared to the sharp corner case. Negative pressure was even achieved on the frontal region indicating the significant effect of corner shape in such flow. Tamura's work gave an idea of the change the corner shape might introduce in the flow field around the square cylinder, yet a more detailed study is encouraged to test the corner effect under different Reynolds numbers, the onset of vortex shedding and how it is affected by the corner shape and the mechanism of vortices formation downstream of the cylinder. Other different corner shapes and the effect or the relative size of the corner dimension to the square cylinder size might be very helpful to gain better understanding of the flow field around square cylinders.

2.4 Objectives

In all the previous sections we mentioned the root of the idea of viscous micropumps and microturbines together with the studies that cover most of the flow details that should be a part of any future work in this field. It is noted that there are no studies at all for the transient performance of viscous micropumps during start up. This is expected to be an important issue especially if it is used for drug dosing applications which have been named by its inventors as the most appropriate application for it. In the current study, transient performance of viscous micropumps will be investigated numerically. The effect of the main parameters which govern pump start-up and steady state performance will be investigated. These parameters are either geometrical parameters like the micropump channel height and the cylinder eccentricity or flow parameters like Reynolds number and pump load. The study will include the effect of each parameter on the time the pump takes to reach steady state, the average fluid velocity inside the pump, the flow pattern inside the micropump and the lift, drag and moment coefficient of the rotor. Pressure and shear stress distribution on the cylinder surface are also monitored for many cases to see how they are related to flow patterns inside the micropump. The pumping efficiency and its dependence on each of the main parameters will be reported in order to have an idea about the feasibility of the viscous micropump.

It is expected that using more than one rotor inside the micropump will enhance its performance considerably. Thus, the effect of using more than one rotor and the different orientations of these rotors inside the micropump are intended to be studied as well. Sample cases of different multi-rotor orientations will be studied in order to have an idea about how far the use of more than one rotor will enhance the performance. The pressure and shear stress distribution on the different rotors will be reported as well.

Chapter III

Mathematical modeling and numerical solution

3.1 Pump geometry and flow parameters

The micropump is composed of a cylinder with diameter *d*, placed inside a channel with height *h*, with its axis perpendicular to the channel axis. Figure 1.1 shows a schematic of the pump geometry. The main geometrical parameters in the study will be the channel height (*S*) defined as

$$S = \frac{h}{d} \tag{1}$$

and the cylinder eccentricity $\in$, which indicates the cylinder position inside the channel. The eccentricity is defined as:

$$\in = \frac{y_c}{\frac{h}{2} - \frac{d}{2}}. \tag{2}$$

Based on this definition, $\in = 0$ corresponds to the cylinder being centered on the channel axis and $\in = 1$ corresponds to the cylinder touching the lower wall.

The cylinder is forced to rotate with an angular velocity ω. The unequal viscous forces on the upper and lower surfaces of the cylinder, due to the unequal upper and lower gap sizes, causes a net fluid flow in the channel. In this problem, Reynolds number

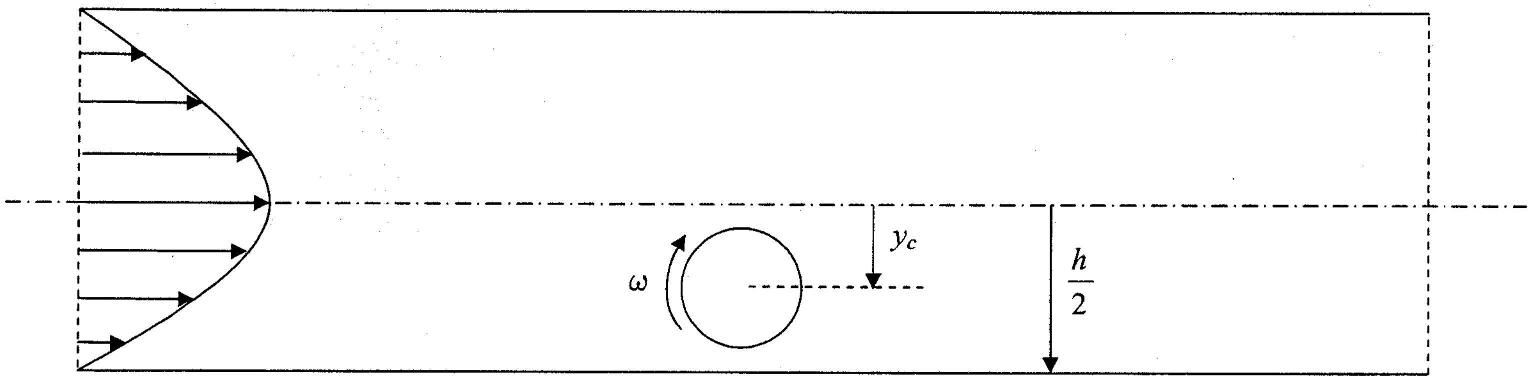

Figure 3.1: Schematic of the micropump geometry.

will be based on the cylinder surface velocity $U = \dfrac{\omega\, d}{2}$ since the average velocity in the channel $\bar{u} = \dfrac{1}{h}\int_0^h u\, dy$ is an output of the solution. Therefore, Reynolds number will be defined as:

$$\mathrm{Re} = \frac{U\, d}{\nu} = \frac{\omega\, d^2}{2\,\nu}. \tag{3}$$

The pressure is specified on the inlet and outlet of the channel. A higher pressure is specified at the outlet to simulate the pressure head the pump should supply. This head is needed to overcome the pressure drop in whatever circuit the pump is attached to. The non-dimensional pressure rise is defined as:

$$\Delta P^* = \frac{P_{out} - P_{in}}{\dfrac{\rho\,\nu^2}{d^2}}, \tag{4}$$

where P_{out} is the pressure on the pump outlet and P_{in} is the pressure on the pump inlet, ρ is the fluid density, and ν is the fluid kinematic viscosity.

The scale used to non-dimensionalize the time in the simulation was chosen to be the time taken by the rotor to finish one complete revolution:

$$t^* = \frac{t}{\dfrac{2\pi}{\omega}} = \frac{t\,\omega}{2\pi}. \tag{5}$$

According to this definition, the non-dimensional time is simply the number of revolutions of the rotor. This provides an easier tracking of the changes in the flow field over time regardless of the rotor angular velocity.

The drag, lift, and moment coefficients are defined as

$$C_D = \frac{F_D}{\frac{1}{2}\rho V^2 D}, \tag{6}$$

$$C_L = \frac{F_L}{\frac{1}{2}\rho V^2 D}, \tag{7}$$

and

$$C_M = \frac{M}{\frac{1}{2}\rho V^2 D^2}, \tag{8}$$

3.2 Governing equations and boundary conditions

The 2-D Navier-Stokes equations will be solved for the specified geometry where all the dimensions will be normalized by the cylinder diameter *d*. The flow will be assumed to be laminar, incompressible and Newtonian with constant properties. Based on these assumptions, the continuity equation will have the form:

$$\nabla \cdot \vec{V} = 0, \tag{9}$$

and the momentum equation:

$$\rho\left[\frac{\partial \vec{V}}{\partial t} + (\vec{V}\cdot\vec{\nabla})\,\vec{V}\right] = \rho\vec{\alpha} - \vec{\nabla}P + \mu\,\nabla^2\vec{V}, \tag{10}$$

where α represents the body forces per unit mass. Based on the above mentioned method for non-dimensionalizing, and assuming that the flow is incompressible with neglected body forces, the momentum equation becomes

$$\frac{\rho\,\omega^2 d}{4}\left[\frac{1}{\pi}\frac{\partial\overrightarrow{V^*}}{\partial t^*}+(\overrightarrow{V^*}\cdot\vec{\nabla})\,\overrightarrow{V^*}\right]=\frac{\mu\,\omega}{2\,d}\,\overrightarrow{V^*}-\frac{\mu^2}{\rho\,d^3}\,\vec{\nabla}P^*, \tag{11}$$

which in non-dimensional terms becomes

$$\frac{1}{\pi}\frac{\partial\overrightarrow{V^*}}{\partial t^*}+(\overrightarrow{V^*}\cdot\nabla)\overrightarrow{V^*}=\frac{1}{\mathrm{Re}}\nabla^2\overrightarrow{V^*}-\frac{1}{\mathrm{Re}^2}\nabla P^*. \tag{12}$$

No-slip, no-penetration boundary conditions are assumed in the viscous micropump. This means that the fluid velocity is zero on the upper and lower walls and is equal to the cylinder surface velocity on the cylinder boundary. The pressure is specified on the inlet and outlet of the micropump. Pressure will be always assumed to be zero gage pressure at the inlet and its value at the exit will be varied to simulate different loads. Different fluids will be used in order to test the pump under different fluid viscosities to observe how this parameter affects the pump performance. The fluid will be assumed to be initially at rest ($\vec{V}=0$) and the motion will start by rotating the cylinder clockwise with an angular velocity ω. The main independent parameters in the solution will be the channel height S, the cylinder eccentricity $\in$, Reynolds number Re, and the pump load P^*.

3.3 Numerical solution

The CFD package FLUENT 6.0 is used to solve the Navier-Stokes equations numerically. This CFD package uses the finite volume method and supports unstructured grids. It enables the use of different descretization schemes and solution algorithms, together with various types of boundary conditions. As part of the same package, a preprocessor, Gambit, is used to generate the required grid for the solver. An unstructured grid with triangular elements is used. The cylinder surface was divided into

100 equally spaced elements. The upper and lower walls were divided into 200 non-uniformly spaced elements using the Bell Shaped meshing scheme with a ratio $R = 0.4$. The grid was finer in regions near the center and adjacent to the cylinder, and was coarser in regions far upstream and downstream. The Bell shaped scheme meshes the edge so that the node distribution follows a normal distribution curve centered at the geometric center of the edge. The ratio R specifies whether the nodes will be denser at the center of the edge or at its ends, and also specifies the intensity of this distribution. In addition to this meshing method, which refines the grid in the cylinder region, grid adaptation by the solver itself was performed in the gap between the cylinder and the lower wall for cases of high eccentricities, where this gap is very small.

The Piso-Simple algorithm, where PISO stands for Pressure-Implicit with Splitting of Operators, was used for the pressure-velocity coupling. It is nearly the same as the SIMPLE algorithm, presented in Patankar (1980), except that it takes into account two additional corrections. The first one is the neighbor correction. This correction incorporates more iterations into the pressure correction equation in order to satisfy the continuity and momentum equations more precisely. Thus, the PISO algorithm requires more time per iteration, but at the same time decreases the total number of iterations. Therefore, the total time is much less, rendering it more suitable for transient applications. The second correction is the skewness correction, which simply enables the solver to deal with highly skewed meshes and reduce the total number of iterations required for the convergence on such meshes.

Two different descretization schemes were used for the time and momentum equations. A power law scheme was used for the two momentum equations while a second order descretization scheme was used for the time derivatives. Under-relaxation was used during the solution with the under relaxation factors varying between 0.3 and 1 to ensure convergence. Multi-grid methods were also used in order to reduce convergence time. The use of multi-grids helps reduce the low frequency error components when the equations are iterated on a coarser mesh. By default, a V-cycle multi-grid is chosen for the pressure correction equation while a flexible cycle was chosen for momentum equations. In the V-cycle, one iteration is first performed on the finest grid to reduce the high frequency components of the error, and then the solution is restricted to the coarser grid. After a certain number of iterations on the coarser grid, the solution is interpolated to the finer grid where it is iterated again. For the flexible cycle, the use of coarse grid corrections is called only in the cases where the convergence rate on the current grid is slow. (FLUENT 6.0 user guide manual)

3.3.1 Grid independence

Different meshes were used at the beginning to determine the optimum grid size and to ensure grid independent solutions. Five meshes have been tested for the case of $S = 2.5$ and $\in = 0.95$ as well as S = 1.5 and $\in = 0.6$. The grid size was identified through the number of nodes on the cylinder surface and on the upper and lower sides of the pump channel. In the first mesh, the cylinder was divided into 10 elements and the upper and lower sides were divided into 50 elements. Due to the nature of the unstructured grid used, the number of elements on the inlet and outlet surfaces does not affect the degree of refinement of the grid in the whole domain. For each grid the solver adapted the region between the cylinder and the lower wall. The different meshes used are shown in Figure 1.2. The sizes of all five meshes are shown in Table 1.1.

Grid independent solution was assured by observing three parameters. The first parameter is the distribution of the x-velocity component on a vertical plane just one diameter from the cylinder axis, and will indicate whether the grid is fine enough in the neighborhood of the cylinder where the largest shear stresses exist. Figure 3.3 and 3.4 shows the velocity distribution on a plane one diameter downstream of the cylinder center for the cases $S = 1.5$ $\in = 0.6$ and $S = 2$ $\in = 0.95$ at different mesh sizes.

The second parameter is the change of the drag coefficient of the cylinder with time, Figure 3.5 and Figure 3.6, which tests the coupling between the grid size and the time step chosen. The convergence of the drag coefficient over the grid size was achieved on the third mesh used. The trend of the drag coefficient variation with time on all the meshes

Table 3.1: Properties of different grids used

Mesh	Number of cylinder elements x Number of wall elements	Number of control volumes	
		S = 1.5	S = 2.5
Mesh1	10x50	589	985
Mesh2	20x100	2241	3652
Mesh3	40x150	5151	8611
Mesh4	80x150	6341	11533
The used Mesh	100x200	11044	18983

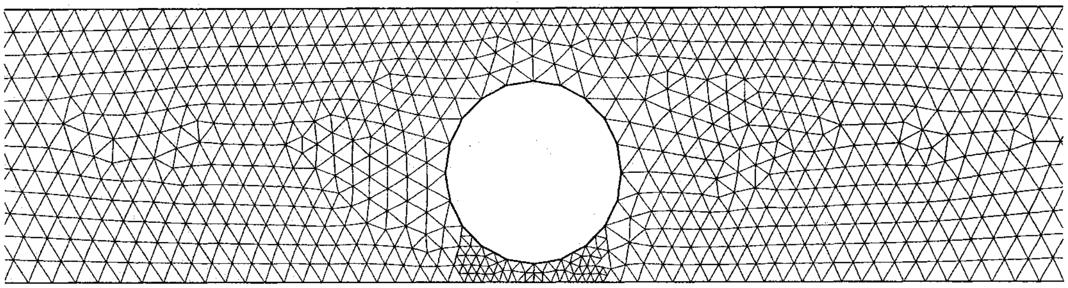

a) 20x100

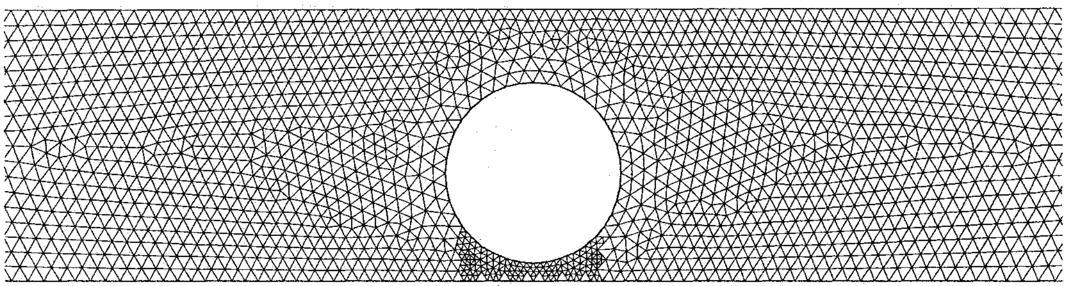

b) 40x150

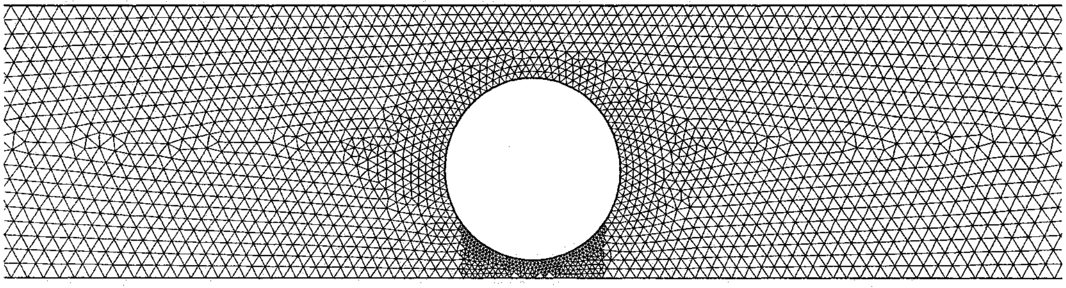

c) 80x150

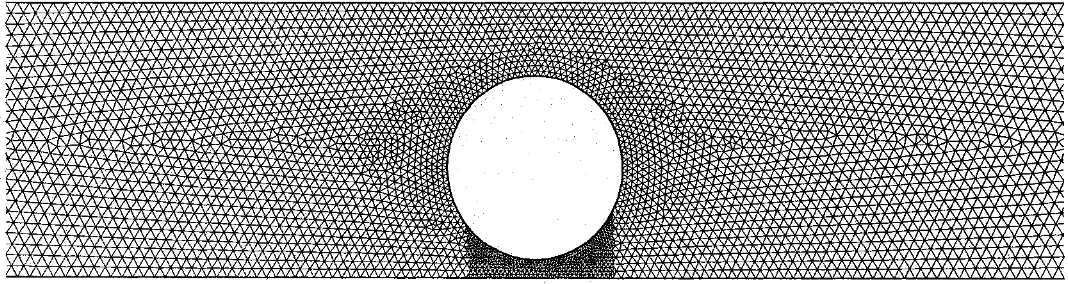

d) 100x200

Figure 3.2: Different meshes used for the grid dependence test.

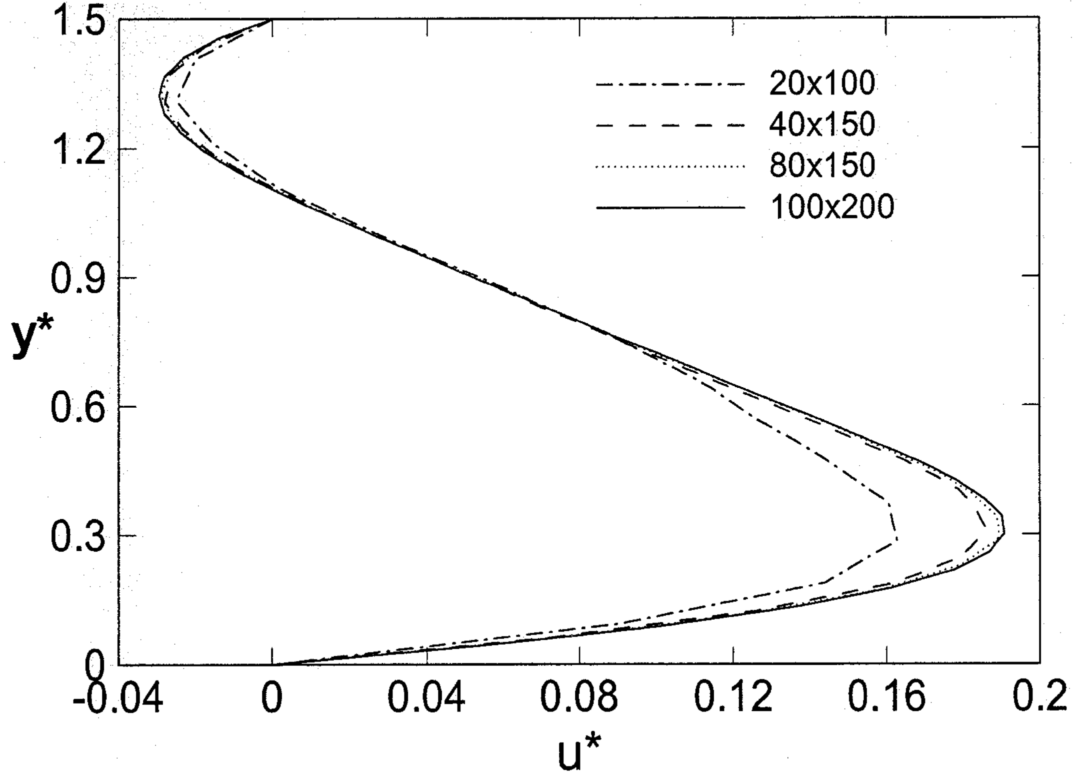

Figure 3.3: X-Velocity on plane $x^* = 9$ on different meshes
($S = 1.5$, $\in = 0.6$, $\Delta P^* = 0$, $Re = 1$).

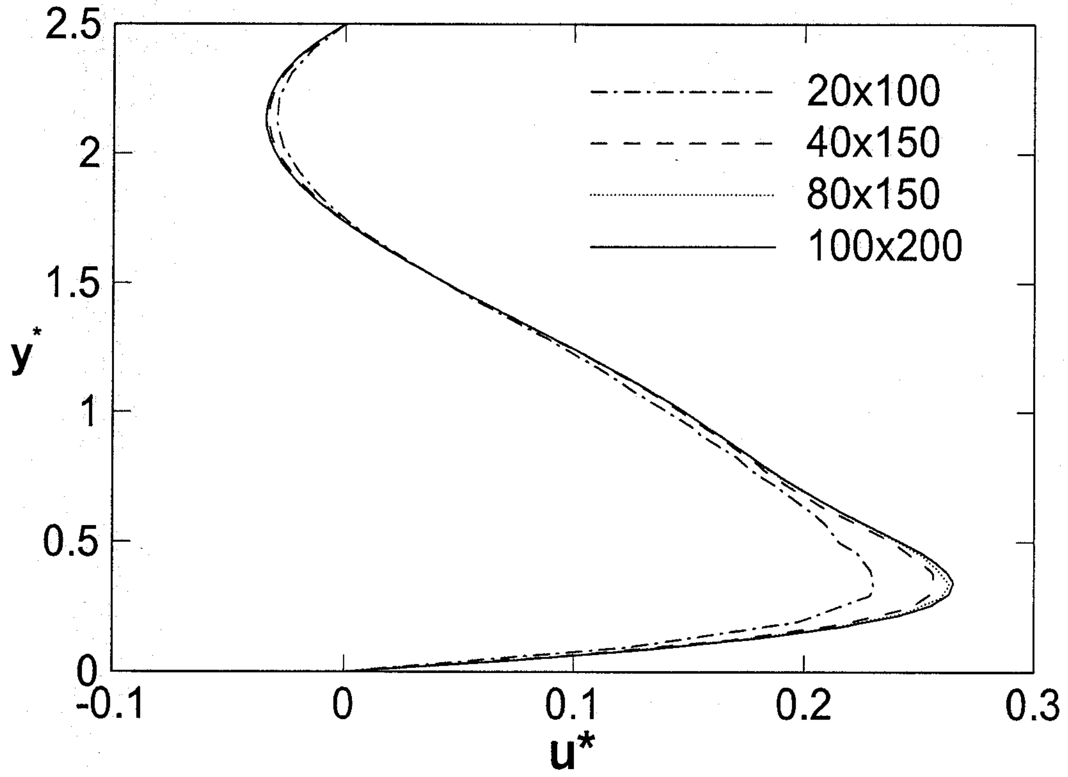

Figure 3.4: X-Velocity on plane x* = 9 for on different meshes

($S = 2.5$, $\in = 0.95$, $\Delta P^* = 0$, $Re = 1$).

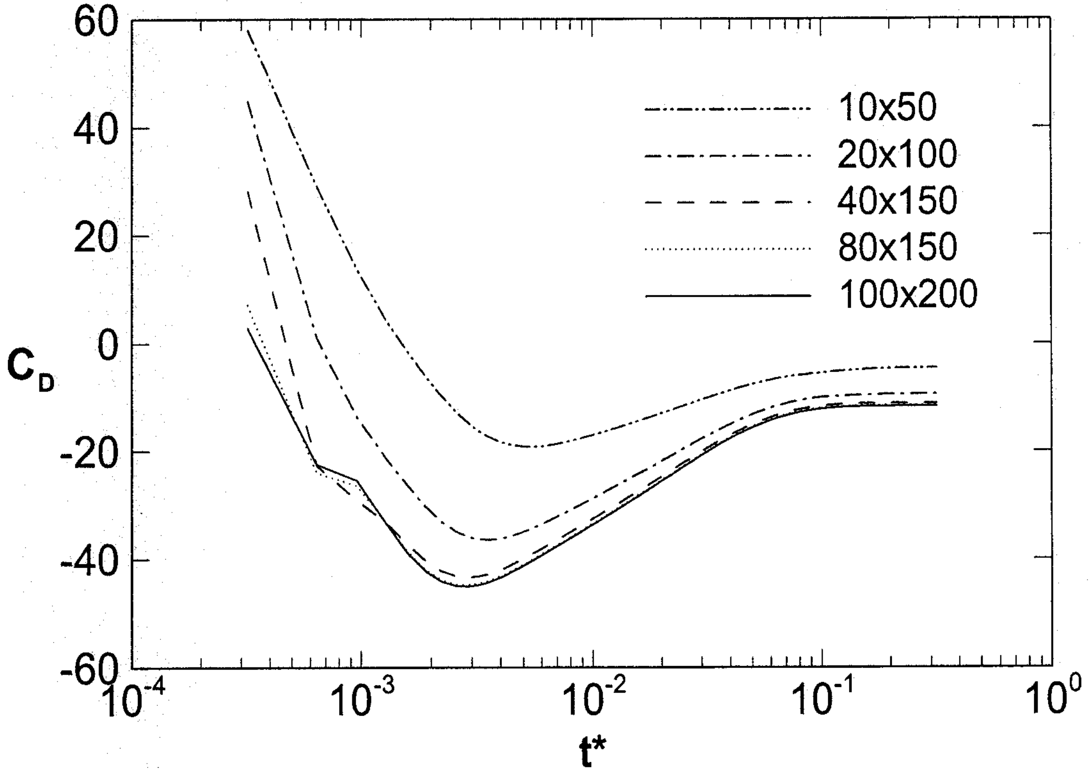

Figure 3.5: Change of the drag coefficient with time on different meshes ($S = 1.5$ $\epsilon = 0.6$ $\Delta P^* = 0$ $Re = 1$).

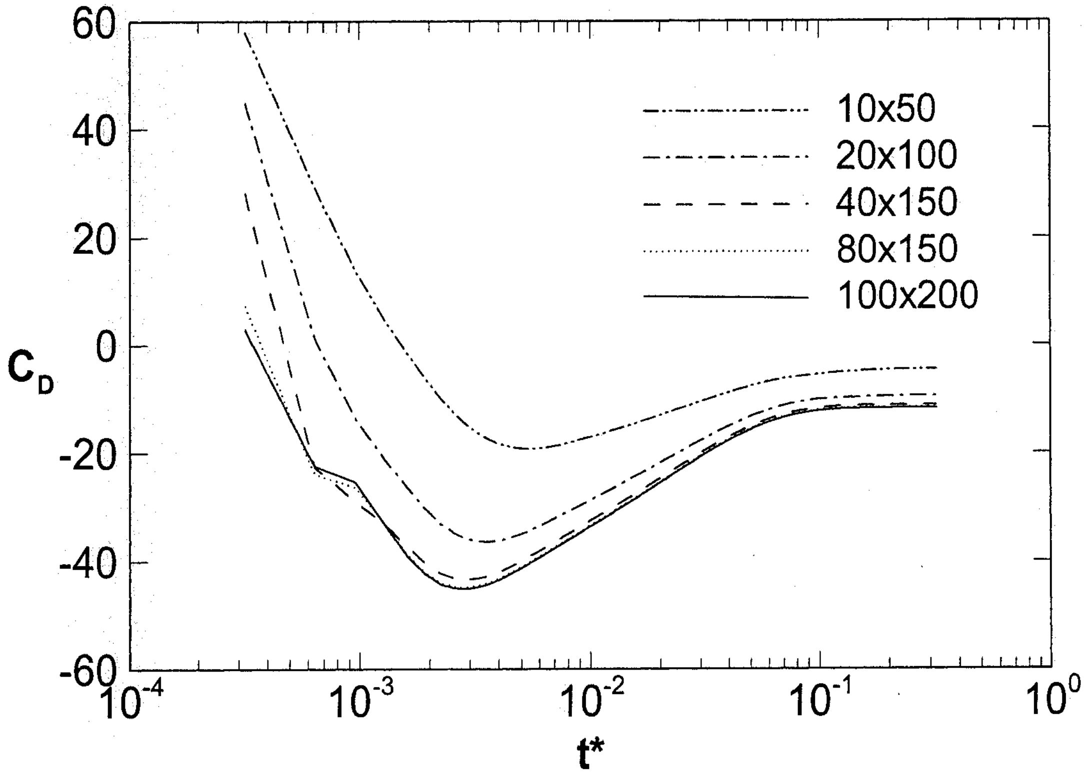

Figure 3.6: Variation of the drag coefficient with time on different meshes ($S = 2.5$ $\epsilon = 0.95$ $\Delta P^* = 0$ $Re = 1$).

used was the same, where differences only occurred between the coefficients values themselves. The first few points in all the curves of the drag coefficient change with time experienced sharp changes which is thought to be due to numerical calculations because the cylinder at time t = 0 is assumed to accelerate from zero velocity to its pre-set angular velocity in zero time. It has to be mentioned as well that it is the logarithmic scale nature that enlarges effect of the first few time steps to look as shown in the figures. The truth is they are only three points out of more than one thousand points.

The third parameter is the average velocity of the flow on the outlet from the pump, which will give a good indication of the effect of the grid size in the entire micropump domain. Table 3.2 compares the values of the average dimensionless velocity inside the channel for the different grid sizes.

3.3.2 Convergence

The scaled residuals of the corresponding conservation equation were the criterion that assessed the convergence for each time step (Patankar, 1980; FLUENT 6.0 user guide manual). After the descretization of any conservation equation with any variable Φ, the equation will appear in the form

$$a_P \Phi_P = \sum_{nb} a_{nb} \Phi_{nb} + b, \tag{13}$$

where a_P is the coefficient for the active cell for this equation, a_{nb} is the corresponding coefficients for the neighboring cells, and b is the contribution from the constant part of the source terms. The residuals of such equation are calculated according to equation 14:

Table 3.2: The variation of the fluid average velocity with grid size

Grid	U* ($S = 1.5$, $\in = 0.6$)	U* ($S = 2.5$, $\in = 0.95$)
10x50	0.0527	0.0632
20x100	0.0703	0.0859
40x150	0.0757	0.0919
80x150	0.077	0.0932
100x200	0.0769	0.0943

$$R = \sum_{all-cells} \left| \sum_{nb} a_{nb}\Phi_{nb} + b - a_P\Phi_P \right| \tag{14}$$

In order to assess convergence more accurately, the solver monitors the residuals scaled with respect to the summation of the variable Φ over the whole domain. Accordingly, the scaled residuals are calculated according to the following equation:

$$R_{scaled} = \frac{\sum_{all-cells} \left| \sum_{nb} a_{nb}\Phi_{nb} + b - a_P\Phi_P \right|}{\sum_{all-cells} \left| a_P\Phi_P \right|}. \tag{15}$$

As a convergence criterion in the present work, the solver iterated the equations until the scaled residuals are less than 10^{-5} or until it stabilized at a constant value, which is still small enough to ensure convergence. This value varied approximately from 10^{-5} to 3×10^{-4}, based on the parameters for each specific case. Figure 3.7 shows the effect of the residuals on the solution accuracy.

3.3.3 Time step size

The time step used for simulating the transient operation of the micropump needed to be small enough to pick the physical changes over time inside the flow field, as well as to ensure stability. Different time steps were tested at the beginning in order to determine the optimum time step to be used. Obviously, the optimum time step size varies from one case to another, since the Reynolds number (i.e. the cylinder angular velocity) is different in the various cases. The optimum time step should be the one that, when coupled with the cylinder angular velocity, corresponds to small changes in the cylinder angular

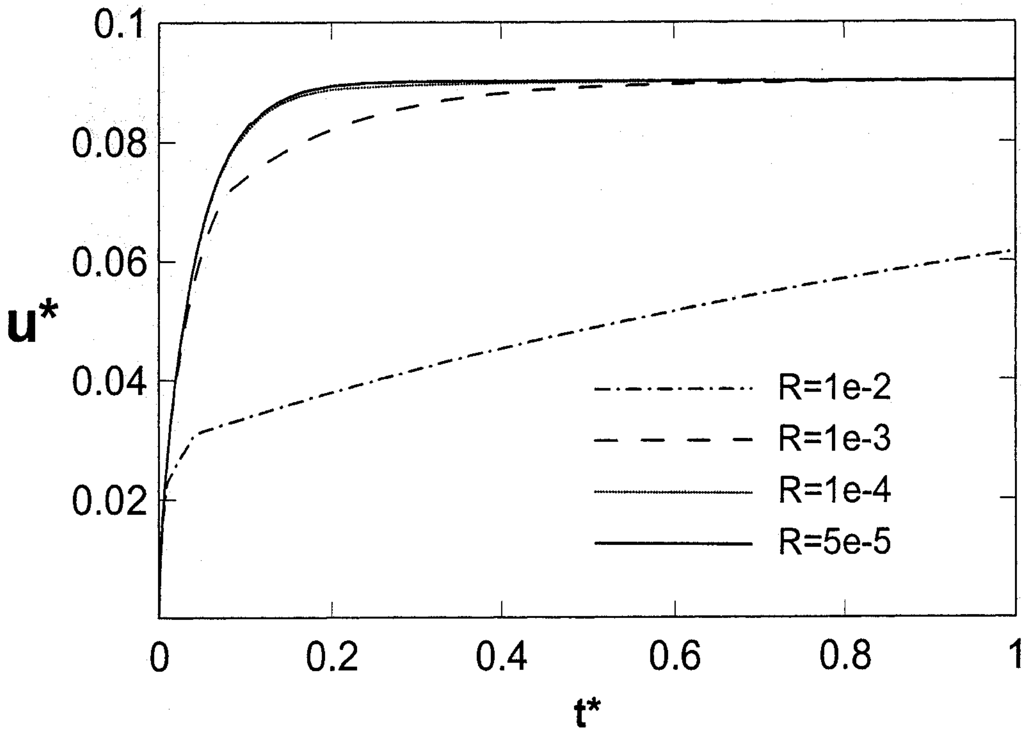

Figure 3.7: Effect of residuals on the change of u* with time ($S = 2$ $\epsilon = 0.95$ $\Delta P^* = 0.5$ $Re = 1$).

displacement so that any corresponding changes in the flow field may be monitored. The change of the average velocity inside the micropump channel with time was used as a criterion to determine the optimum step size. Time step sizes of Δ t = 0.0001, 0.001, 0.01 and 0.1 sec (corresponding to Δt^{*}= 3.198e-5, 3.198e-4, 3.198e-3 and 3.198e-2 at Re = 1) were tested. The results for Δ t = 0.0001 , 0.001 and 0.01 sec were nearly the same while for Δ t = 0.1sec large fluctuations in the average velocity occurred indicated instability. The time step chosen for nearly all the cases studied was 0.001 s which was small enough to monitor all the changes in the flow field over time, and, in addition, was large enough to achieve reasonable computation time. Figure 3.8 shows the effect of time step size on the calculation of the change of the average velocity inside the micropump with time.

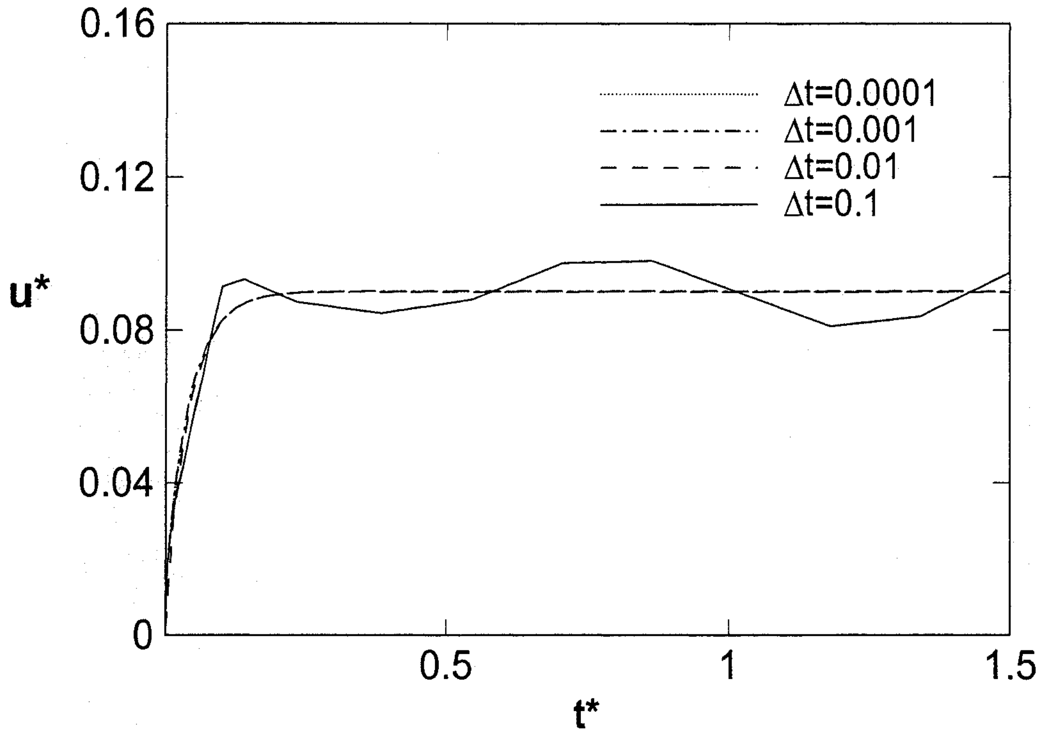

Figure 3.8: Effect of time step size on the change of u* with time

($S = 2$ $\in = 0.95$ $\Delta P^* = 0$ $Re = 1$).

Chapter IV

Single-rotor viscous micropump

4.1 Comparison with previous results

Before the transient operation of the micropump was studied, some steady state cases were simulated and the results were compared with existing numerical and experimental results. Existing experimental results for steady state cases were obtained from Sen et al. (1996), while numerical results were obtained from Sharatchandra et al. (1997). The effect of the micropump channel height on the pump flow rate was studied both experimentally and numerically in the two studies mentioned above. In the present study, and for comparison purposes, eleven cases were simulated with different channel heights of S = 1.1, 1.2, 1.3, 1.4, 1.5, 1.6, 1.8, 2.0, 2.5, 3.0, and 3.5 with an eccentricity $\in = 0.9$. It should be noted that the eccentricity, $\in = 0.9$, corresponds to the value of the maximum eccentricity, $\in_{max,}$ in the two references mentioned above. In all cases studied, the Reynolds number was kept constant at Re = 0.5, and the pump load was $\Delta P^* = 0.5$. Figure 4.1 shows the comparison between the results attained in the present study and the previous ones. It is clear that the results are in very good agreement with both the computational and experimental results. The largest difference occurred at the largest channel height (S = 3.5). This difference may be due to the fact that the gravity forces were neglected in the simulation; these forces will have an increasing effect as the channel height is increased.

The rotor eccentricity in the viscous micro pump is the main parameter that initiates the driving force of the pump. Sharatchandra studied the effect of the rotor eccentricity

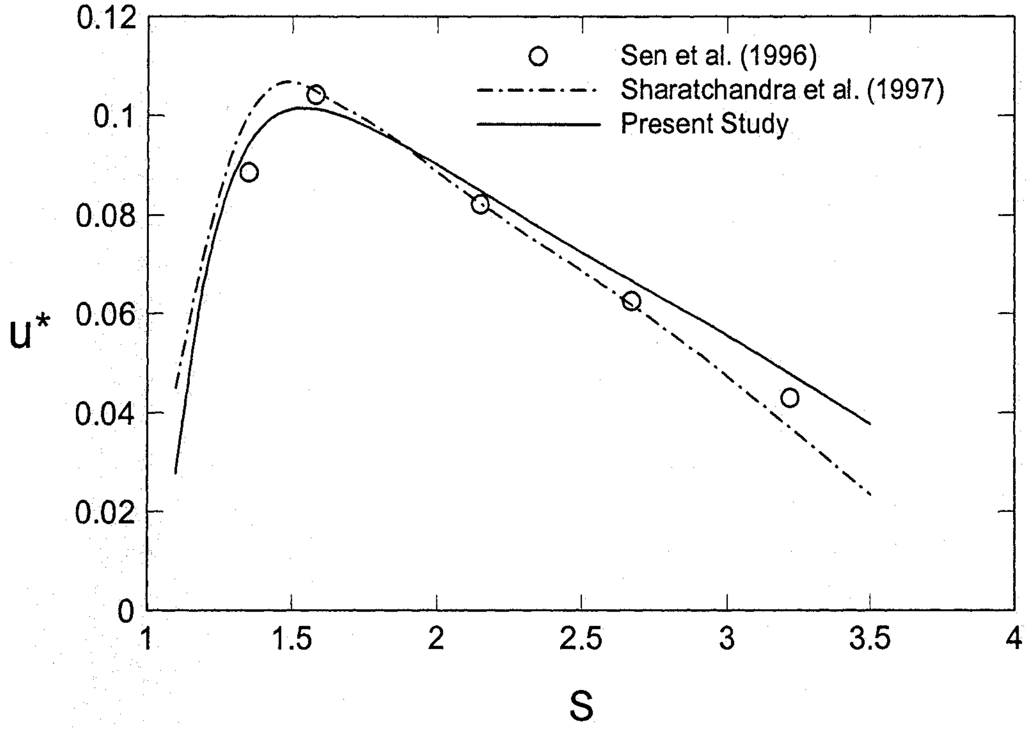

Figure 4.1: Comparison of average velocity vs. channel height (Re = 0.5, $\Delta P^* = 0.5$ and $\in = 0.9$).

on the fluid average velocity in the channel and found that the average velocity increases nearly linearly with the eccentricity. Figure 4.2 compares the results calculated by Sharatchandra et al. and those calculated in the present study for the cases S = 1.5 & 2.5 where the pressure and Reynolds number were kept constant at $\Delta P^* = 1$ & Re = 1. Both show the nearly linear variation of the average velocity with the rotor eccentricity.

In addition, Sharatchandra et al. observed a linear relation between the pump flow rate and the imposed pressure rise (pump load) exerted on the pump. This observation was confirmed in the present simulation for different geometries and flow configurations. Figure 4.3 shows the non-dimensional (Q - P) curve for the cases S = 2.5, $\in = 0.9$, and Re = 1, as well as the case of S = 1.5, $\in = 0.9$, and $\mathrm{Re} = 1$ for the present and previous studies.

4.2 Effect of micropump channel height

The present study on viscous micropumps showed different transient flow patterns when the channel height was changed between $S = 1.5$ to $S = 3.5$. These differences in the flow pattern affected all the flow parameters, from the time needed to reach steady state operation to the variation of drag and lift coefficient with time. Figure 4.4 shows the effect of the channel height S on the start-up performance of the micro pump. It is clear that when the channel height is increased, the pump requires a longer time to reach the steady state flow rate. This is due to the reduction of the shear stress on the upper cylinder surface resulting from the larger distance between the cylinder and the upper wall; this reduces the flow driving force. Moreover, in the cases of higher S, the momentum of the fluid layers adjacent to the cylinder is diffused through a larger number

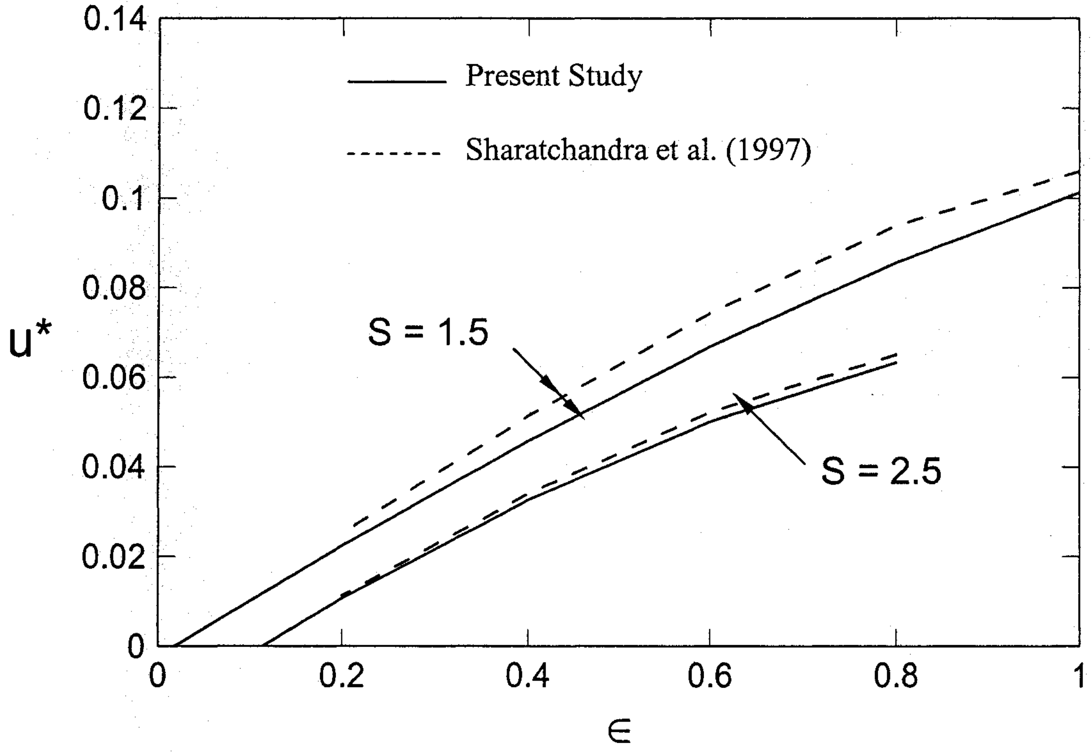

Figure 4.2: Comparison of average velocity vs. eccentricity at $\Delta P^* = 1$ and $Re = 1$.

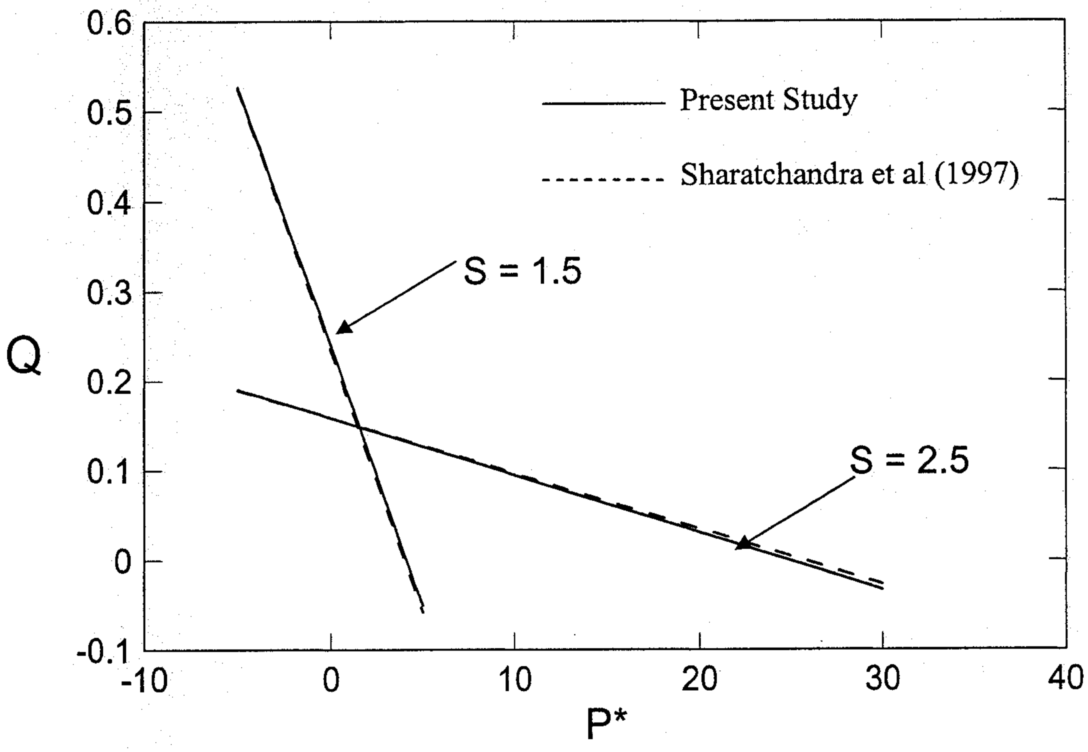

Figure 4.3: Flow rate vs. pump load at Re = 0.5 and $\in$ = 0.9.

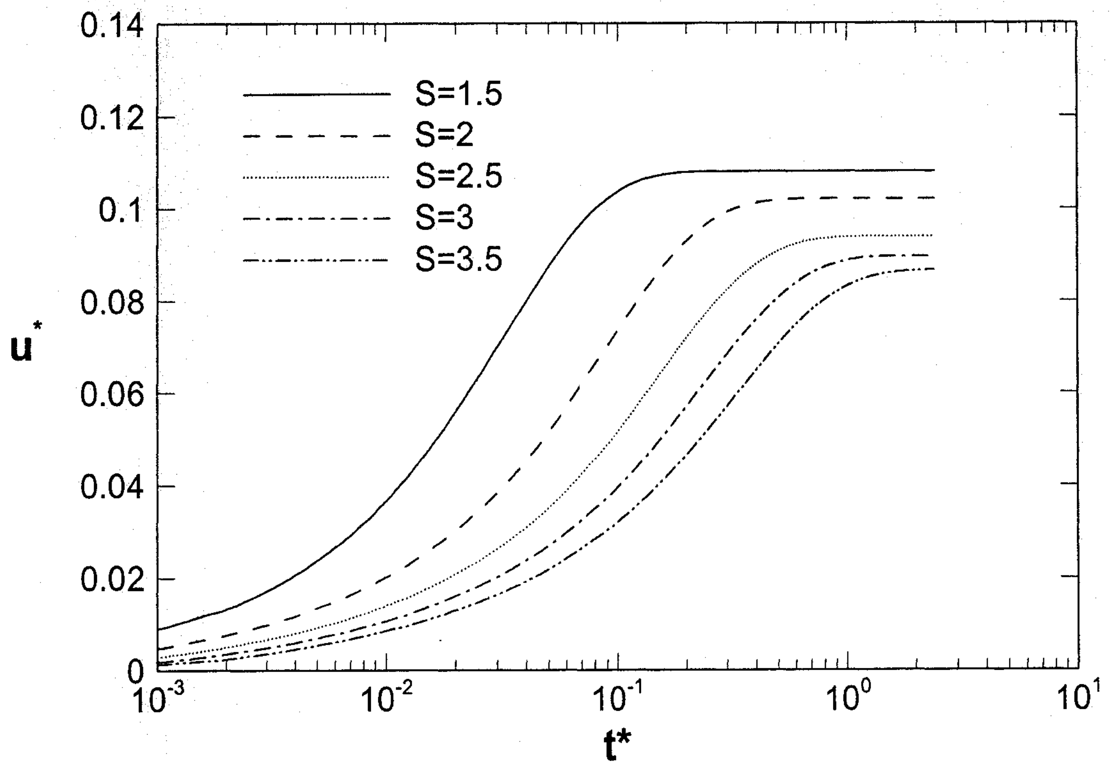

Figure 4.4:. Start-up operation for different channel heights ($\in = 0.95$, $\Delta P^* = 0$ and $Re = 1$).

of fluid layers in order to reach the region adjacent to the upper wall, which takes a longer time depending on the viscosity of the working fluid. The micropump time constant was defined as the time taken by the pump from the instant it starts until the instant the average velocity inside the pump channel reaches 99% of its steady state value at the same conditions. This time constant was found to increase with increasing the channel height, Figure 4.5.

It was observed that the drag, lift, and moment coefficients depend on the channel height. However, before these coefficients could be studied, the nature of the flow field and the pressure distribution around the cylinder in the micropump had to be examined. For small channel heights, two small counterclockwise co-rotating vortices form at the upper-left and upper-right sides of the cylinder, Figure 4.6-a. This pair of vortices moves upward when the channel height is increased Figures 4.6-b&c, until the two vortices merge together to form one large counterclockwise vortex directly above the cylinder Figure 4.6-d.

In all cases of different channel heights, the vortices start from the upper surface of the cylinder, Figure 4.7-a, and then move upward with time, Figure 4.7-b, until they separate from the cylinder surface to form either a pair of vortices, as in the cases of low S values, Figure 4.7-c, or one big vortex, as in the cases for high values of S, as in Figure 4.7-d.

The pressure contours around the cylinder, Figure 4.8, gives the steady state pressure distribution inside the micropump. For all the cases studied, there are always two important regions to note in the pressure distribution inside the micropump. The first

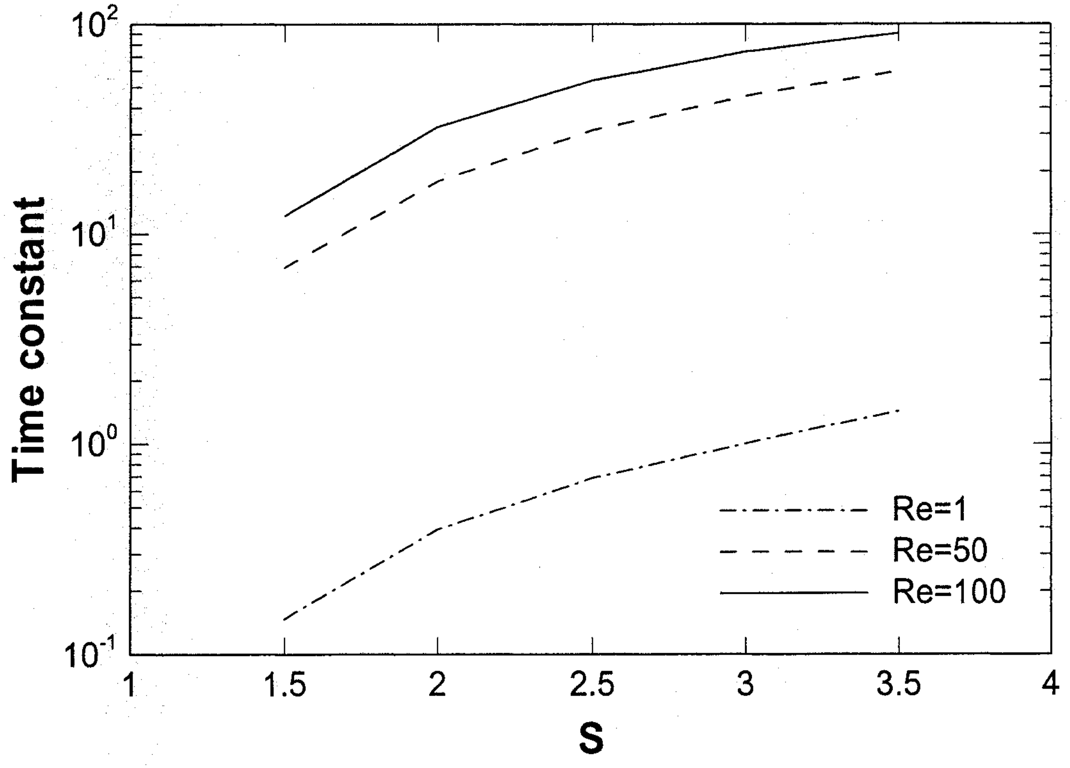

Figure 4.5: Change of the time constant with increasing channel height S

($\in = 0.95$, $\Delta P^* = 0$ and $Re = 1$)

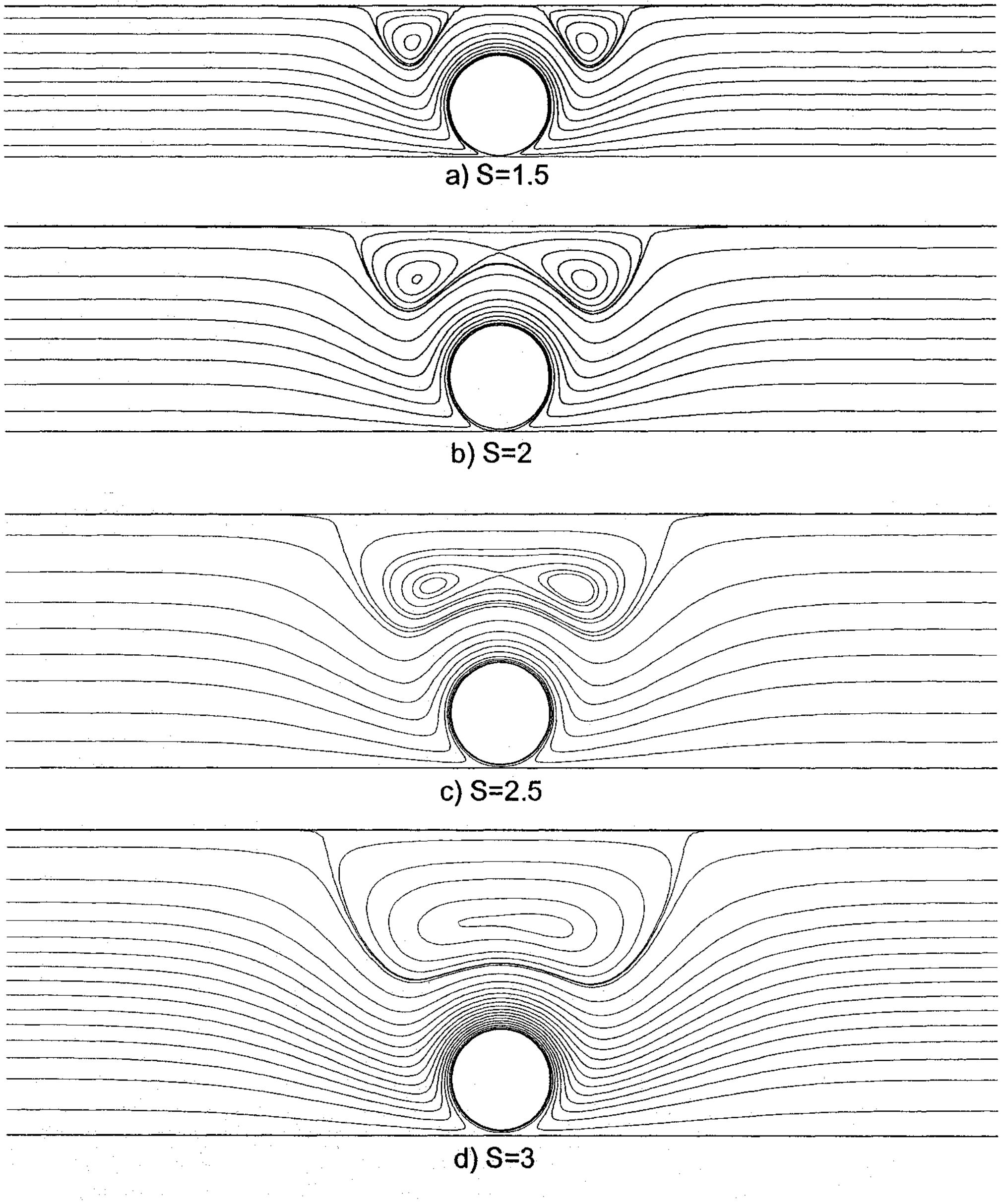
a) S=1.5

b) S=2

c) S=2.5

d) S=3

Figure 4.6: Steady state stream lines at different channel height S ($\in = 0.95$, $\Delta P^* = 0$ and $Re = 1$).

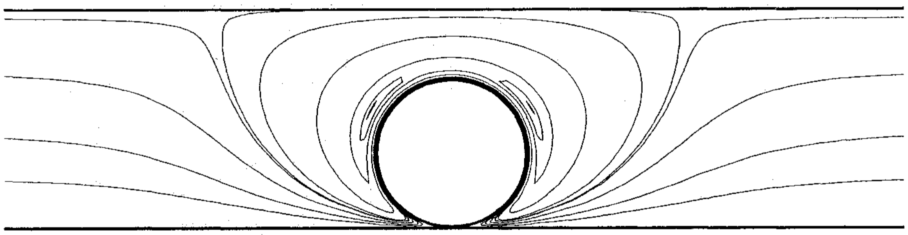

t*=0.48e-3

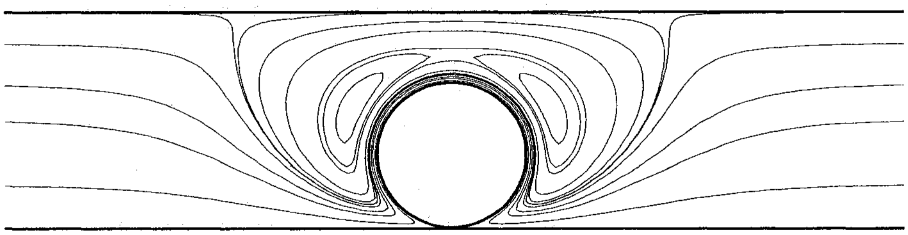

t*=4.8e-3

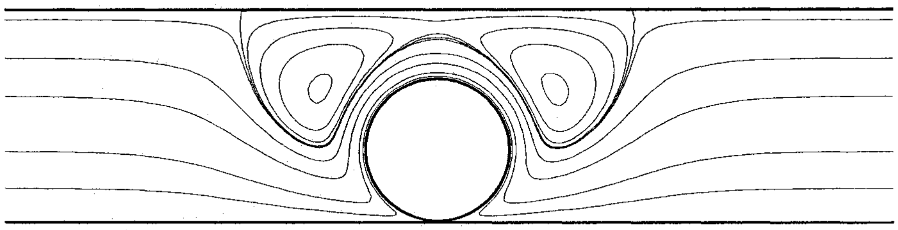

t*=31.98e-3

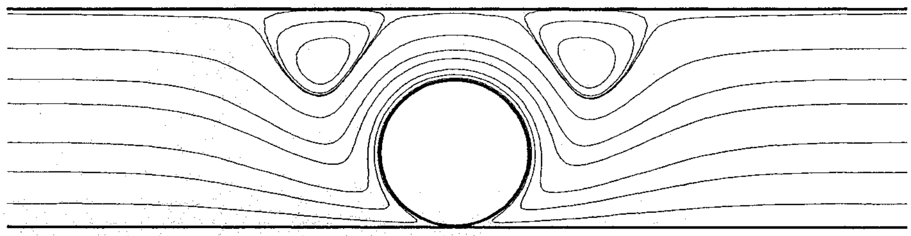

Steady state

Figure 4.7: Streamlines at different times
($S = 1.5$, $\in = 0.95$, $\mathit{\Delta}P^* = 0$, $Re = 1$).

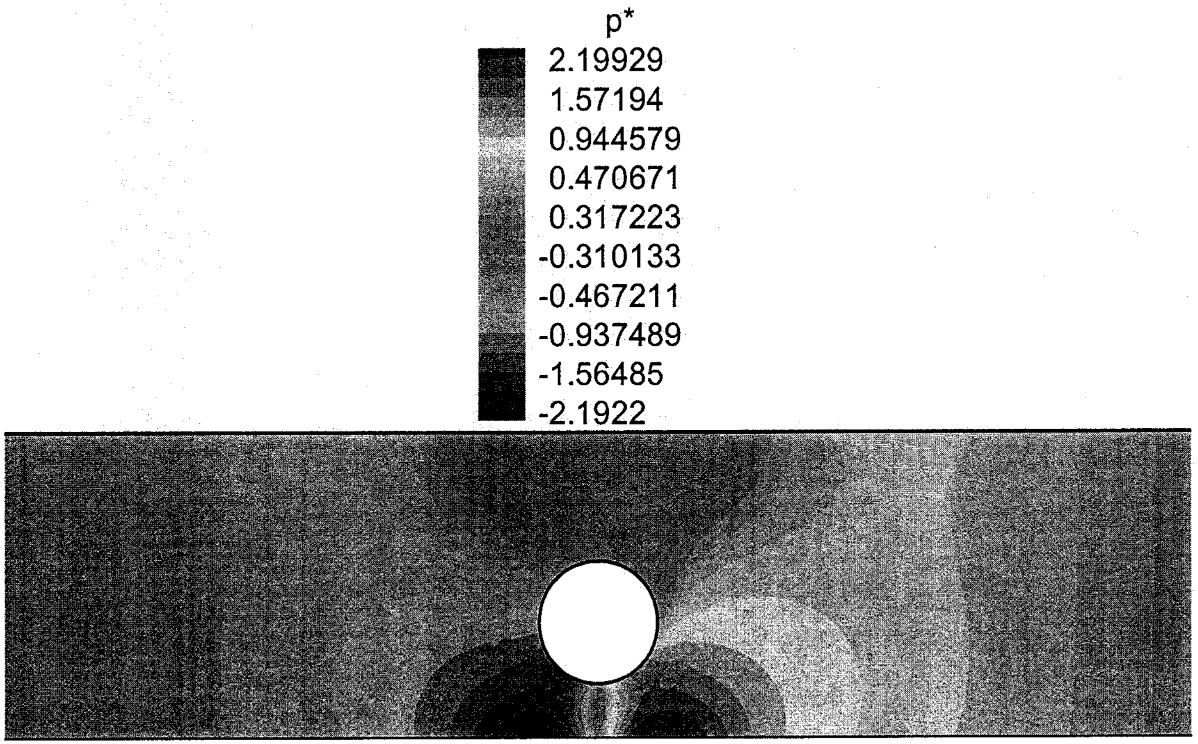

Figure 4.8: Pressure contours (S = 2.5, $\in = 0.95$, $\Delta P^* = 0$, Re = 1).

region is the one below the cylinder on the downstream side where the highest pressure inside the micropump exists. The reason for the high pressure in this region is the existence of the lower wall, which obstructs the vertical component of the cylinder surface velocity, and consequently the fluid velocity in this region, creating a semi-stagnation zone below the cylinder. The second region exists below the cylinder on the upstream side, where the lowest pressure inside the micropump exists. The reason for this low pressure is, similarly, due to the fact that the vertical component of the cylinder surface velocity is directed away from the lower wall, creating a suction zone in which the pressure is significantly reduced. It must be noted that two similar zones opposite to those below the cylinder exist on the upper surface of the cylinder in cases of low eccentricities and low channel heights. However, the pressure values are less than those on the lower walls because the cylinder is always closer to the lower wall than to the upper wall. Increasing the channel height was found to decrease the pressure difference between the high and low pressure zones due to the increase in the gap size below the cylinder. This is very clear in Figure 4.9. It has to be noted that, according to this pressure distribution, the drag force due to pressure on the cylinder will be always directed upstream, which results from these high and low pressure regions on the lower cylinder surface.

When the change of the drag coefficient with the channel height is examined, it was found to decrease with increasing the channel height, as shown in Figure 4.10. There are two reasons for this decrease. The first one is the reduction in the pressure difference between the high and low pressure zones below the cylinder when the channel height is increased. This causes a reduction in the horizontal component of the pressure force on

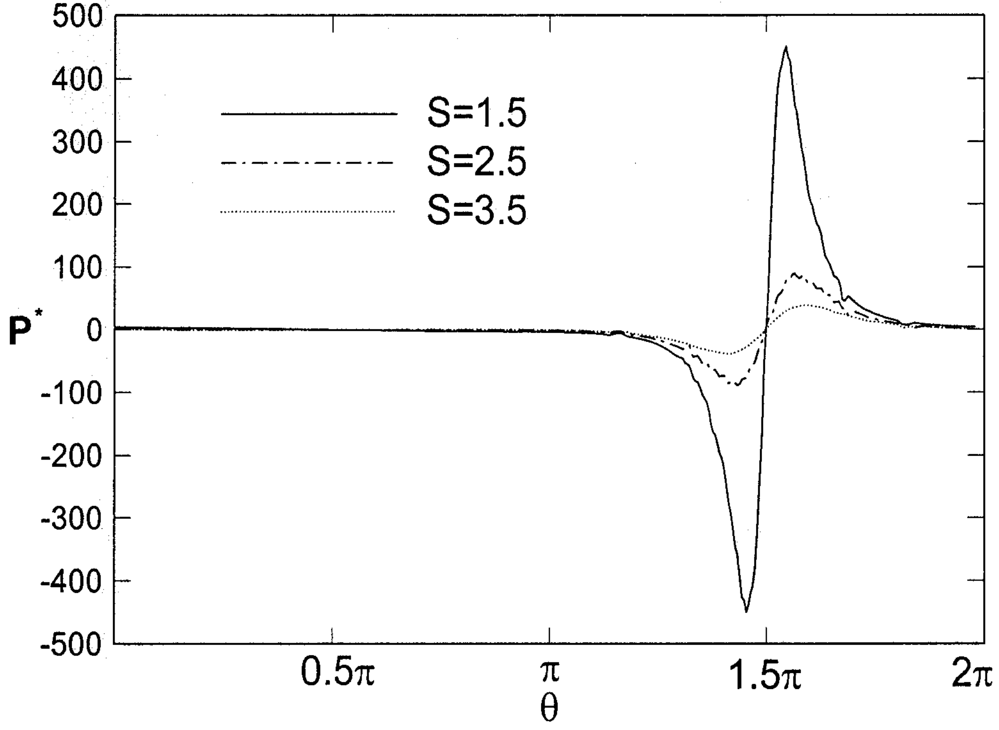

Figure 4.9: Pressure distribution on cylinder surface at different channel heights

($\in = 0.95$, $\Delta P^* = 0$, $\mathrm{Re} = 1$).

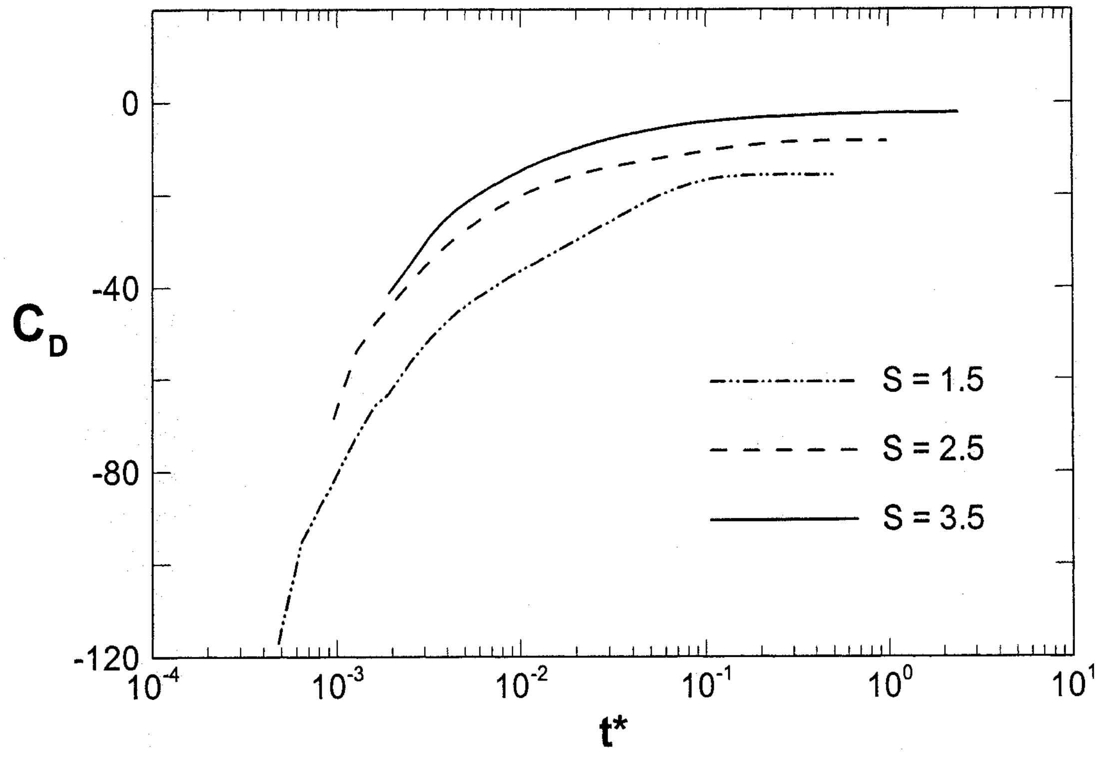

Figure 4.10: Change of drag coefficient with time at different channel heights ($\in = 0.95$, $\Delta P^{*} = 0$, $Re = 1$).

the cylinder and consequently a reduction in the drag coefficient. The second reason for the reduction in the drag coefficient with increasing the channel height is the reduction in the shear rate on the upper cylinder surface with an increase in the size of the gap between the cylinder and the upper wall, Figure 4.11. As a result, viscous forces are reduced on the cylinder upper surface. Yet, it must be noted that the effect of increasing the channel height is opposed by the effect of the merging of the two vortices that exists in cases of small channel heights to form a bigger vortex directly above the cylinder. The presence of the large vortex above the cylinder reduced the effect of increasing the channel height on the shear rate by reducing the length over which the velocity gradient occurs. In the upper gap, at low *S*, the velocity changes from its maximum value at the cylinder surface to zero at the upper wall. With the presence of the large vortex above the cylinder, the velocity gradient occurs between the cylinder upper surface and the vortex center instead of from the cylinder upper surface to the upper wall. Thus, the velocity gradient would have decreased more when the channel height is increased if it were not for the merging of the two vortices. Figure 4.12 gives the velocity distribution on the plane ($x^* = 8$) at different channel heights.

The lift coefficient was found to be one order of magnitude lower than the drag coefficient, Figure 4.13. This large difference between the values of the drag and lift coefficients is due to the nature of pressure distribution around the cylinder as shown in Figure 16. Since there are high and low pressure zones below the cylinder, and since the pressure distribution on the upper cylinder surface is of moderate value, it is clear that the upward force resulting from the high pressure zone below the cylinder will be balanced by the downward force resulting from the pressure difference between the pressure above

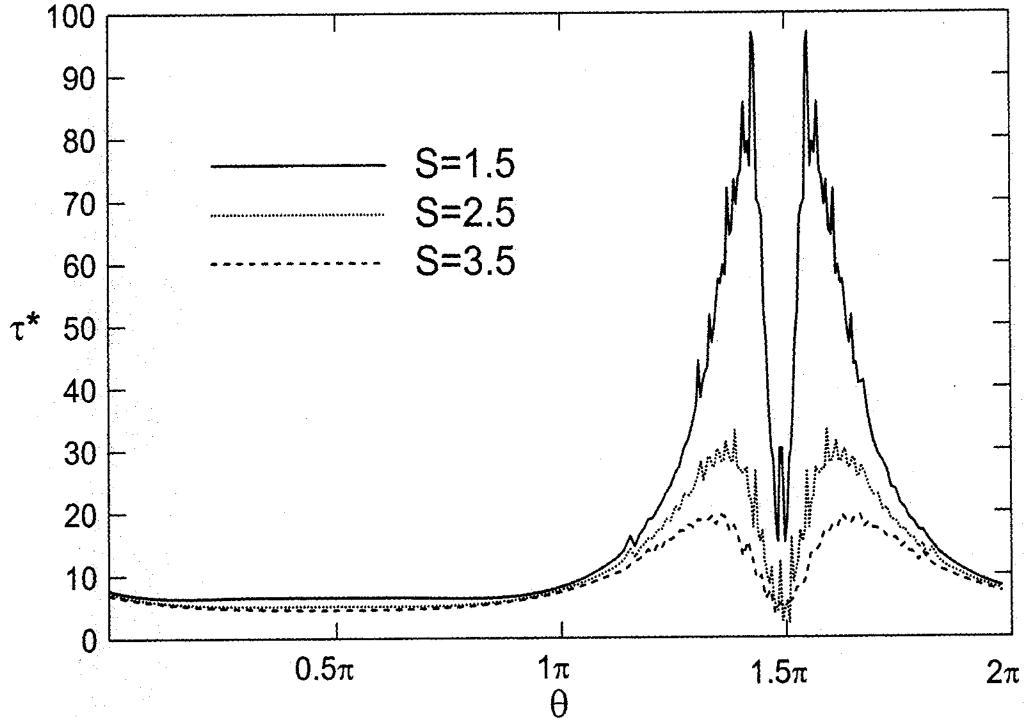

Figure 4.11: Shear stress distribution on cylinder surface at different S ($\in = 0.95$, $\Delta P^* = 0$, $\mathrm{Re} = 1$).

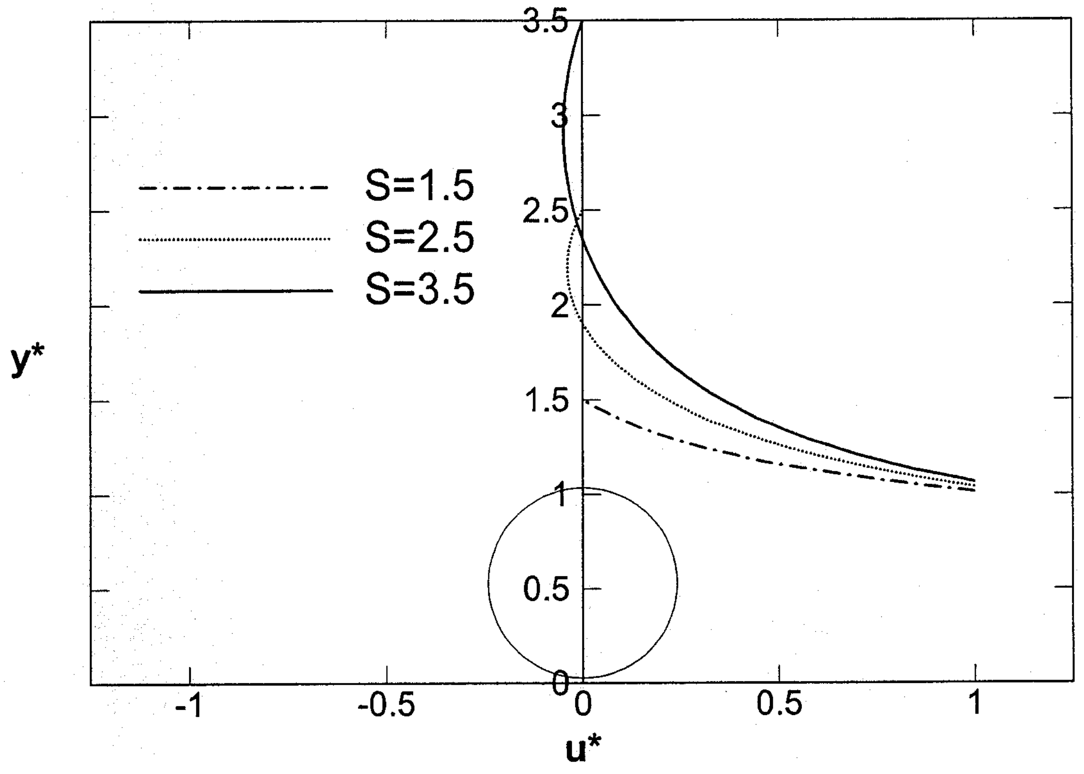

Figure 4.12: u-velocity distribution at x* = 8 for different S

($\in = 0.95$, $\Delta P^* = 0$, Re = 1).

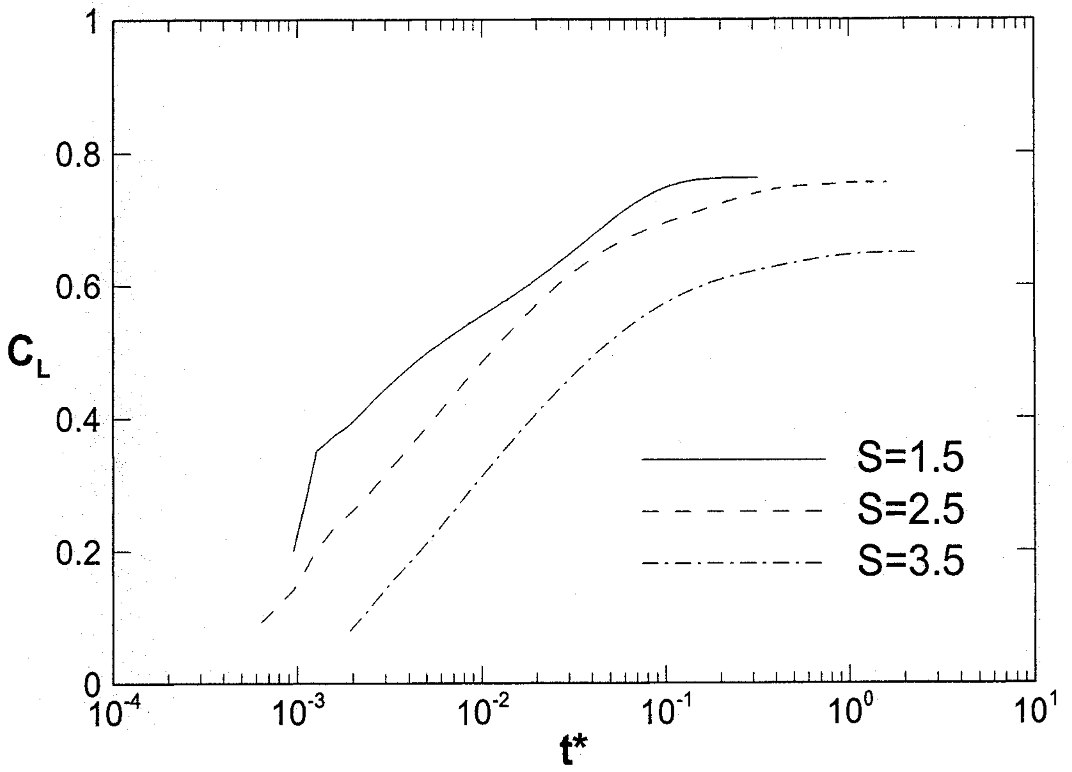

Figure 4.13: Lift coefficient vs. time at different channel heights

($\in = 0.95$, $\Delta P^* = 0$, $Re = 1$).

the cylinder and lowest pressure zone below it. The viscous contribution to the lift force is nearly zero for small Reynolds numbers because of the symmetrical nature of the flow in this case. At high Reynolds numbers, the flow becomes asymmetrical and the velocity gradient at the upper right quarter of the cylinder becomes higher than that at the upper left quarter. This results in a net positive lift force that adds to the pressure lift. When the channel height increases, the velocity gradient on the upper cylinder surface generally decrease and thus decreasing the left coefficient. Evidently, this asymmetry in the velocity gradient on the cylinder surface cannot be noticed for the cases of low Reynolds numbers, but it still cannot be neglected.

The resisting torque on the cylinder surface is due only to the viscous forces as the pressure forces are perpendicular to the cylinder surface and pass through the moment center. The moment coefficient value is highest at the beginning and decreases gradually until it reaches a constant value corresponding to the steady state operation, Figure 4.14. At the beginning of the cylinder rotation, the velocity gradient is very high because the fluid layer adjacent to the cylinder surface is moving with the same velocity as the cylinder velocity, while the fluid layer adjacent to that layer still didn't acquire this velocity. With time, the moment is diffused through the fluid layers away from the cylinder, and the velocity gradient decreases causing a reduction in the shear stress on the cylinder surface, consequently producing a reduction in the resisting torque.

The pumping efficiency is a very important parameter to consider when the performance of any pump is investigated. In the case of the viscous micropump, the net energy addition to the flow is only in the form of pressure rise (flow energy) at the pump

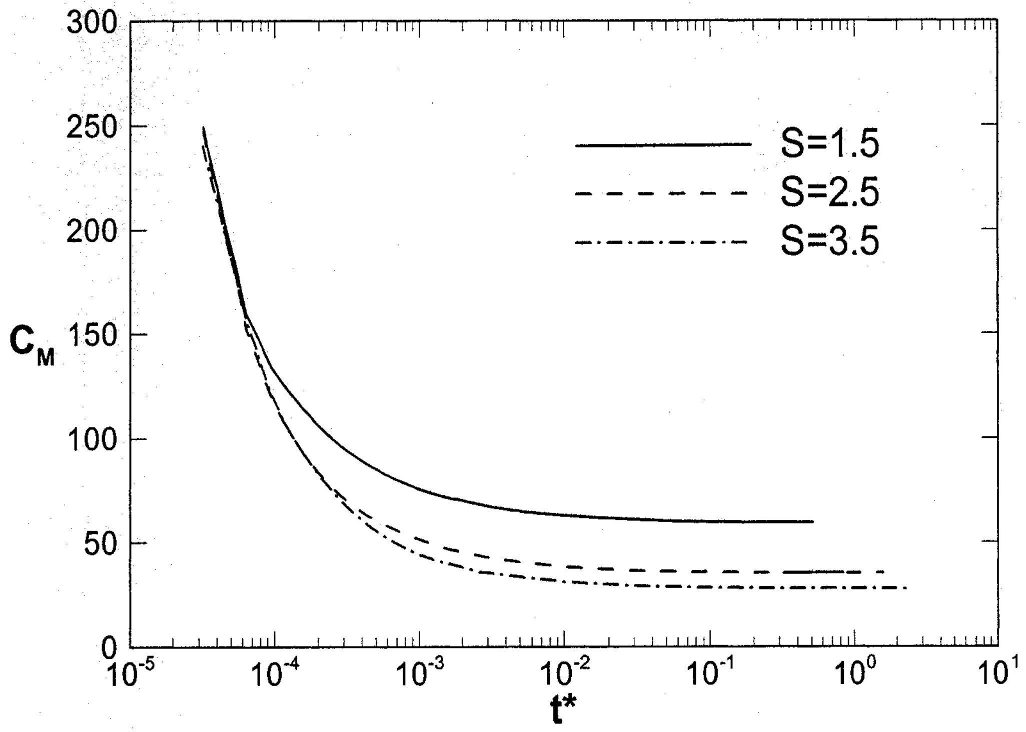

Figure 4.14: Moment coefficient vs. time at different channel heights

($\in = 0.95$, $\Delta P^* = 0$, $\mathrm{Re} = 1$).

outlet, since the kinetic energy at the inlet and exit are equal. Accordingly, the micropump efficiency can be defined as:

$$\eta = \frac{\text{Flow energy rise}}{\text{Input mechanical energy}}.$$

Therefore the micropump efficiency may be obtained from:

$$\eta = \frac{\dfrac{\dot{m}\Delta P}{\rho}}{M\omega}. \tag{16}$$

In non-dimensional terms, this reduces to:

$$\eta = \frac{\Delta P^{*} u^{*} S}{C_m \operatorname{Re}^2}. \tag{17}$$

Figure 23 shows how the efficiency η varies with time for different channel heights. It should be noted that this figure does not include any values of S higher than $S = 2$, because with the backpressure corresponding to this figure for all the tested values of S greater than $S = 2$ results in a backflow. It is clear from Figure 4.15 that increasing the channel height reduces the pumping efficiency since the velocity gradients on the cylinder surface, and hence the viscous forces, i.e. pumping forces, decrease.

4.3 Effect of rotor eccentricity

The cylinder eccentricity is a very important parameter in determining the performance of the micropump. In fact, it is the cylinder eccentricity that provides the driving force to the fluid inside the micropump channel, by introducing unequal shear stresses on the upper and lower surfaces of the cylinder. The degree of cylinder

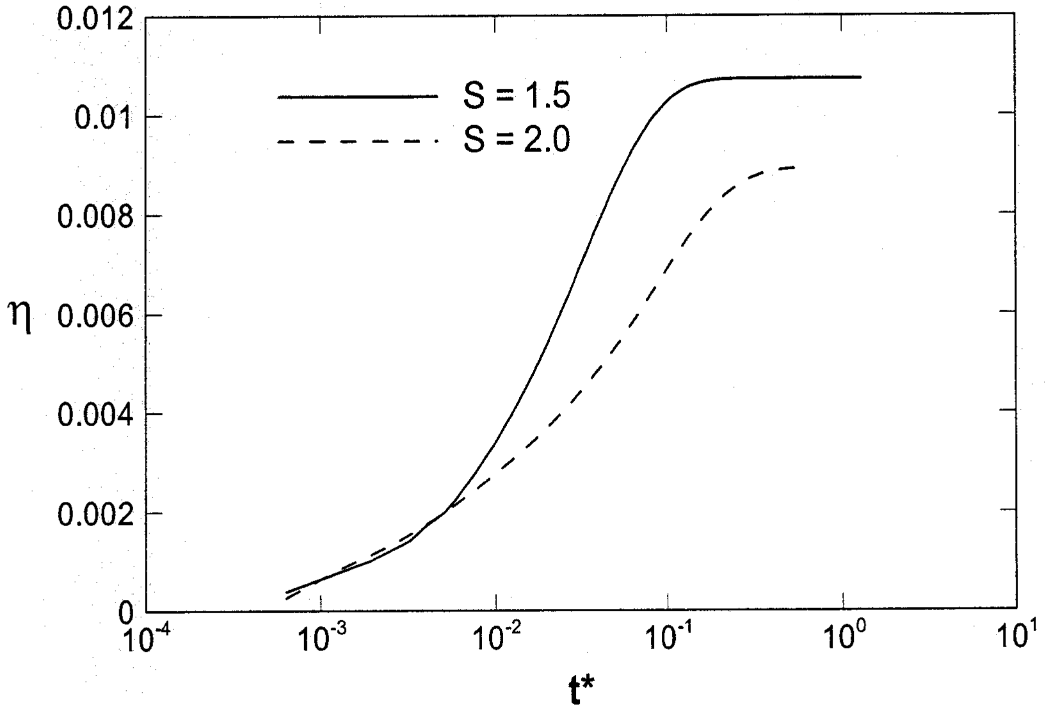

Figure 4.15: Pumping efficiency development with time

($\in = 0.95$, $\Delta P^* = 5$, Re = 1).

eccentricity determines how the micropump will operate and what flow pattern to expect. Figure 4.16 shows the different start-up curves at different eccentricities. It is clear that when the eccentricity increases the steady state average velocity inside the channel increases and micropump requires more time to reach this steady state operation. This is due to the fact that increasing the cylinder eccentricity increases the mass flow rate inside the channel directly and thus more time is needed for the viscous forces between the fluid layers to overcome the inertia of the fluid to attain this higher velocity.

If the eccentricity is set to zero, which means that the cylinder is in the center of the channel, no net flow is initiated. Instead there is a big vortex around the cylinder rotating with it in the same direction, Figure 4.17. On both sides of the cylinder vortex, two co-rotating vortices exist. All the fluid motion in the case of zero eccentricity is nearly restricted inside these three vortices, which occupies the vast majority of the whole channel. When the eccentricity is increased, the center vortex around the cylinder gradually decreases in size until it is restricted to a very thin strip around the cylinder at $\in = 0.95$. The two side vortices move toward the upper wall (the larger gap) and their change in size depends on the channel height. For the cases of small channel heights, the two side vortices decrease in size with increasing eccentricity, thus allowing for more fluid to pass through the micropump as they move toward the upper wall. For large channel heights, the vortices decrease in size at the beginning with increasing eccentricity, but then they increase in size again when they merge together to form one big vortex above the cylinder. This is characteristic of the effect of large channel heights as described in Section 4.2.

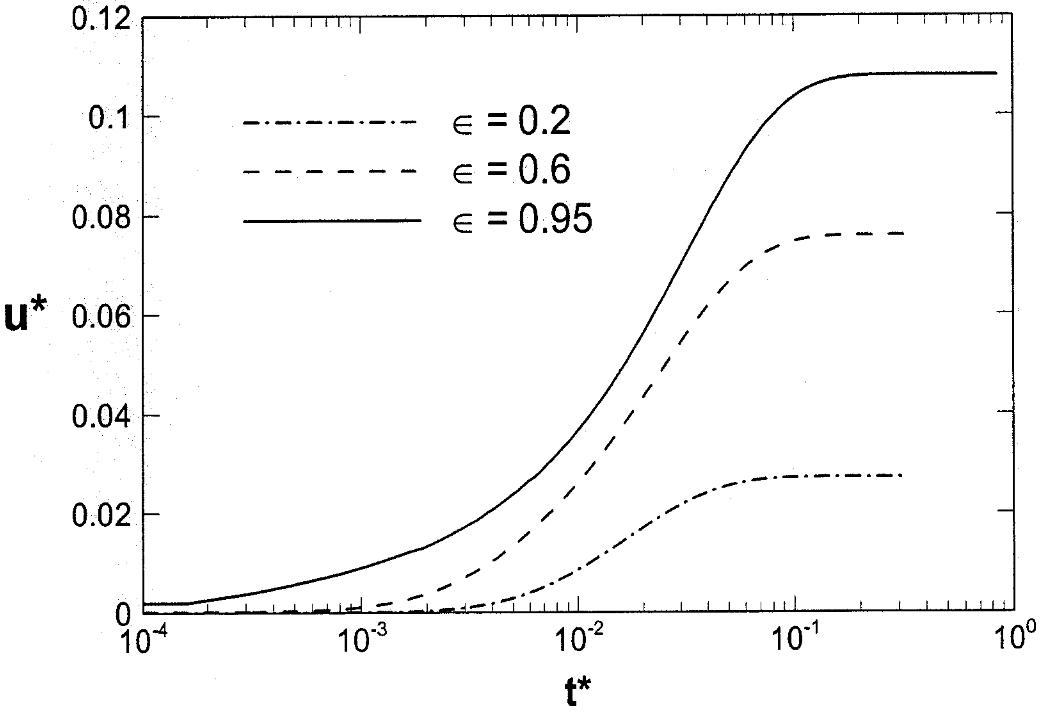

Figure 4.16: Average velocity vs. time at different rotor eccentricities

(S = 1.5, $\Delta P^* = 5$, Re = 1).

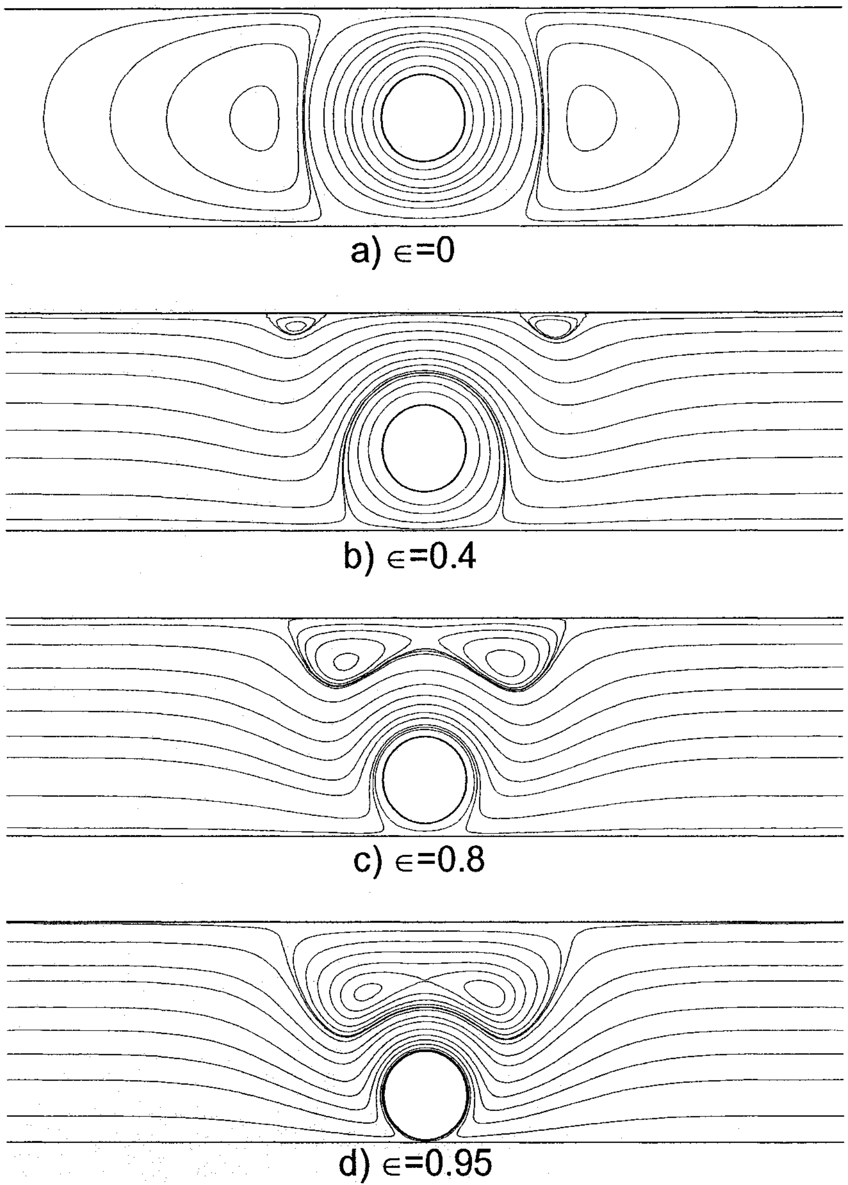

Figure 4.17: Steady state streamlines at different eccentricities

(S = 2.5, $\Delta P^* = 0$, Re = 1).

When the flow development with time is monitored, it was observed that at the beginning of each case, the center vortex around the cylinder first appears along with two vortices, one on each side of the main cylinder vortex and slightly shifted towards the upper wall, Figure 4.18-a. The size of the cylinder vortex remains nearly the same from the beginning until steady state is reached. For the cases of small channel heights, the two side vortices start to decrease in size and move upward until they finally come to rest separate from each other at the upper wall. For the cases of large channel heights there is one big vortex above the cylinder vortex in the form of a crescent with two very small vortices in its branches, instead of the two side vortices associated with small channel heights, Figure 4.18-b. These two small vortices grow gradually with time until they occupy most of the crescent vortex. For cases of small eccentricities, these two vortices split from each other with time to form two separate small vortices resting on the upper wall as shown in Figure 4.18-d, while for cases of large eccentricities, they merge together to form one big vortex above the cylinder, Figure 4.6-d.

When the dependence of the steady state drag coefficient upon the cylinder eccentricity is examined, it was found that it is always negative, and that it increases with an increase in the cylinder eccentricity. This is mainly due to the increase in the pressure drag as the viscous contribution to the drag is much smaller than that of the pressure (e.g. in cases of low eccentricities, the viscous drag is one order of magnitude less than the pressure drag). Figure 4.19 shows how the drag coefficient changes with time at various eccentricities. The value of the steady state drag can be found at the end of the simulation time when the drag coefficient stabilizes at a constant value.

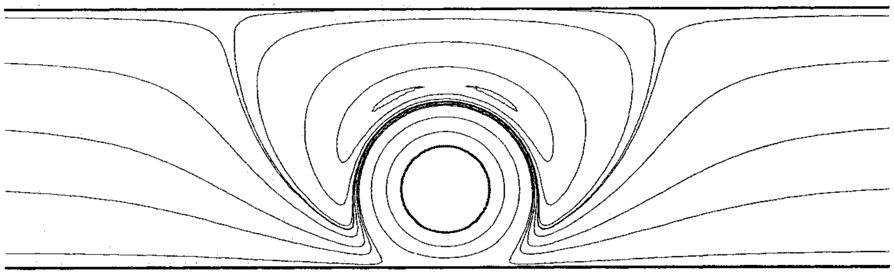

(a) t*=9.6e-3

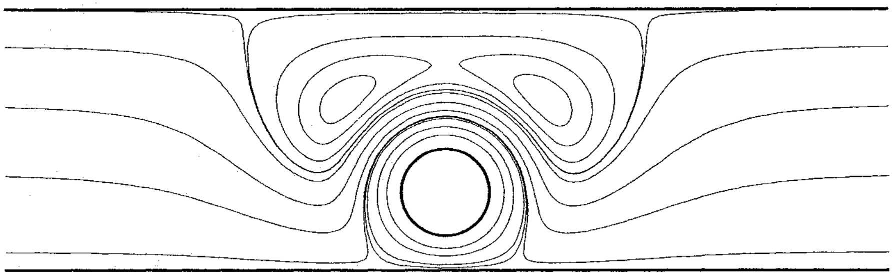

(b) t*=79.96e-3

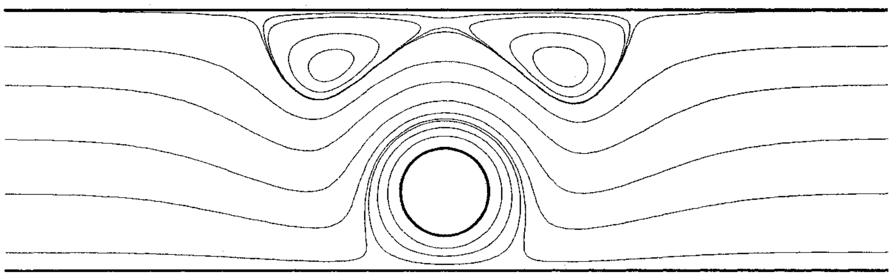

(c) t*=0.2399

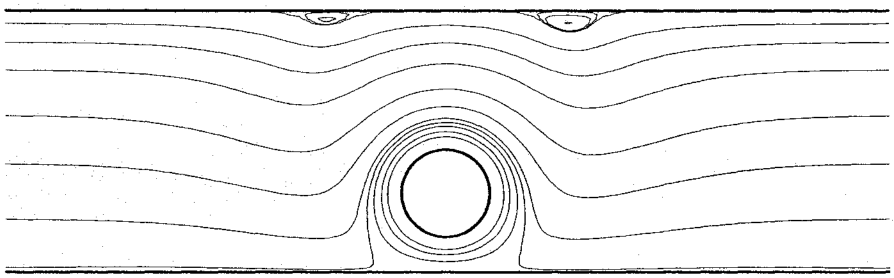

(d) Steady state

Figure 4.18: Streamlines at different times

($S = 3$, $\in = 0.6$, $\Delta P^{*} = 0$ and $Re = 1$).

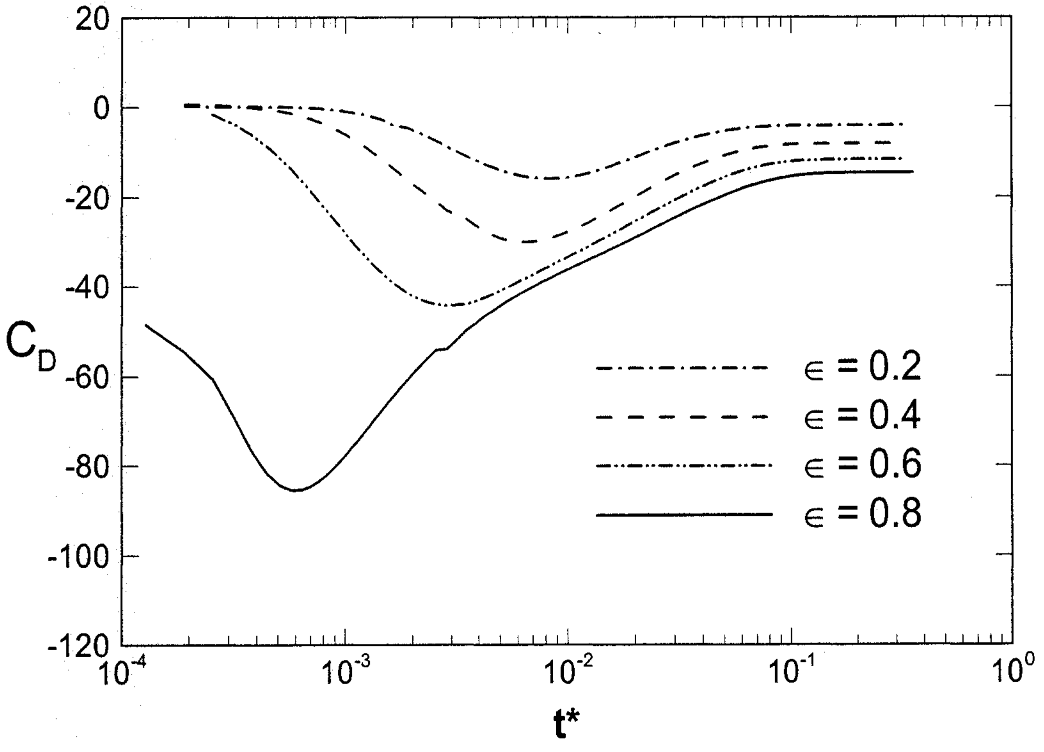

Figure 4.19: Drag coefficient vs. time at different eccentricities

($S = 1.5$, $\Delta P^{*} = 0$, $Re = 1$).

The time dependence of the drag coefficient at different eccentricities is more complicated as shown from Figure 4.19. At low eccentricities, the drag coefficient is initially a small value, increases with time, then finally decreases and returns to its steady state value. For high eccentricities the drag coefficient is initially a large value and gradually decreases to its steady state value. In order to explain this curve, the two components of the drag force, the pressure and viscous drags, should be studied independently. Figure 4.20 shows the variation of the pressure and viscous drags with time at $\in = 0.4$. At low eccentricities, the pressure in the semi-stagnation zone behind the cylinder increases with time until it reaches a maximum value, and then afterwards decreases slightly. This is due to the velocity distribution in the lower gap with time. At the beginning, the fluid motion is restricted to the vicinity of the cylinder and the lower wall obstructs the vertical component of the fluid velocity, raising the pressure and forming the semi-stagnation zone. With time, and due to this high pressure zone, the fluid's velocity increases and is redirected away from this zone, consequently reducing its pressure. For this reason, the pressure drag begins to increase with time initially, and subsequently decreases to a smaller value. Figure 4.21 shows the change of the pressure distribution on the cylinder surface with time.

In addition, the viscous drag changes its direction with time for low eccentricities. This is due to the fact that the fluid exerts a force to the left at the upper part of the cylinder and another force to the right at the lower part of the cylinder. Initially, the velocity gradients on both the upper and lower halves of the cylinder are nearly the same, but are slightly higher on the upper half due to the presence of the two co-rotating vortices located very close to the cylinder on both sides on its upper half. These two

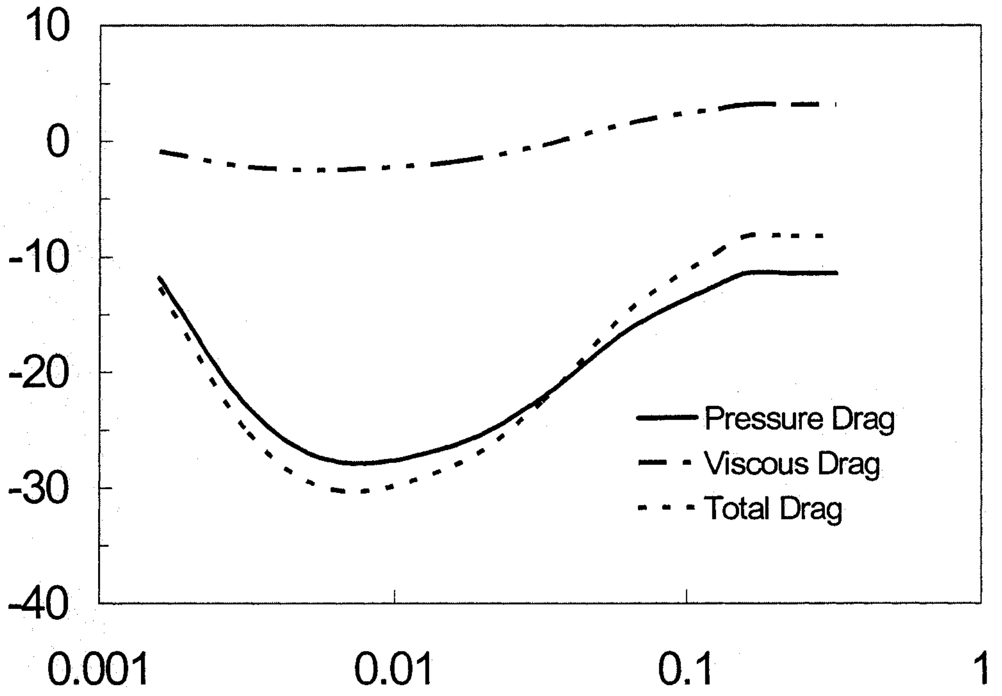

Figure 4.20: Viscous, pressure and total drag coefficients for $\in = 0.4$

($S = 1.5$, $\Delta P^* = 0$, $Re = 1$).

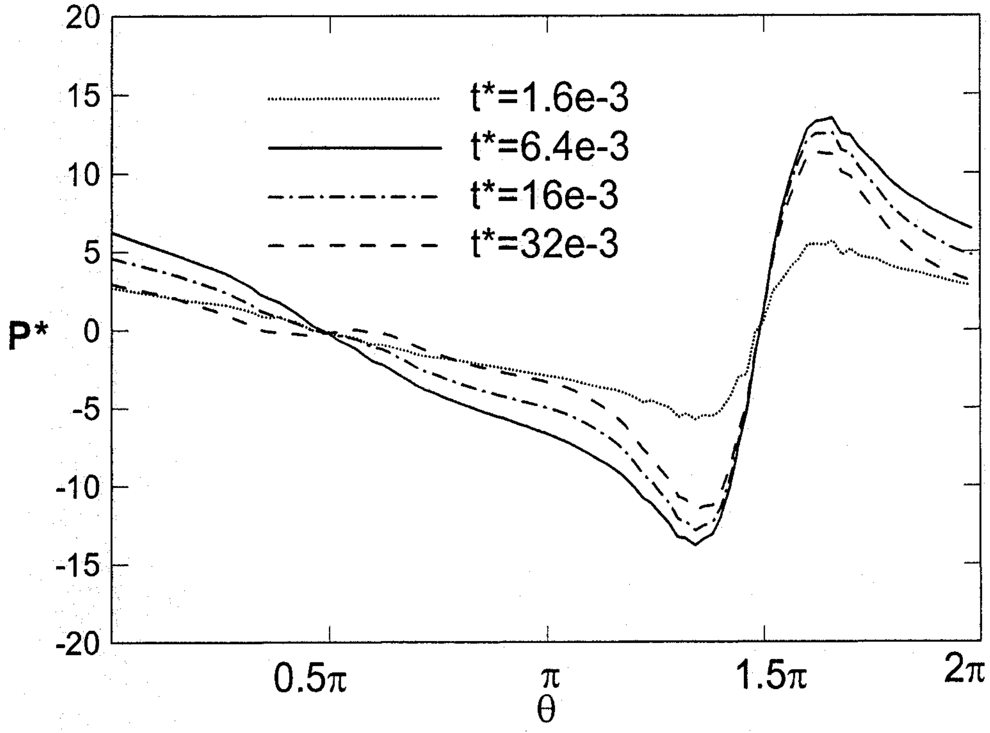

Figure 4.21: Pressure distribution on cylinder surface at different times

($S = 1.5$, $\in = 0.4$, $\Delta P^* = 0$, $Re = 1$).

vortices help increase the velocity gradient on the upper surface, thus increasing the upper viscous drag, which is toward the left. With time, and with the development of the flow field, these two vortices move away from the cylinder towards the upper wall, thus reducing the velocity gradient on the upper cylinder surface. Since the velocity gradient on the lower surface is nearly constant with time, the effect of the viscous drag on the lower cylinder surface becomes higher than that on the upper surface, so the overall viscous drag is to the right.

At high eccentricities the lower gap between the cylinder and the lower wall is so small that the obstruction of the lower wall causes the pressure reaches its maximum very rapidly. The pressure then decreases with time due to the velocity development in the semi-stagnation zone. The pressure drag naturally follows the same trend of the pressure. The viscous drag is found to remain nearly constant with time compared to the cases of low eccentricities. This occurs due to the very sharp change in the direction of the streamlines in the area downstream from the cylinder in the lower gap, which initially induces very high velocity gradients. The value of the shear stress on the lower cylinder surface in this case is much higher than the shear stress value on the upper surface. For this reason, the total viscous drag is directed to the right (i.e. positive drag).

The effect of the eccentricity on the lift coefficient is much simpler than the its effect on the drag coefficient as shown in Figure 4.22. As shown in the figure, the lift coefficient increases with increasing the cylinder eccentricity. In order to be able to explain this trend, it has to be remembered that the lift coefficient is the result of the non-symmetrical velocity gradients on the left and right halves of the cylinder. When the eccentricity increases, the upper gap size increases which magnifies the difference

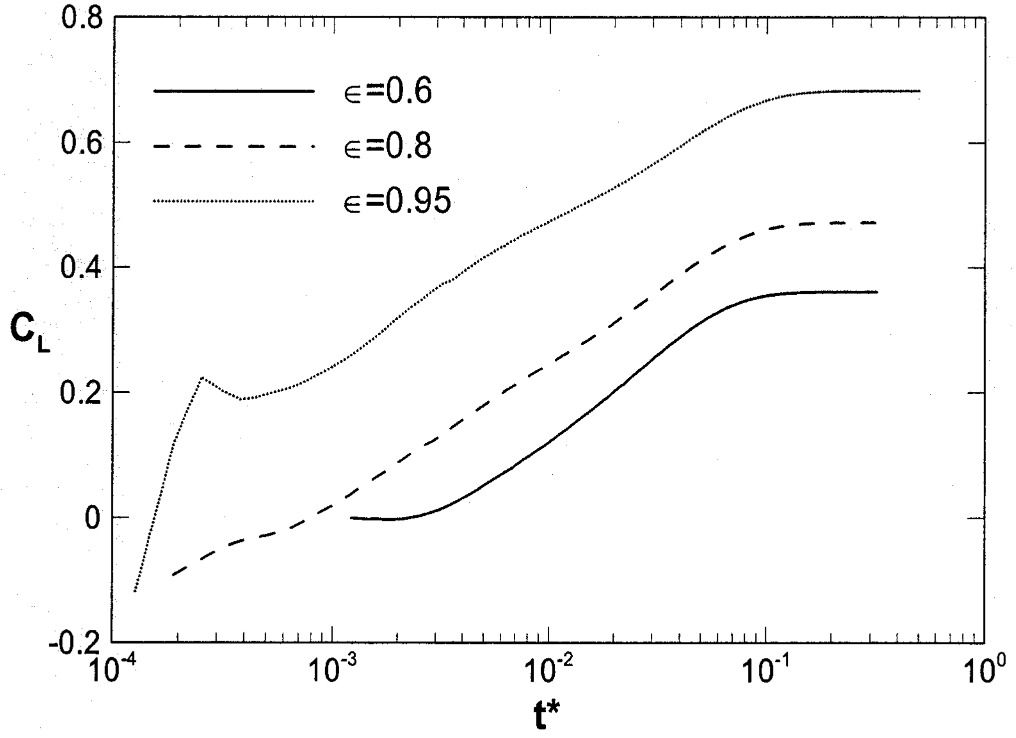

Figure 4.22: Change of lift coefficient with time at different eccentricities ($S = 1.5$, $\Delta P^* = 0$, $Re = 1$).

between the upstream and downstream velocity gradients on the cylinder upper surface. This causes the increase of the left coefficient as described before.

The variation of the moment coefficient with time at different eccentricities is shown in Figure 4.23. It is clear that the moment coefficient increases with increasing the eccentricity. This is due to the reduction in the gap size between the cylinder and the lower wall, resulting in an increase in the shear stress on the cylinder surface. Figure 4.24 shows the shear stress on the cylinder surface at different eccentricities.

The dependence of the pump efficiency on the cylinder eccentricity is shown in Figure 4.25. The negative part of the curves corresponding to $\in = 0.4$ & 0.6 indicates that, for this part of the curve, the pump still could not overcome the backpressure, so a backflow occurs, and thus a negative mass flow rate results. However, the pump eventually generates higher pressure than the backpressure with time and the net flow rate becomes positive. Figure 4.25 shows that the dependence of the efficiency on the cylinder eccentricity has a maximum. According to equation 17, the efficiency is a function of ΔP^*, S, u^*, C_M and Re. Since ΔP^*, S, and Re are kept constant when the effect of eccentricity is studied, it becomes apparent that the efficiency is a function in u^* and C_M. For low eccentricities, the average velocity u^* is small, so the efficiency should be small. However, the moment coefficient C_M is also small due to the low velocity gradient on the cylinder surface, which tends to increase the efficiency. For the cases of high eccentricities, the situation is reversed. The average velocity u^* is high, which tends to increase the efficiency, but the moment coefficient C_M is also high, which tend to decrease the efficiency. As a result, the efficiency is expected to have its highest value at moderately high cylinder eccentricities where the average velocity is high and the

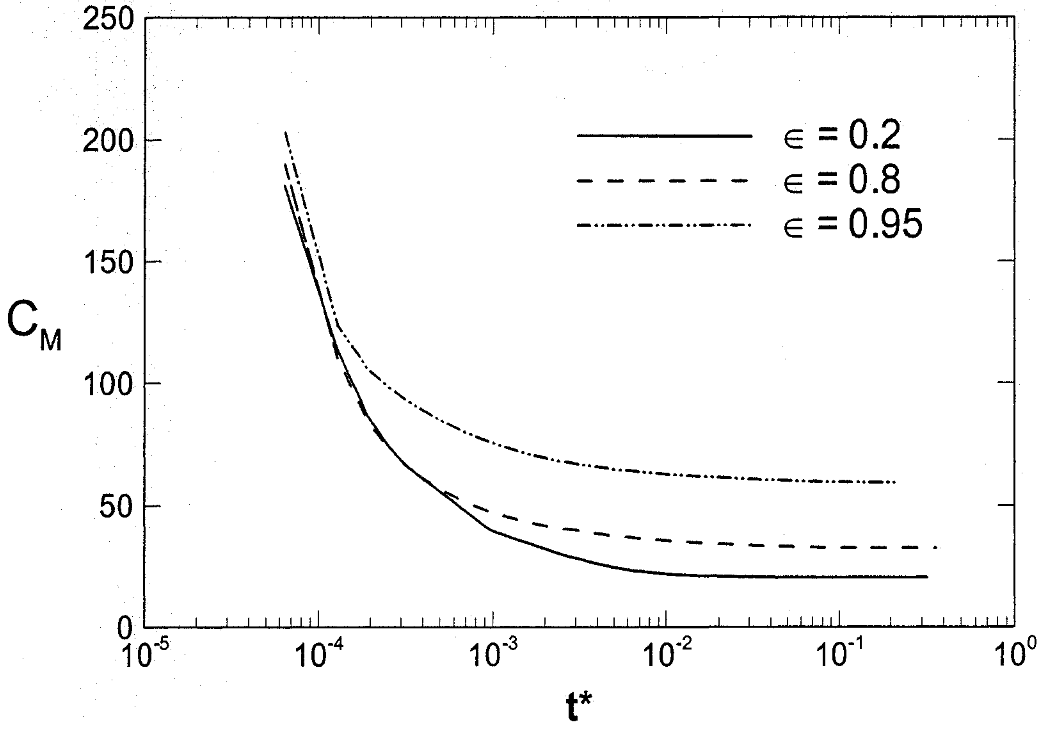

Figure 4.23: Cylinder Moment coefficient vs. time at different eccentricities

($S = 1.5$, $\in = 0.4$, $\Delta P^* = 0$, $Re = 1$).

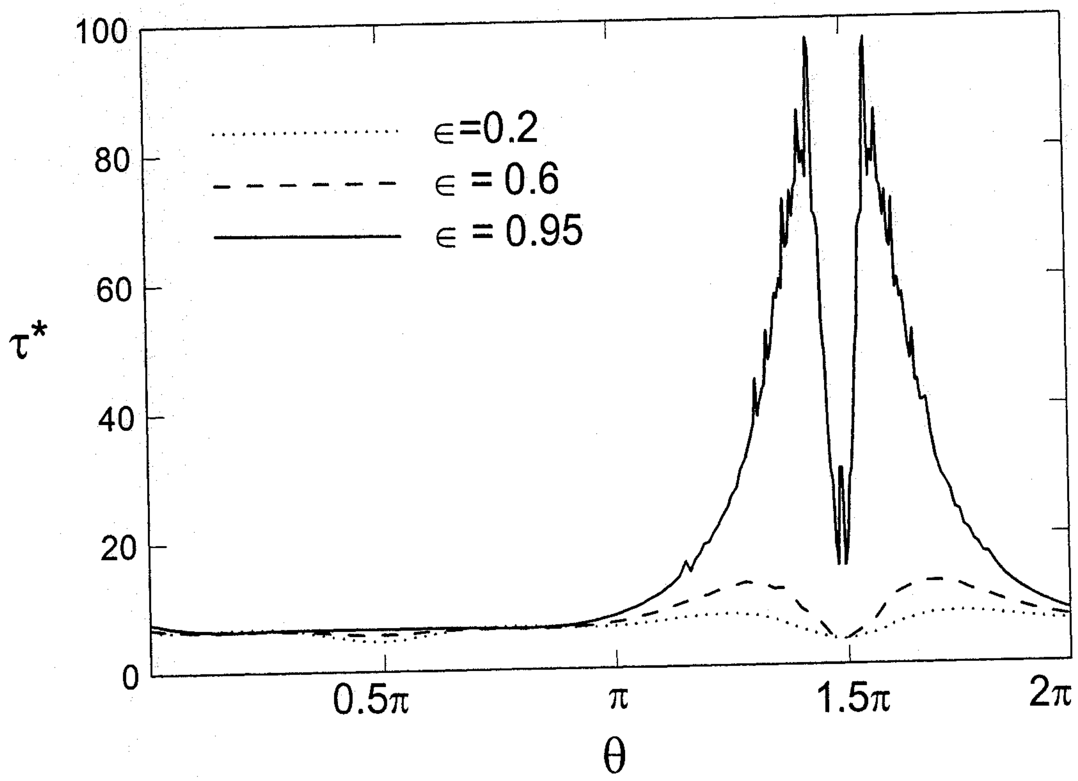

Figure 4.24: Shear stress distribution on cylinder surface at different eccentricities

(S = 1.5, $\Delta P^{*} = 0$, Re = 1).

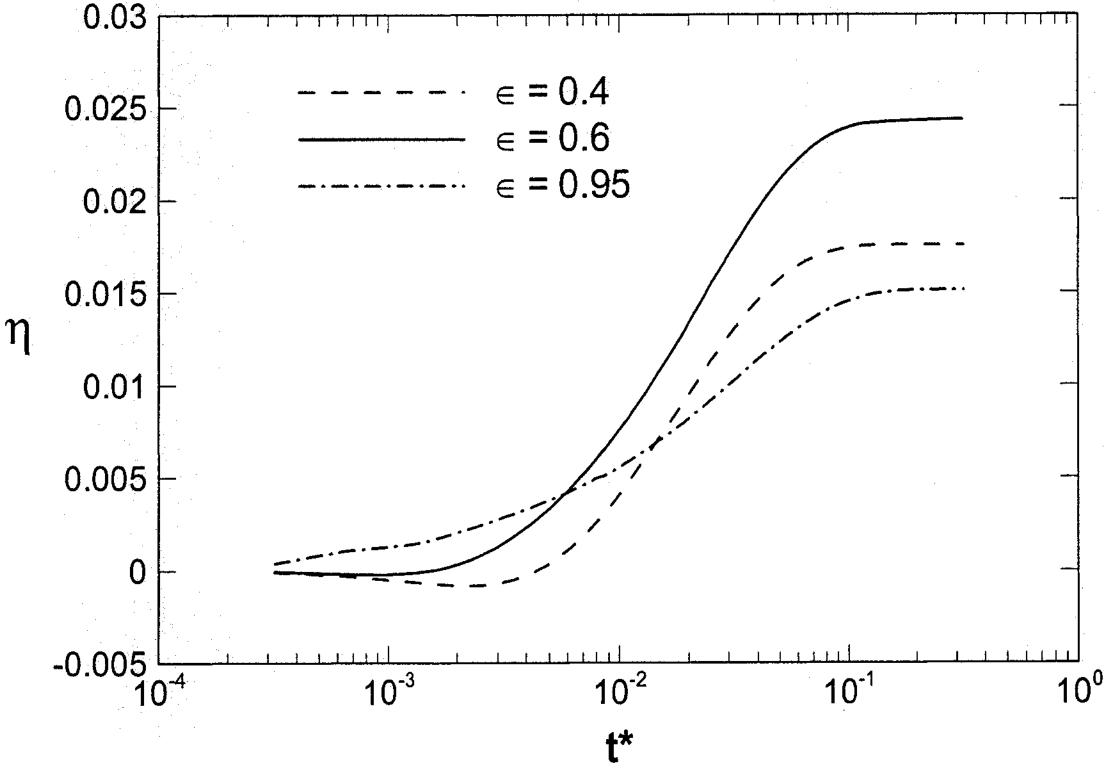

Figure 4.25: Pumping efficiency at different eccentricities

(S = 1.5, $\Delta P^* = 10$, Re = 1).

moment coefficient is still relatively small. This can be seen in Figure 4.25, which shows how the efficiency first increases and then decreases with increasing the cylinder eccentricity.

4.4 Effect of Reynolds number

The Reynolds number for the micropump is based on the rotor angular velocity, and not on the average fluid velocity in the micropump. In this case, since the power input equals the resisting viscous torque multiplied by the cylinder angular velocity, the Reynolds number determines the amount of power input to the micropump. In this section, the effect of Reynolds number on the flow field inside the micropump will be studied in detail. Most of the cases presented in this study correspond to the value Re = 1, since this is the most probable operating condition for the micropump. Some cases were studied at Re = 10, 50, and 100 in order to demonstrate the effect of increasing the Reynolds number beyond the operating range.

When Reynolds number is increased, the flow field pattern changes in the vicinity of the cylinder. Before the effect of increasing Reynolds number on the flow pattern is examined, it has to be mentioned that increasing Reynolds number constantly increases the flowrate inside the micropump. If initially two vortices exist above the cylinder, as in the case for small channel heights, increasing the Reynolds number renders the downstream vortex to be convected more downstream and gradually increasing in size. Contrary to the downstream vortex, the upstream vortex decreases in size with increasing Reynolds number in order to allow more fluid to pass in the channel above the cylinder. At very high Reynolds numbers, the upstream vortex disappears completely, Figure 4.26.

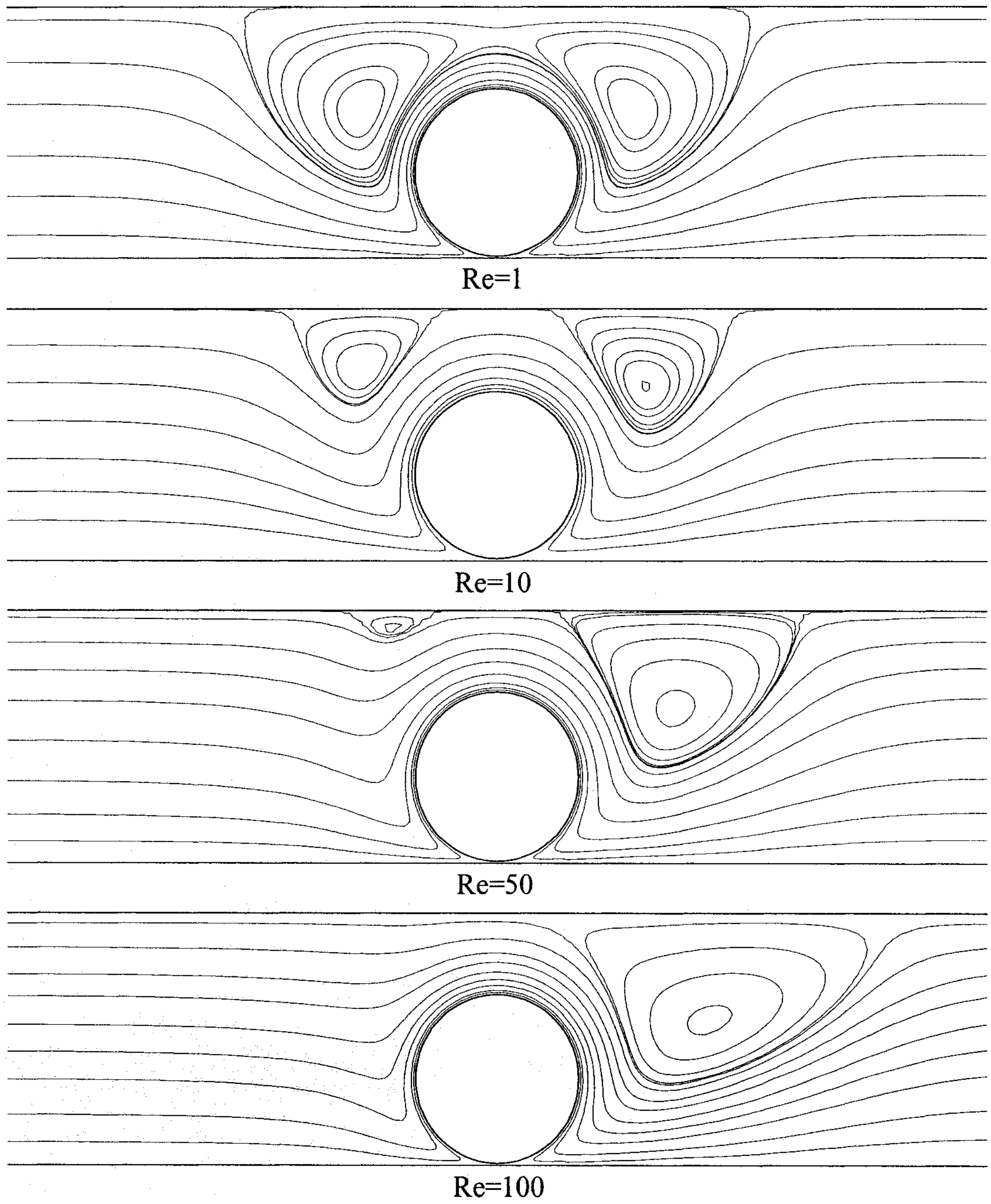

Figure 4.26: Streamlines at different Reynolds numbers
($S = 1.5$, $\in = 0.95$, $\Delta P^* = 10$).

If initially only one vortex exists above the cylinder, as in case for large channel heights, when Reynolds number is increased this large vortex is convected downstream, and gradually increases in size.

Figure 4.27 shows the start-up curves of the micropump at different Reynolds numbers. It has to be mentioned that the non-dimensional velocity is normalized by the cylinder surface velocity, which increases linearly with increasing Reynolds number. So even though the non-dimensional velocity for higher Reynolds number is less than that for low Reynolds number, the actual fluid velocity is much higher. The starting time for the three curves is different because the non-dimensional time is calculated through Equation 5, which is:

$$t^* = \frac{t}{\frac{2\pi}{\omega}} = \frac{t\omega}{2\pi}$$

So even if the time step was smaller for cases of high Reynolds number, the non-dimensional time will be larger due to the large rotational velocity of the cylinder.

The flow development with time at Re = 50 is shown in Figure 4.28. At the beginning and as in all cases, two small vortices exist above the cylinder and are encircled by one big vortex. With time, they start to separate form each other and rest on the upper channel wall. The upstream vortex start to decrease in size in order to allow for more flow to pass as a result of the high cylinder surface velocity, while the downstream vortex increase in size and is convected away under the momentum of the flow. At steady state, the upstream vortex become very small in size and might totally disappear for very high Reynolds numbers.

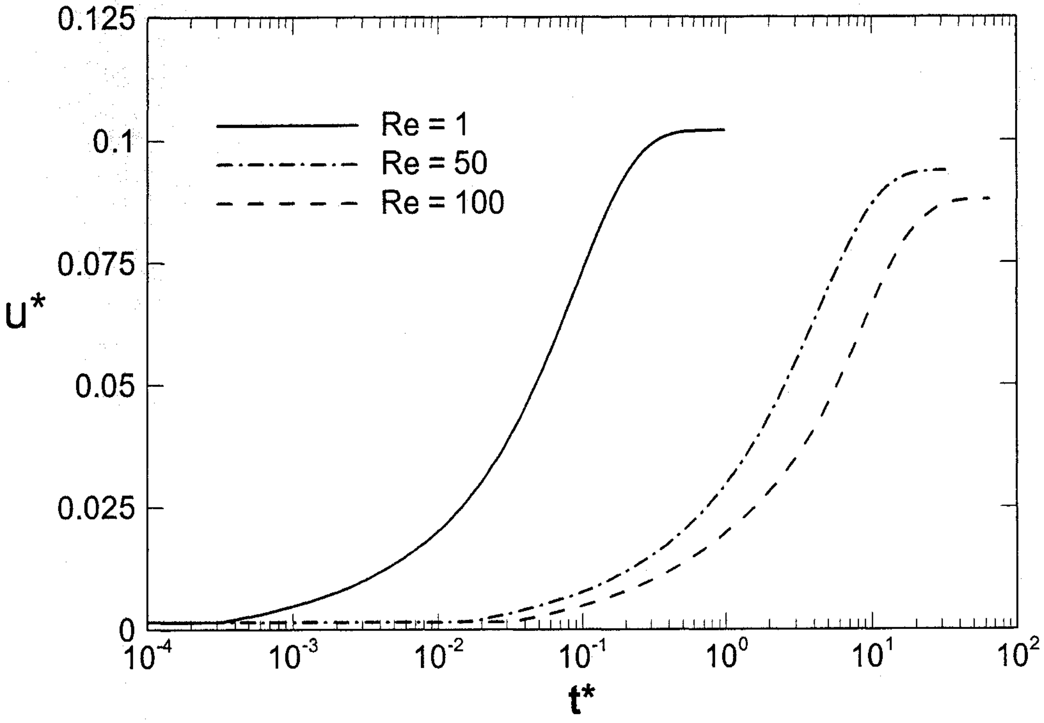

Figure 4.27: Average velocity inside the channel vs. time at different Re

(S = 1.5, $\in = 0.95$, $\Delta P^* = 0$).

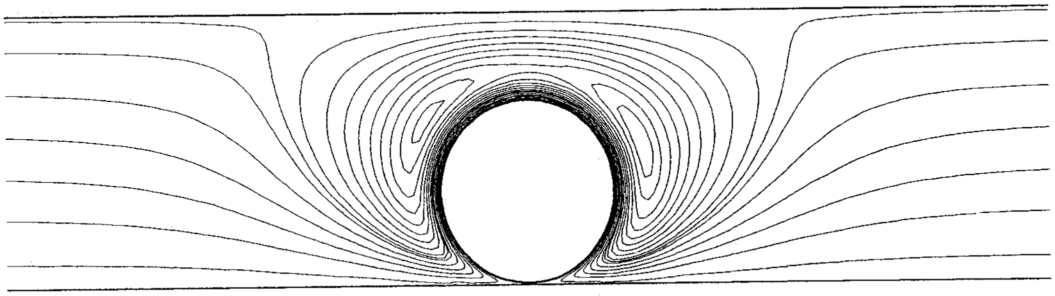

t*=0.16

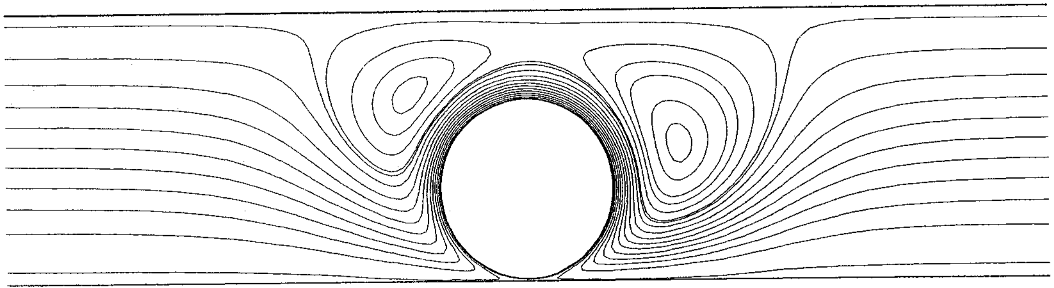

t*=1.12

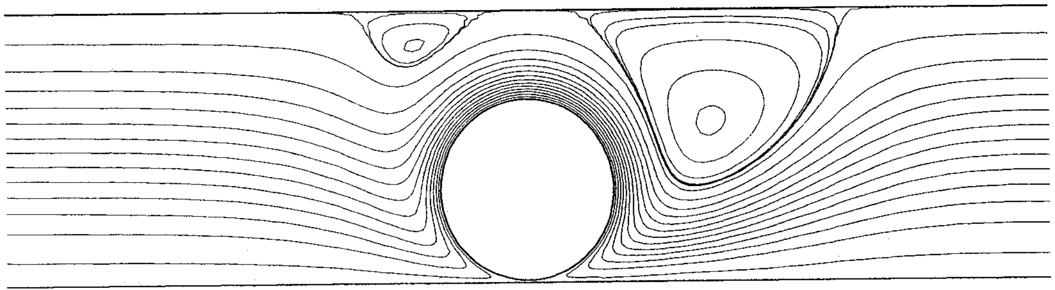

t*=4

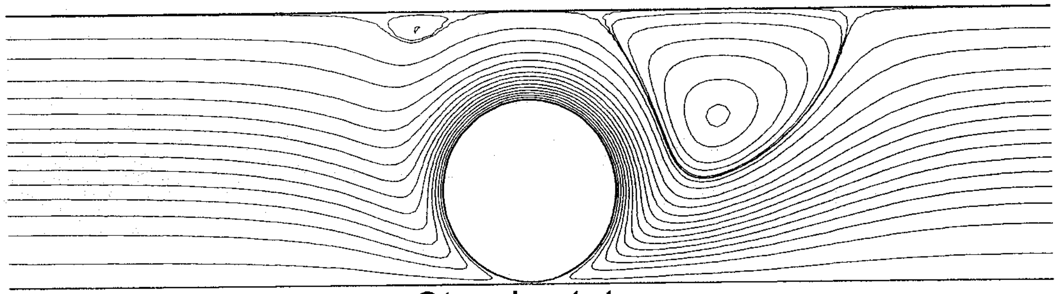

Steady state

Figure 4.28: Streamlines at different times at Re = 50 ($S = 1.5$, $\in = 0.95$, $\Delta P^* = 10$).

It was observed that the drag coefficient decreased with increasing Reynolds number. This is due to the increase in the cylinder surface velocity, which is used for normalizing the drag force. Therefore, the drag coefficient is expected to decrease as Reynolds number increases. The drag coefficient also decreases with time due to the reduction in the viscous forces on the cylinder surface, as the pressure distribution around the cylinder in cases of high eccentricity remains nearly constant with time. The lift and moment coefficients were also found to decrease with increasing Reynolds number as shown in Figure 4.29.

The pumping efficiency is expected to change significantly with changing Reynolds number since it is inversely proportional to Reynolds number squared. Although the value of Reynolds number does not affect the trend of the efficiency development with time, it certainly affects the steady state value of the efficiency. The pumping efficiency decreased one order of magnitude when Reynolds number increased from Re = 1 to $\mathrm{Re} = 10$, and it decreased another order of magnitude when Reynolds number was increased to Re = 100, Figure 4.30. Since Reynolds number is the only non-dimensional parameter that represents the cylinder rotational velocity, which, in turn, is directly related to the energy input, this significant effect of Reynolds number on the efficiency is expected. The fact that the pump efficiency decreases sharply with increasing Reynolds number confirms that the viscous micropump should be restricted only to very low Reynolds numbers.

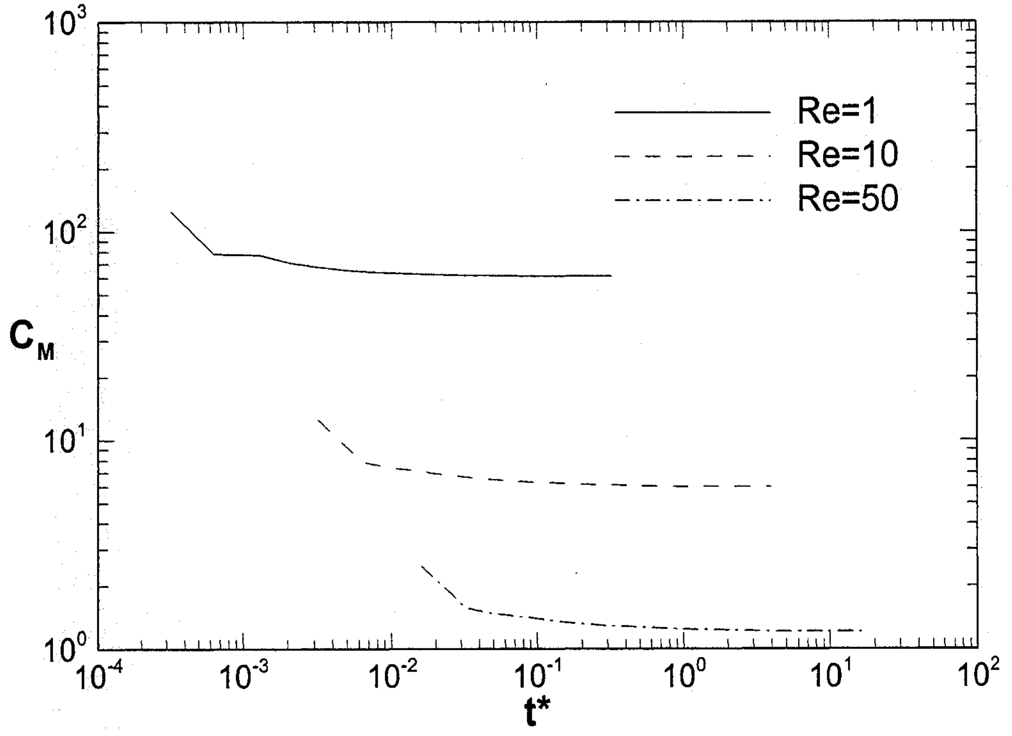

Figure 4.29: Moment coefficient vs. time at different Reynolds numbers

($S = 1.5$, $\in = 0.95$, $\Delta P^{*} = 10$).

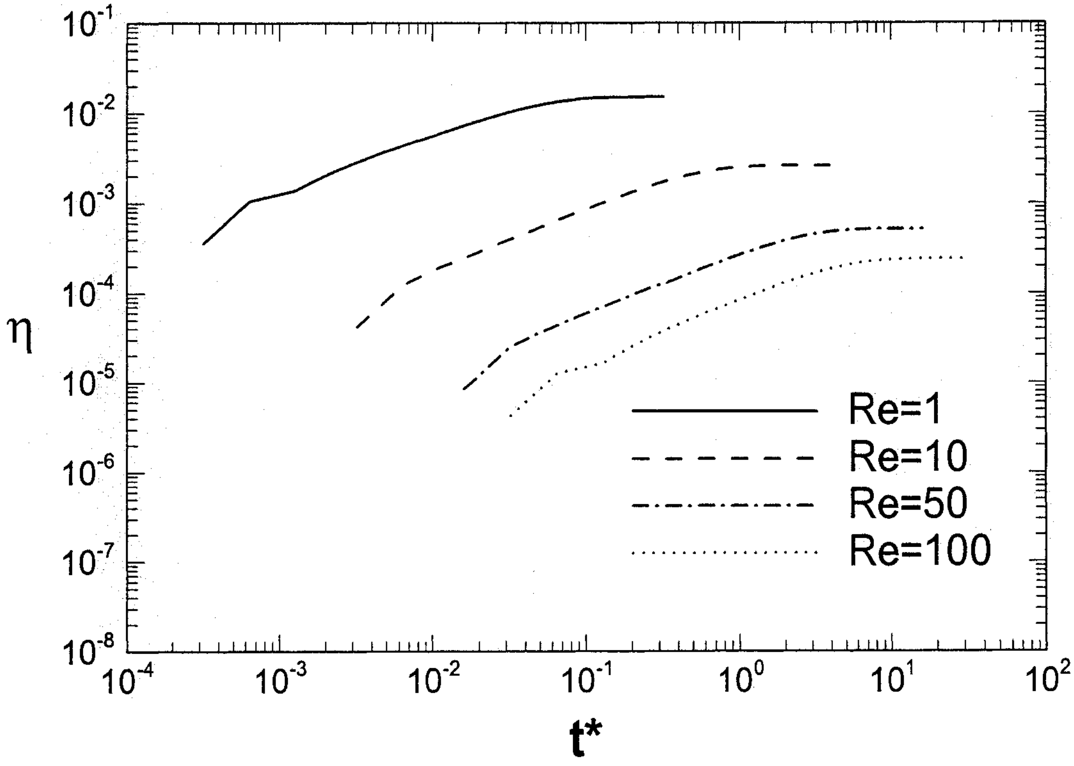

Figure 4.30: Efficiency vs. time at different Reynolds numbers

($S = 1.5$, $\in = 0.95$, $\Delta P^* = 10$).

4.5 Effect of pump load

This section will investigate the effect of the pump load on its performance. The pump load is modeled by increasing the pressure on the outlet boundary of the pump to simulate the pressure rise needed from the pump to overcome the pressure losses in the external fluid circuit. The pressure at the pump inlet is always held at zero, while the pressure at the pump outlet is varied to simulate different loads.

Figure 4.31 shows the change of the average velocity inside the micropump with time at different pump loads. It is clear that the pump average velocity decreases with increasing pump load. This was expected since any conventional pump would behave in this manner. When the pressure exceeds the maximum load the pump can deliver, a backflow occurs and the average velocity becomes negative, as is the case for the third curve "P = 10". For the case shown, the pump delivered positive flow rate initially, but eventually back flow occurred since the backpressure effect overcame the pumping effect. If the backpressure were even higher, the flow rate would have been negative from the start.

When the pump load is zero, indicating that the pump discharges into the atmosphere, two vortices exist on both sides of the cylinder at the upper wall, Figure 4.32-a. When the backpressure increases, it begins to obstruct the flow and the total mass flow rate inside the channel is reduced. Since the cylinder rotation is still the same, the fluid in the vicinity of the cylinder still gains momentum from the cylinder, but this momentum cannot be translated into a net mass flow rate due to the existing backpressure. Therefore, there is an increase in the fluid motion inside the vortices and

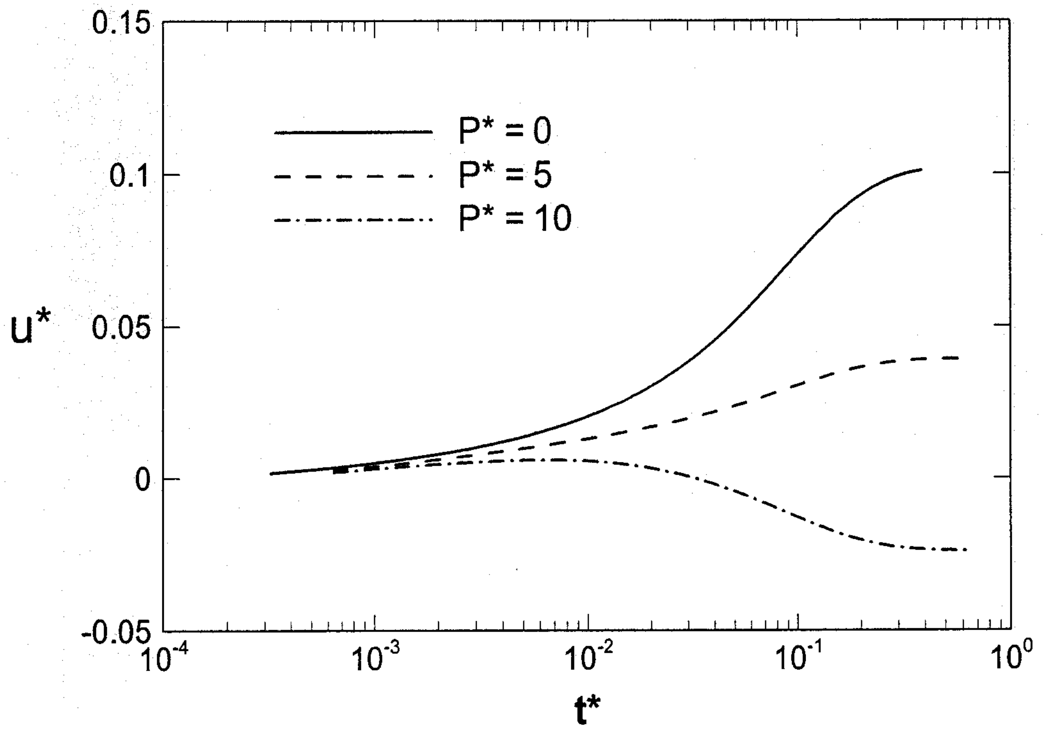

Figure 4.31: Variation of average velocity with time for different backpressures at

($S = 2$, $\epsilon = 0.95$, $Re = 1$).

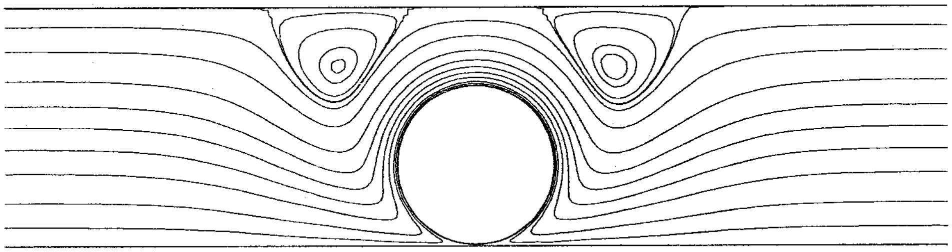

a) P*=0

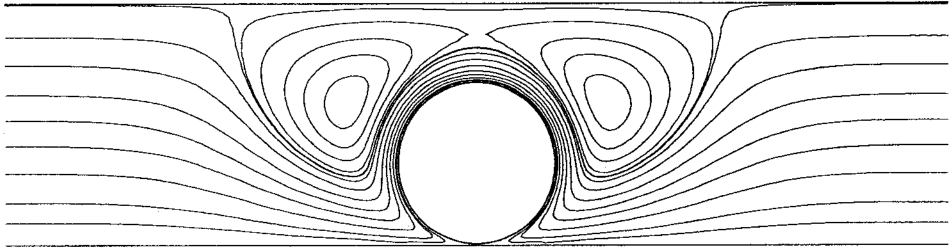

b) P*=10

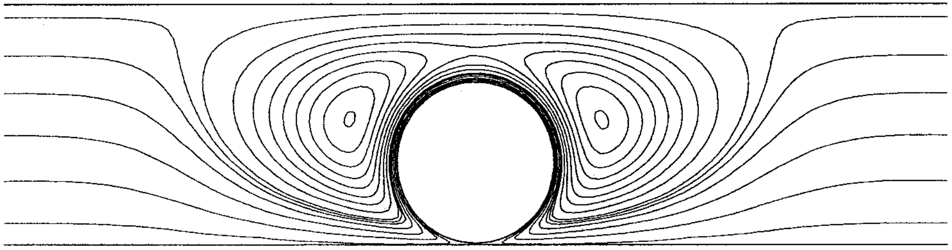

c) P*=20

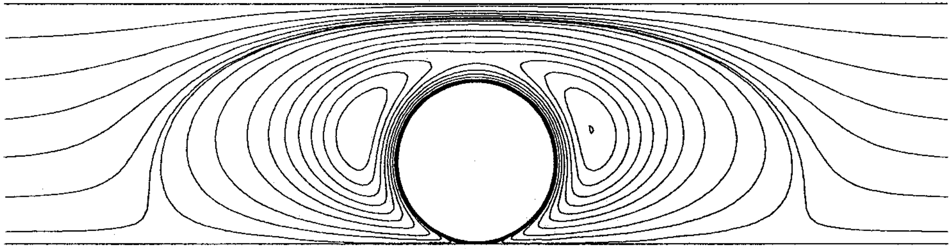

d) P*=30

Figure 4.32: Streamlines at different backpressures

(S = 1.5, ∈ = 0.95, Re = 1).

hence an increase in the vortices' sizes, Figure 4.32-b. When the backpressure increases, the two vortices still increase in size until they occupy nearly 70% of the cylinder surface. Moreover, they begin to merge together and become encircled by one big vortex that nearly occupies the whole channel in the vicinity of the cylinder, Figure 4.32-c. If the backpressure is increased even more such that backflow occurs inside the micropump, the whole situation is reversed and instead of the fluid passing in the narrow stream channel between the cylinder upper surface and the two vortices above it, the net fluid flow passes through the space between the upper wall and the vortices above the cylinder. This happens because the fluid, moving in the opposite direction of the cylinder upper surface, prefers to pass above the upper vortices where the local fluid velocity has the same direction as the net negative flow rate, Figure 4.32-d.

If the flow field for a case of high backpressure is to be monitored with time, it will be discovered that the flow field remains nearly constant from the beginning to the end. As mentioned in the previous sections, the flow always starts with two small vortices on both sides of the upper cylinder surface, and then propagates gradually towards its final form, which depends on the channel height and eccentricity. Due to the large amount of fluid circulation in the two vortices around the cylinder at steady state for the case of higher backpressure, the flow field remains nearly constant from the beginning until steady state. The only noticeable change would be the slight movement of the two vortices cores away from the cylinder surface; their final positions are at the centers of each vortex.

The drag and lift coefficients are expected to change when the backpressure is varied. The steady state value of the drag coefficient increases with increasing backpressure. This increase wasn't attributed to the pressure drag because the pressure distribution on the cylinder was nearly the same at different back pressures, Figure 4.33. Yet, the increase in the drag coefficient was due to the increase in the viscous drag as the shear stress on the cylinder upper surface increased with increasing the back pressure, Figure 4.34. This increase in the shear stress is due to the two vortices above the cylinder coming closer to its upper surface and thus increasing the velocity gradient and consequently the shear stress.

The moment coefficient is not directly related to the pressure distribution on the cylinder surface, yet it is a direct function of the shear stress. Figure 4.34 shows that the shear stress does not change on the cylinder lower surface, yet it rises slightly on the upper surface with increasing backpressure. This small rise in the shear stress raises the moment coefficient slightly.

Since the energy that the pump adds to the flow is in the form of flow energy as pressure rise, the backpressure is expected to affect the pump efficiency significantly. In the case of high backpressure, the energy addition to a fluid particle is high. However, due to the very small flow rates associated with high pressures, the overall energy addition to the fluid is small and thus the efficiency is low. On the other hand, if the backpressure is low, the overall mass flow rate will be high, but the energy addition per fluid particle will be small, thus minimizing the efficiency. The best operating conditions for the pump will be at moderate pressures, which achieve both a high-energy addition rate per fluid element and a relatively high overall flow rate. This performance coincides with the performance of any other conventional pump. Figures 4.35 shows how the pumping efficiency rises to its steady state value corresponding to the applied

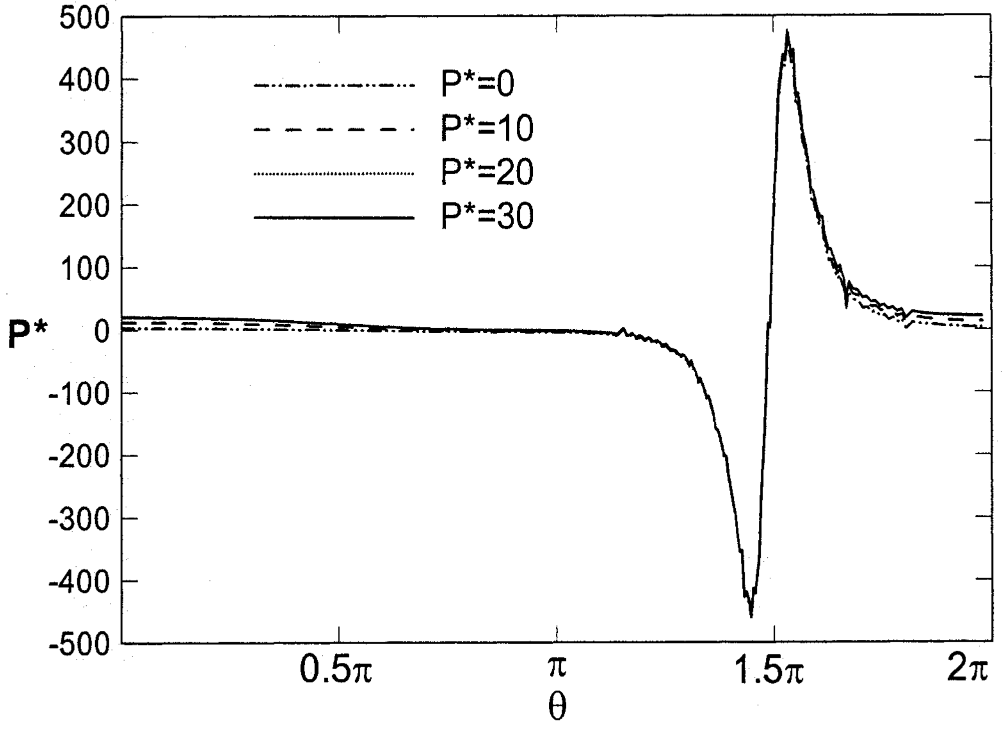

Figure 4.33: Pressure distribution on cylinder surface at different backpressures

(S = 1.5, ∈ = 0.95, Re = 1).

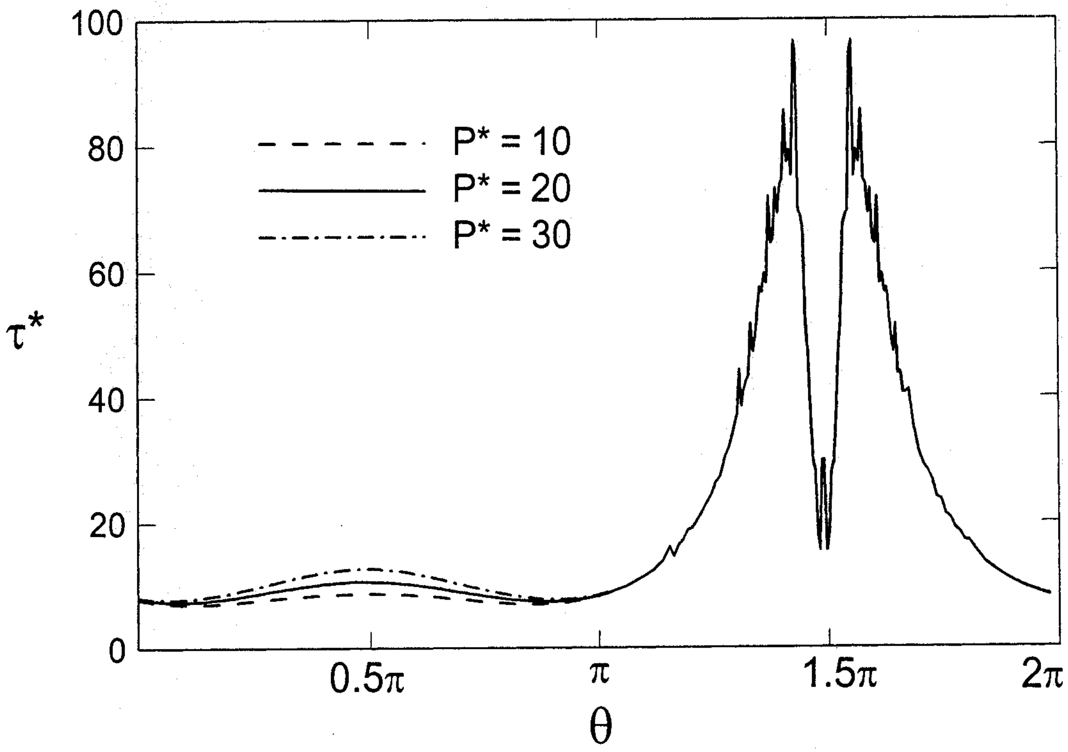

Figure 4.34: Shear stress on cylinder surface at different backpressures

($S = 1.5$, $\in = 0.95$, $Re = 1$).

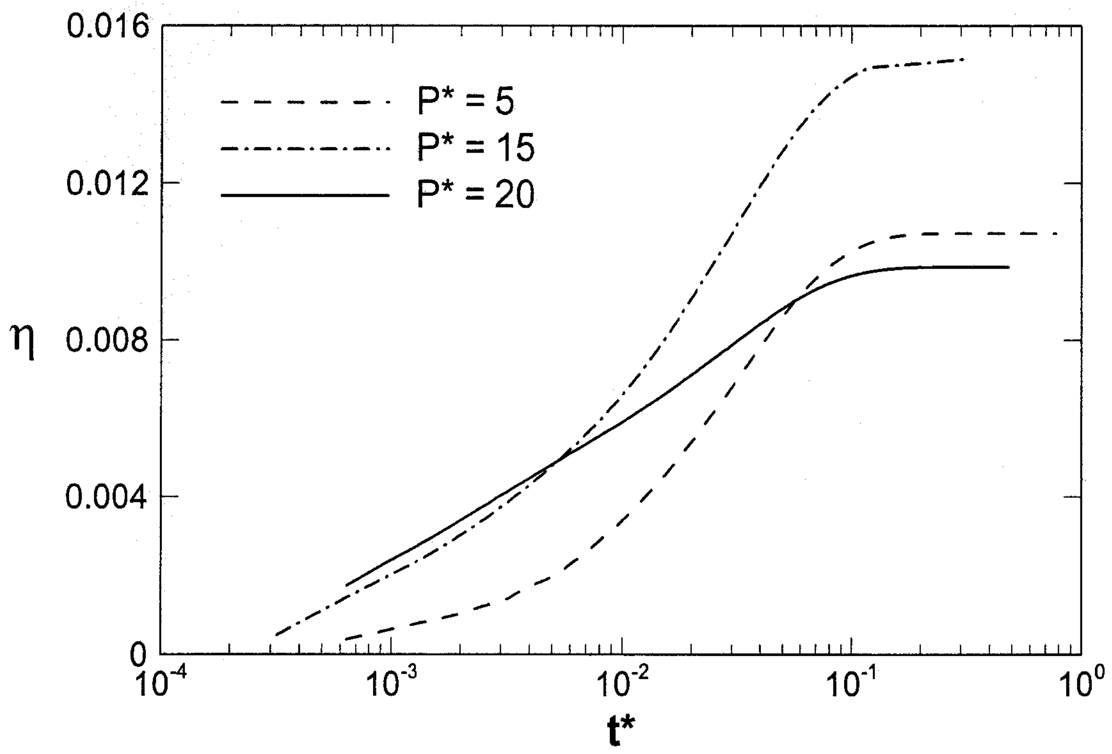

Figure 4.35: Efficiency vs. t* at different backpressures

($S = 1.5$, $\in = 0.95$, $Re = 1$)

Backpressure. Figure 4.36 shows how the efficiency changes with the backpressure at different eccentricities. The principle stated above, that the highest efficiency will be achieved at moderate values of the backpressure, is evident from the bell-shaped curves.

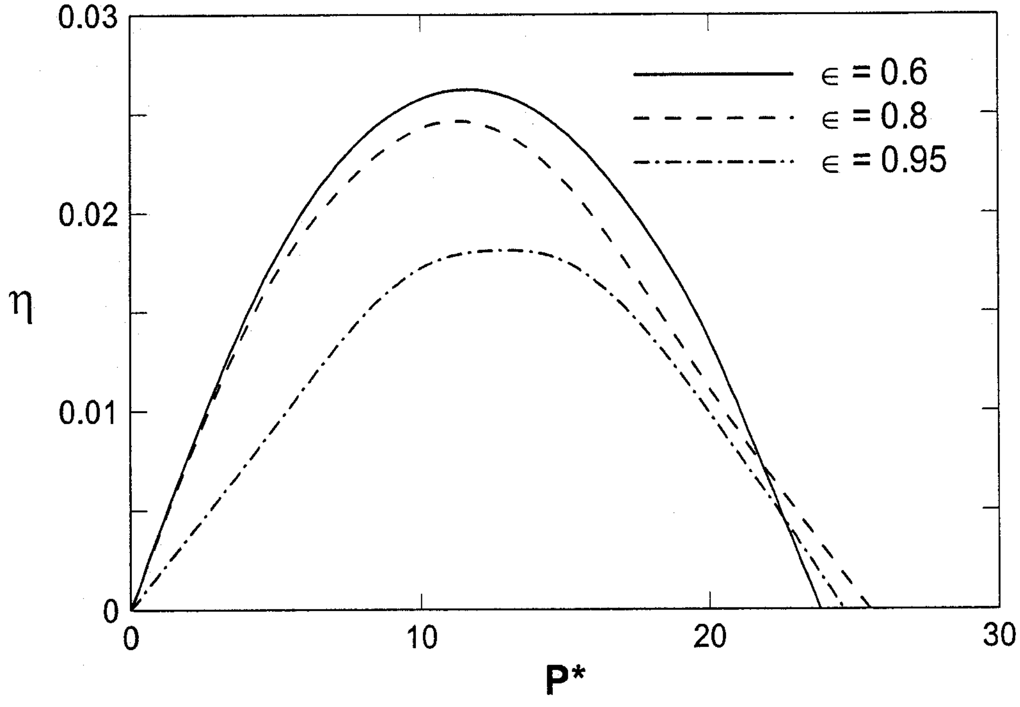

Figure 4.36: Efficiency vs. backpressure at different eccentricities

(S = 1.5, ∈ = 0.95, Re = 1).

Chapter V

Multi-rotor viscous micropump

No doubt that the simplicity of the viscous micropump is a very encouraging factor to introduce it into the field of micro pumping. Yet, the fact that the performance of the viscous micropump is still less than what is required in many of the desired applications can not be neglected. In order to enhance the performance of the viscous micropump in terms of flowrate and pressure capabilities, more than one rotor, horizontally or vertically oriented relative to each other, may be used. This is analogous to connecting two pumps or more in parallel or in series. The idea of using more than one rotor was mentioned by Zhao et al. (2002) as a case study in his work about a new descretization scheme for CFD calculations. In this chapter, different configurations that involve using two or three rotors instead of one will be investigated. These rotors will be oriented either vertically or horizontally inside the micropump channel. Four different orientations will be examined, namely, dual horizontal rotors, triple horizontal rotors, dual symmetric vertical rotors and dual 8-shaped vertical rotors. The effect of the new introduced geometrical parameters, due to the use of more than one rotor, will be the only parameters tested in this chapter. The rest of the parameters like Reynolds number and rotor eccentricity will be fixed at the values corresponding to the micropump best performance.

5.1 Dual horizontal rotor

In this section, using two rotors placed horizontally beside each other will be studied. The effect of changing the distance between the two cylinders will be the main parameter to be investigated. The other parameters will be fixed at $S = 1.5$, $\in = 0.95$ and $\mathrm{Re} = 1$.

Figure 5.1 shows the micropump with dual horizontal rotor and the mesh used for the calculation. A new geometrical parameter (λ) will be introduced to account for different horizontal distances between the two rotors. This new parameter will be defined as:

$$\lambda = \frac{L}{d} \tag{18}$$

Where L is the horizontal distance between the two cylinders as shown in Figure 5.1. The distance L was changed from 0.01 diameters up to 2 diameters in order to see the effect of changing the distance between the two rotors on the pump performance. Figure 5.2 shows the average velocity inside the channel at different rotor spacing compared with the similar curve for the single rotor pump at the same conditions. Although the trend of the flowrate development inside the pump is the same in the single and dual rotor cases, but it is clear that the dual rotor pump generate much higher flowrate as expected. This flowrate increases with increasing the distance between the two rotors up to a distance of 1.5 diameters after which the flowrate does not increase with increasing the rotors spacing. This can be explained by the fact that at this spacing, the two rotors are far from each other such that there is no interaction between the flowfields around each one of them. At such spacing, each rotor can fully work as a nearly separate pump thus nearly doubling the flowrate. At $\lambda = 2$ the flowrate is 1.72 times more than the flowrate in the case of a single rotor.

The flowfield around the two rotors changes with the separating distance between them. Figure 5.3 shows the streamlines around the two rotors at different vales of λ. For small values of λ, two big vortices and a small one exist in the flowfield. The two big vortices are located upstream of the upstream cylinder and downstream of the

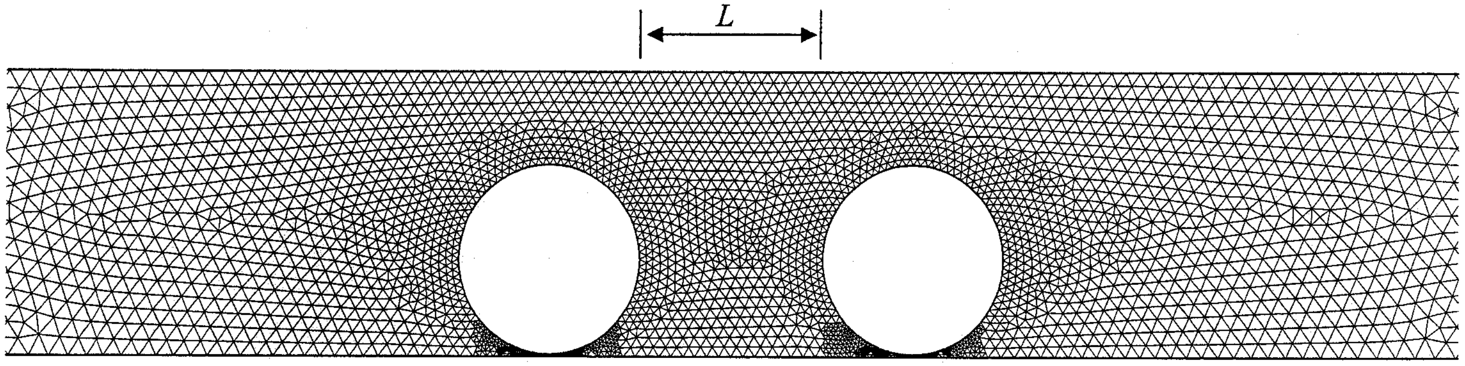

Figure 5.1: Mesh used for the dual rotor viscous micropump

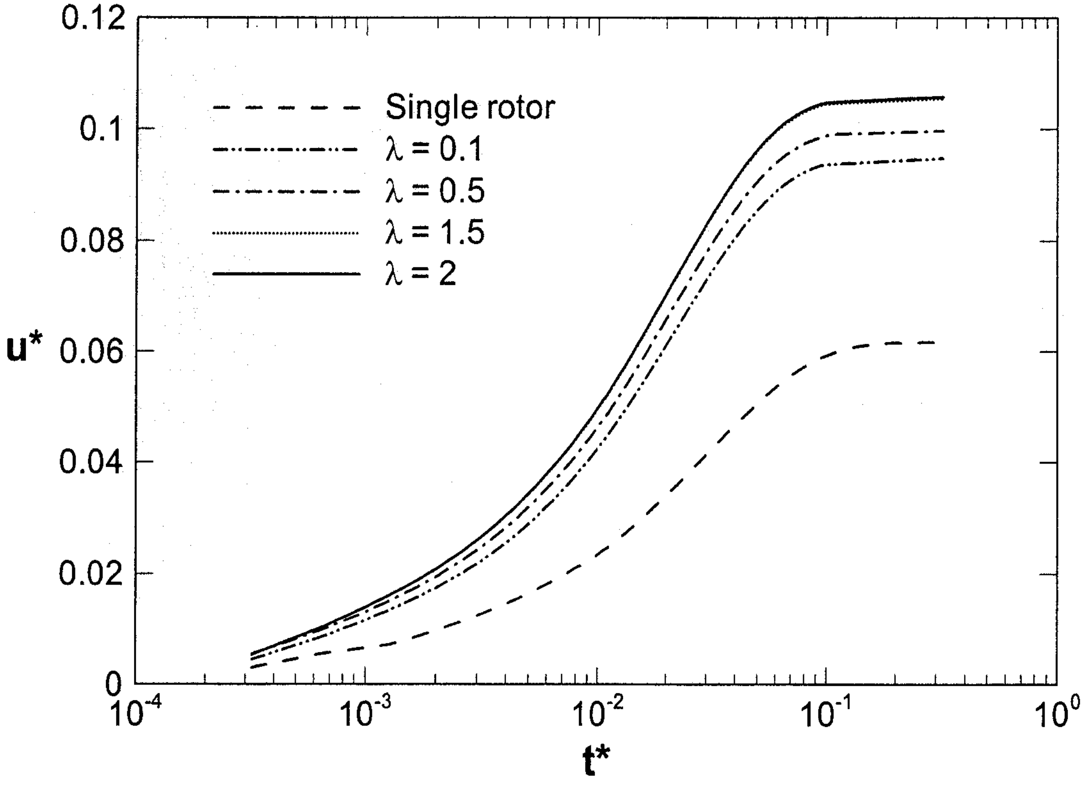

Figure 5.2: Average velocity inside the micropump at different rotor spacing

(S = 1.5, E = 0.95, P = 10, Re = 1)

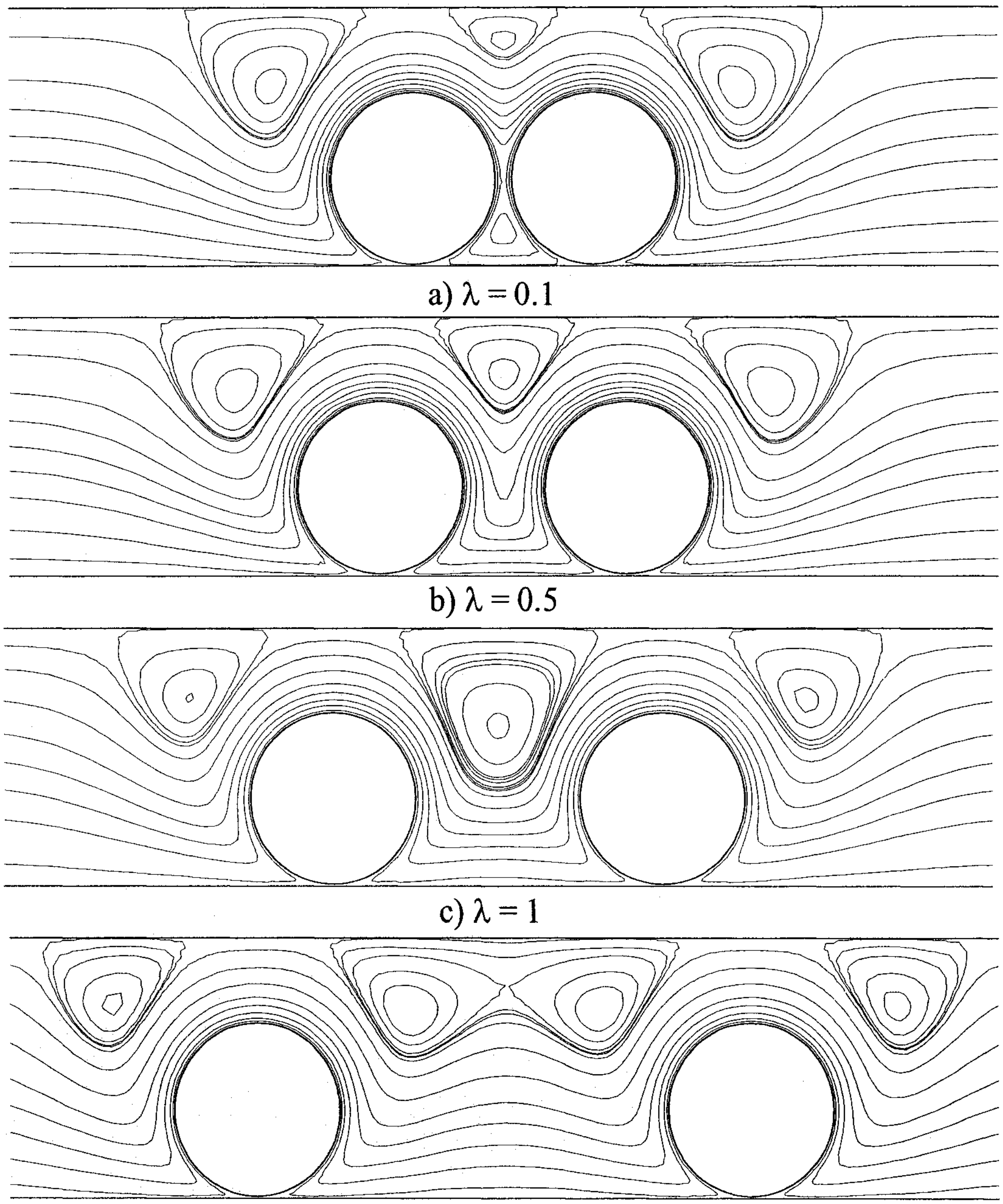

a) $\lambda = 0.1$

b) $\lambda = 0.5$

c) $\lambda = 1$

d) $\lambda = 2$

Figure 5.3: Streamlines at different λ ($S = 1.5$, $\epsilon = 0.95$, $P = 10$, $Re = 1$)

downstream cylinder as shown in Figure 5.3. The small vortex exists between the two cylinders on the upper wall. This vortex increases in size with increasing λ till it becomes two big vortices encircled together inside a bigger vortex at $\lambda = 2$.

When the development of the flowfield with time is examined, Figure 5.4, it can be seen that all the vortices start very close to the cylinders surface as in the case of the single rotor micropump. With time, all the vortices move away from the cylinders till they rest on the channel upper wall.

The drag coefficients of the first rotor (upstream rotor) and the second rotor (downstream rotor) are nearly the same in cases of high separation (λ). This is because at such big spacing, the flow around each rotor is not affected by the flow conditions on the other rotor, thus the drag coefficients are the same. At small spacing, there is a small difference in the drag coefficients on both rotors due to the interaction of the flow fields around both rotors which render each rotor a specific flow conditions around it. Figure 5.5 shows the drag coefficient of each rotor at different spacing.

The moment coefficient of the rotors is very important as it specifies the energy input to the micropump together with Reynolds number. Figure 5.6 shows the moment coefficient of each rotor at $\lambda = 0.5$. It is clear that there is no big difference in the moment coefficient of each rotor. This is due to the symmetry around the vertical centerline at low Reynolds numbers. In order to see the effect of the rotors spacing on the overall pumping performance, the moment coefficients on both the first and second rotors were added together to account for the total torque input required by the pump, Figure 5.7. It is clear from this figure that the moment coefficient does not change considerably with increasing

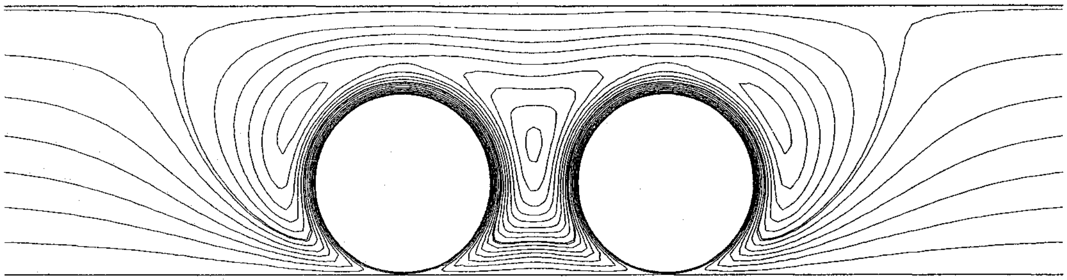

a) $t^* = 3.2$ e-3

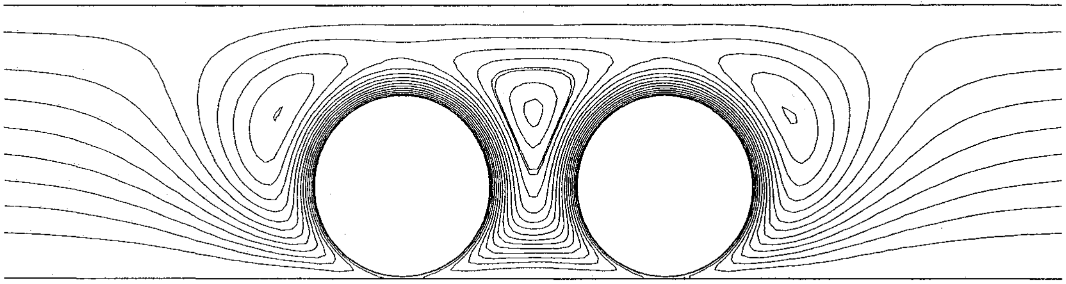

b) $t^* = 9.6$ e-3

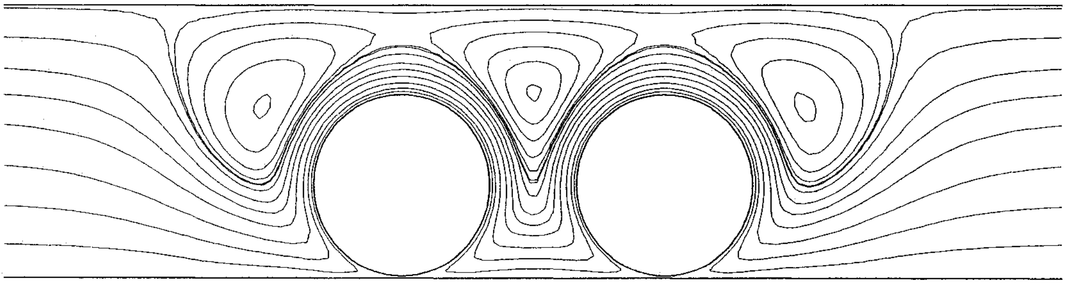

c) $t^* = 22.4$ e-3

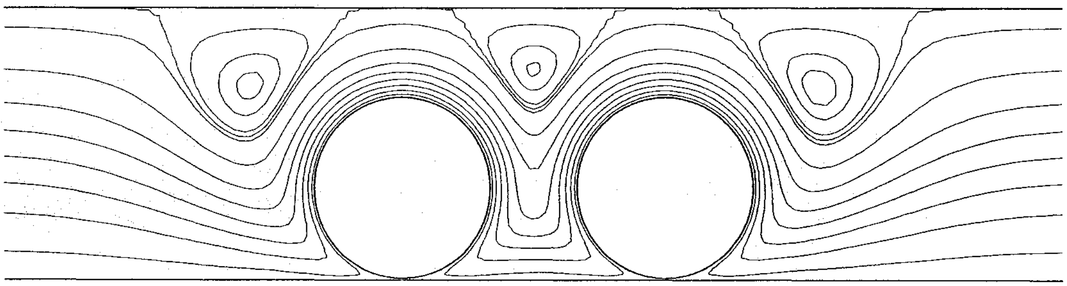

d) Steady state

Figure 5.4: Streamlines at different times at $\lambda = 0.5$

$(S = 1.5, \in = 0.95, P = 10, Re = 1)$.

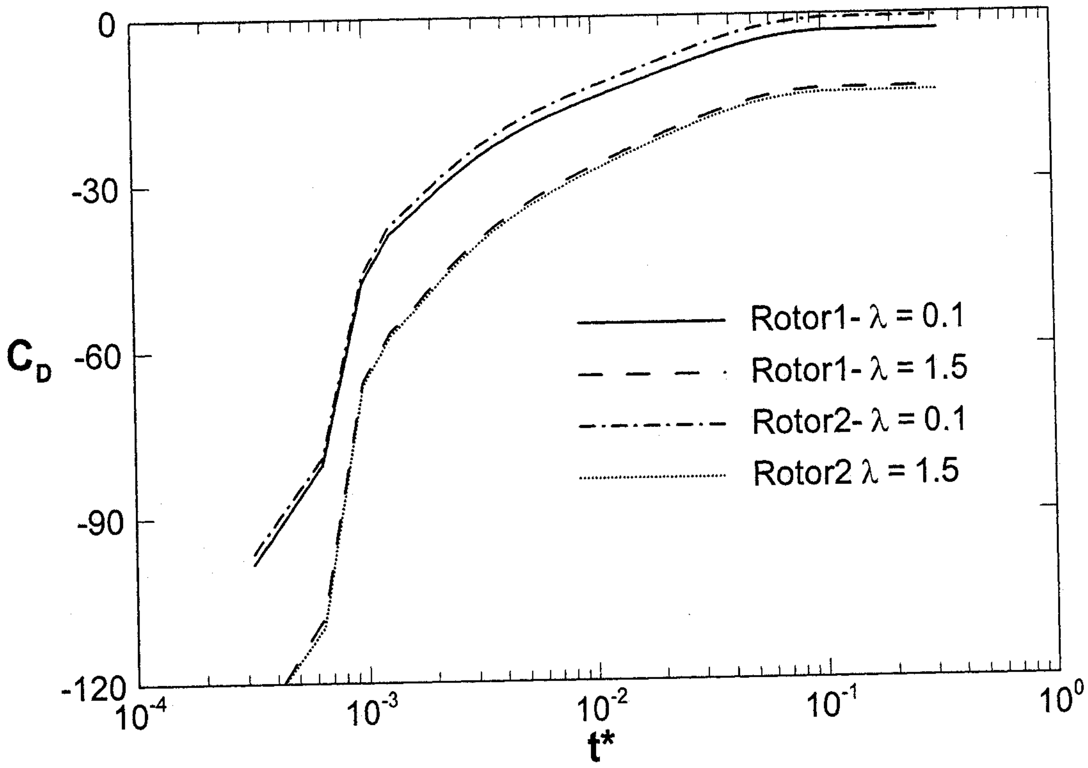

Figure 5.5: Drag coefficient on rotors 1 and 2 at different λ

($S = 1.5$, $\in = 0.95$, $P = 10$, $Re = 1$).

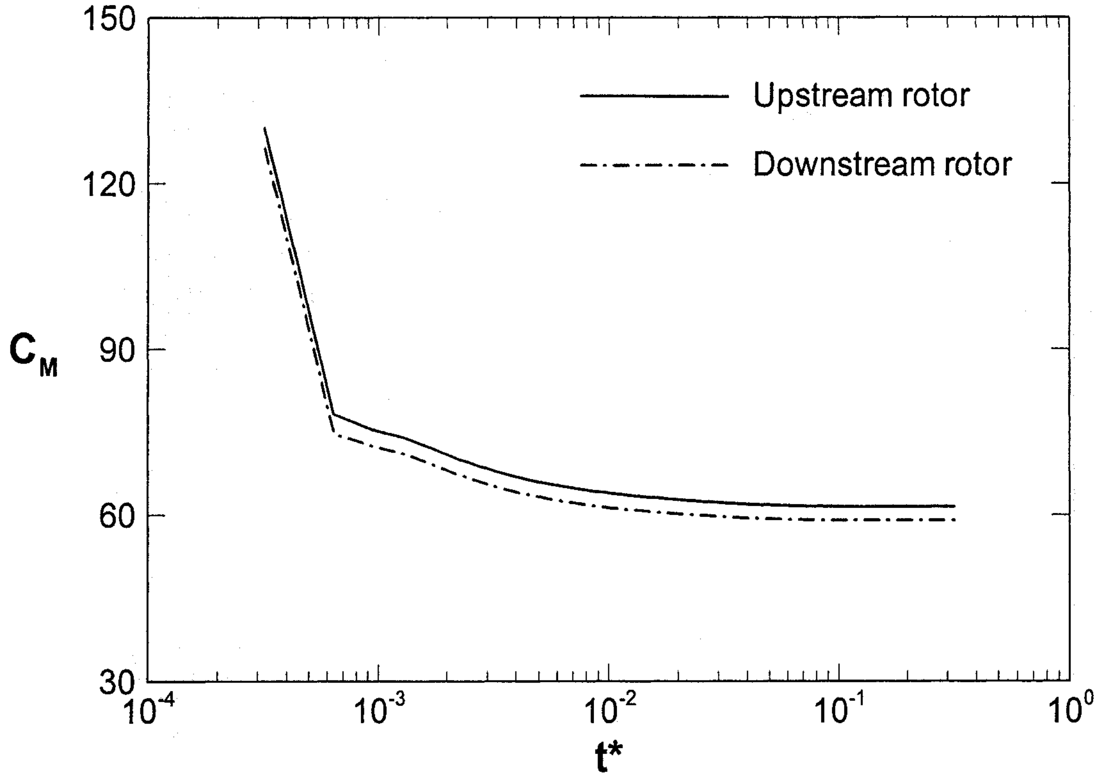

Figure 5.6: Moment coefficient on each rotor at $\lambda = 0.5$

($S = 1.5$, $\in = 0.95$, $P = 10$, $Re = 1$).

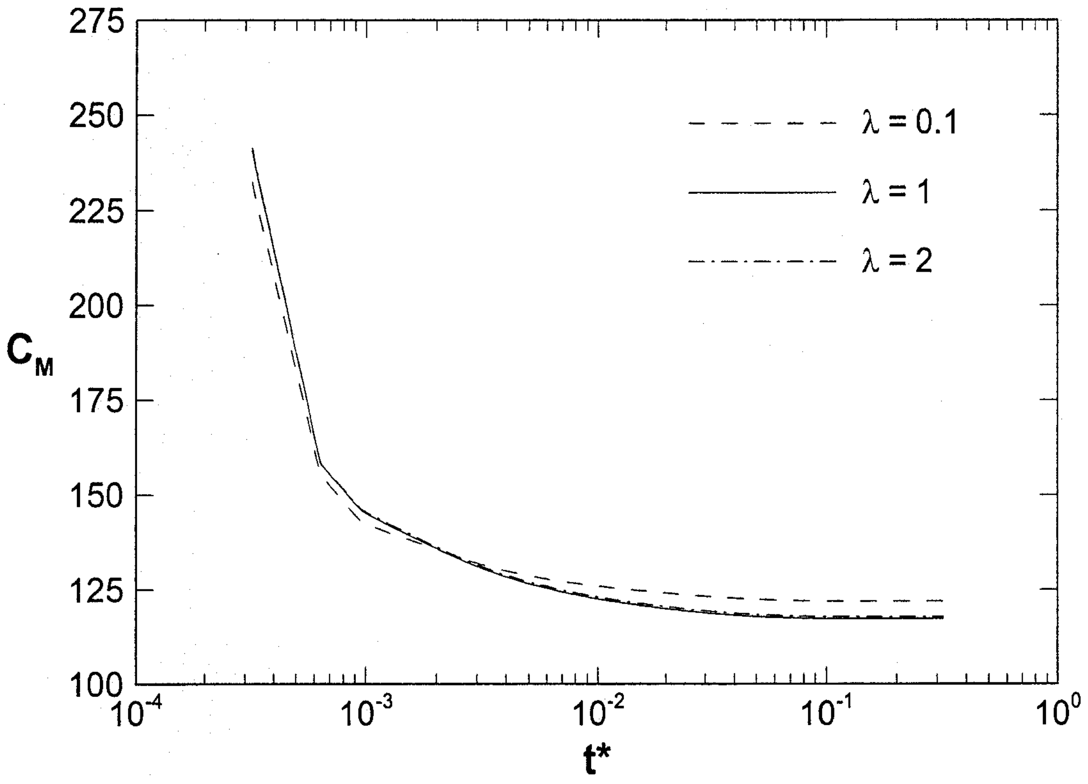

Figure 5.7: Total moment coefficient at different L

($S = 1.5$, $\in = 0.95$, $P = 10$, $Re = 1$).

the rotor spacing. Yet, it has to be noticed that the moment coefficient is higher, even if very slightly, for small values of λ. When λ is small, the two rotors are close to each other. Since the cylinders surface velocities are in opposite directions in the region in-between them, this increases the velocity gradient and hence the shear stress on the parts of the cylinders surface that are facing each other. Consequently the resisting torque and the overall moment coefficient will increase when λ is small. Based on the aforementioned information, it is expected to have higher efficiencies at larger values of λ because of the lower resisting torques in such cases. This is confirmed by Figure 5.8, which shows the development of the pumping efficiency with time at different rotor spacing. As shown in the figure the efficiency of the double rotor pump is always less than that of the single rotor pump because of the interaction between the two rotors which increases the resisting torque.

5.2 Triple horizontal rotor

Using dual rotor instead of a single rotor has increased the pump capabilities in terms of pressure and flowrate. The addition of a new third rotor is expected to further increase this enhancement in performance without the introduction of any new geometrical parameters; λ which defines the rotors spacing will still be the only additional parameter compared to the single rotor micropump. Figure 5.9 shows the steady state streamlines for single, dual and triple rotor micropump. The effect of the rotor spacing λ on the performance of the triple rotor micropump is the same as its effect in the case of the dual rotor micropump. Increasing λ reduces the degree of interaction between the different rotors allowing each one of them to act as if it is a single pump by itself. This increases

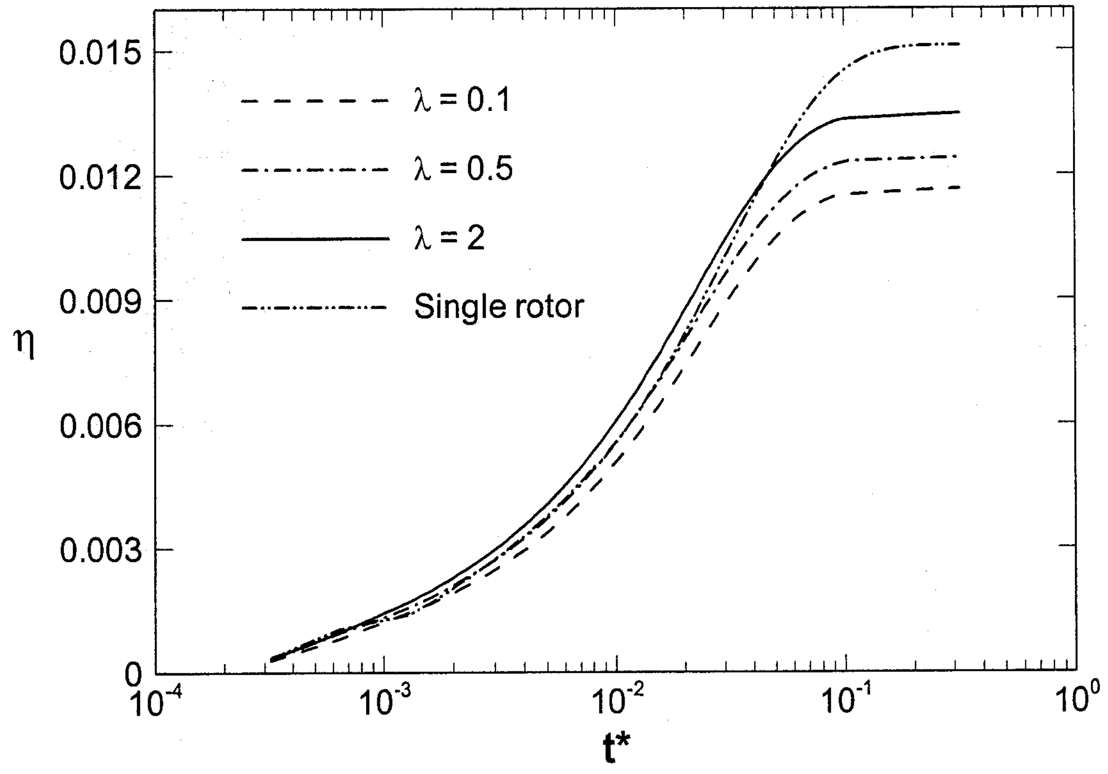

Figure 5.8: Efficiency at different rotor spacing for the dual horizontal pump ($S = 1.5$, $\in = 0.95$, $P = 10$, $Re = 1$).

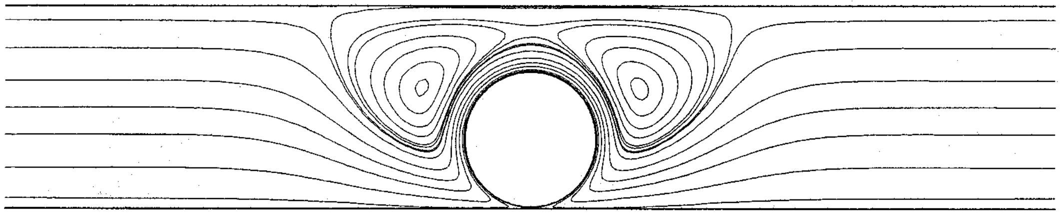

a) Single rotor

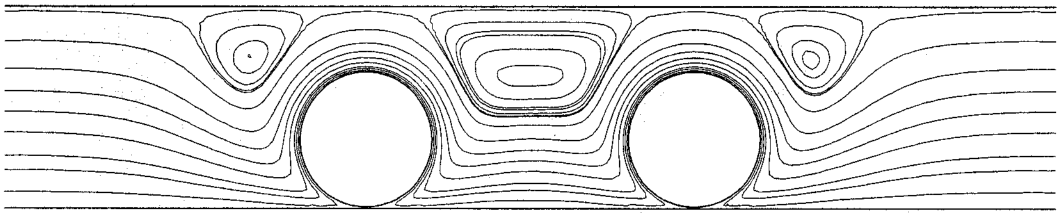

b) Dual rotor

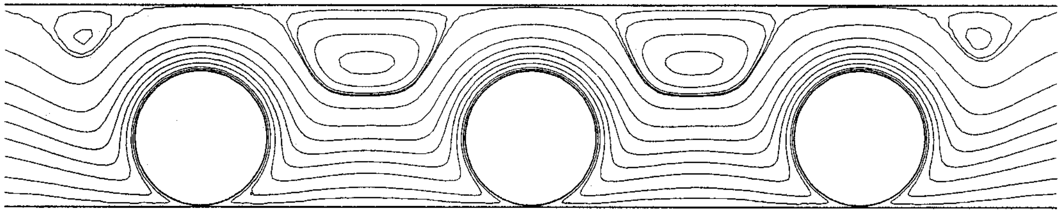

c) Triple rotor

Figure 5.9: Streamlines for single, dual horizontal and triple horizontal rotor micropump at $\lambda = 2(S = 1.5, \epsilon = 0.95, P = 10, Re = 1)$.

the pump flowrate, decreases the resisting torque and increases the efficiency. Increasing the rotor spacing beyond a certain value, which is $\lambda = 2$, has no further effect on the pump performance because at this value of λ, the interaction between the three rotors is already minimized. Figure 5.10 shows the effect of λ on the rotors total moment coefficient which does not change for $\lambda > 2$. The introduction of the third rotor has nearly tripled the value of the maximum backpressure that the micropump can sustain as shown in Figure 5.11.

5.3 Dual vertical rotor

If the two rotors are to be placed vertically instead of horizontally inside the channel, this would be analogous to attaching two pumps in parallel contrary to horizontal rotors which are analogous to attaching two pumps in series. This is expected to increase the maximum flowrate rather than increasing the maximum backpressure. There are two options for placing the two rotors vertically inside the channel. The first one is placing one rotor beside the lower wall and the other one beside the upper wall such that the pump is symmetrical about the horizontal centerline. In this configuration each rotor will rotate in separate direction namely, the lower rotor will rotate clockwise and the upper rotor will rotate counter clockwise so that they push the fluid inside the channel from left to write. The second option is to place both rotors above each other and adjacent to the lower wall so that they form the shape of number (8). In this configuration, both rotors will rotate in the same direction (clockwise) so that they push the fluid to pass through the gap between the upper rotor and the upper wall. Figure 5.12 shows these two different configurations and how the rotors are placed inside the channel in each one.

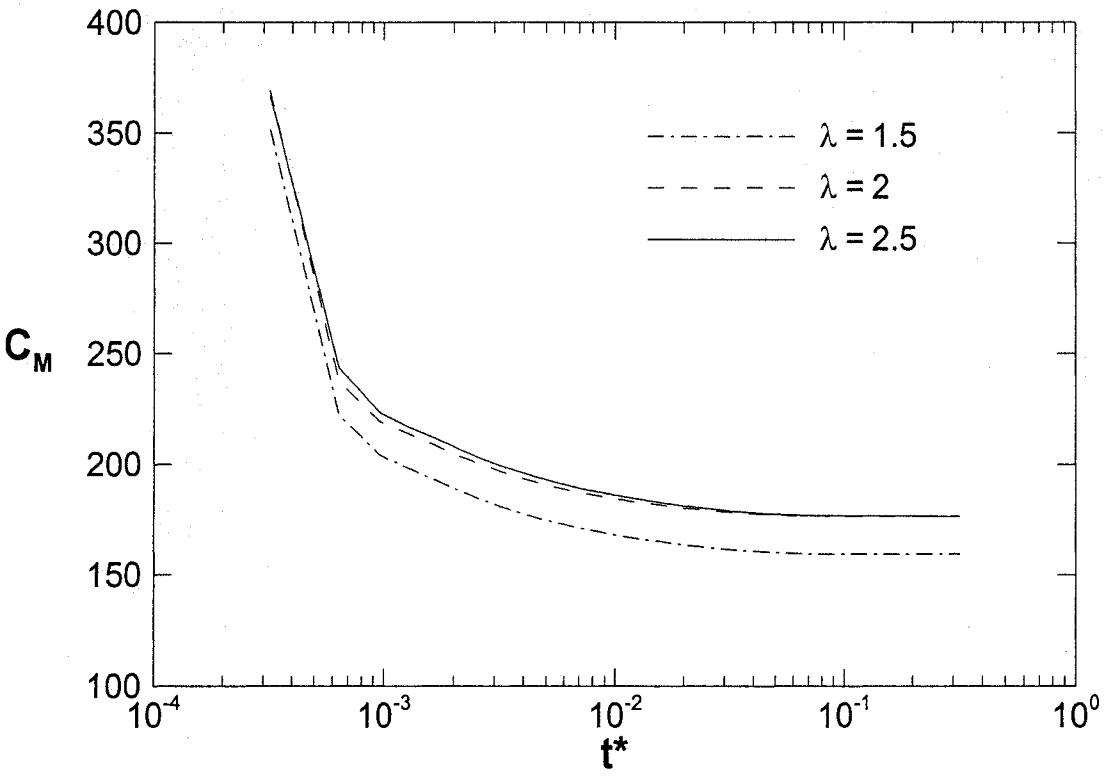

Figure 5.10: Effect of rotor spacing λ on total moment coefficient

($S = 1.5$, $\in = 0.95$, $P = 10$, $Re = 1$).

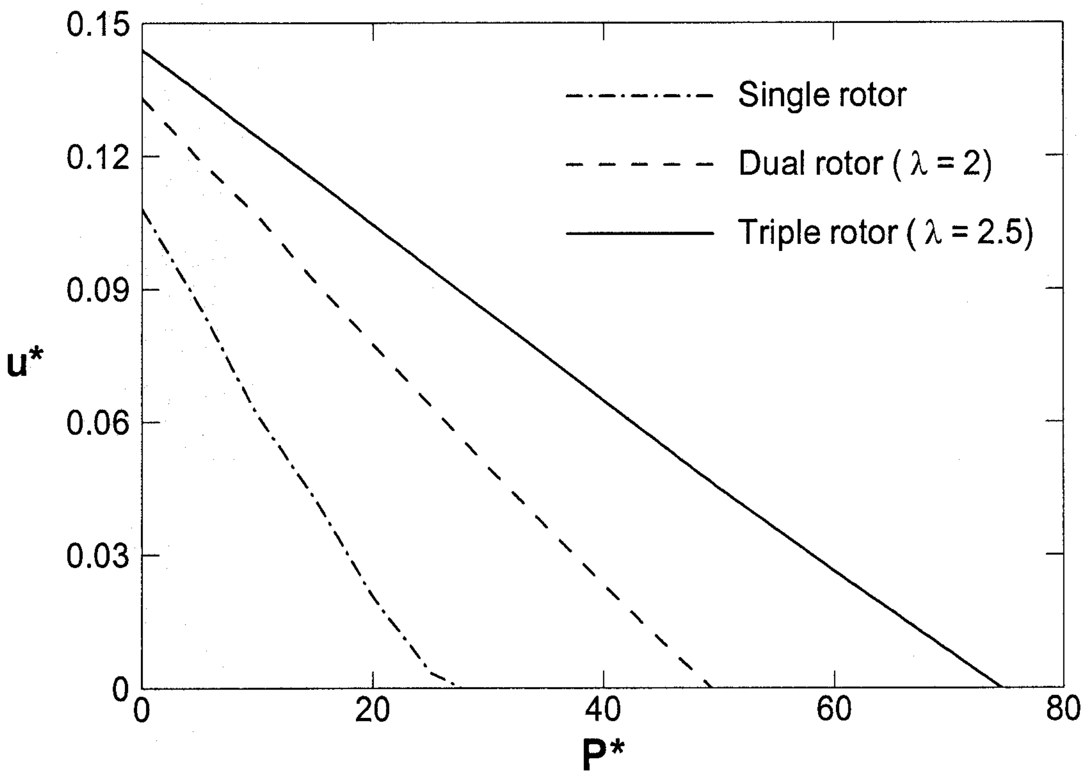

Figure 5.11: Average velocity vs. backpressure for single, dual and triple rotor micropump (S = 1.5, E = 0.95, Re = 1).

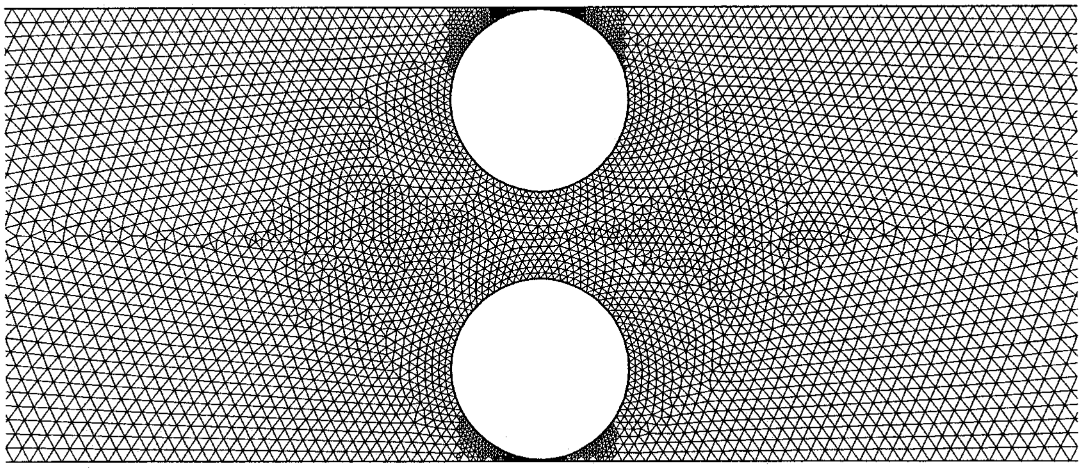

a) Symmetrical confuguration

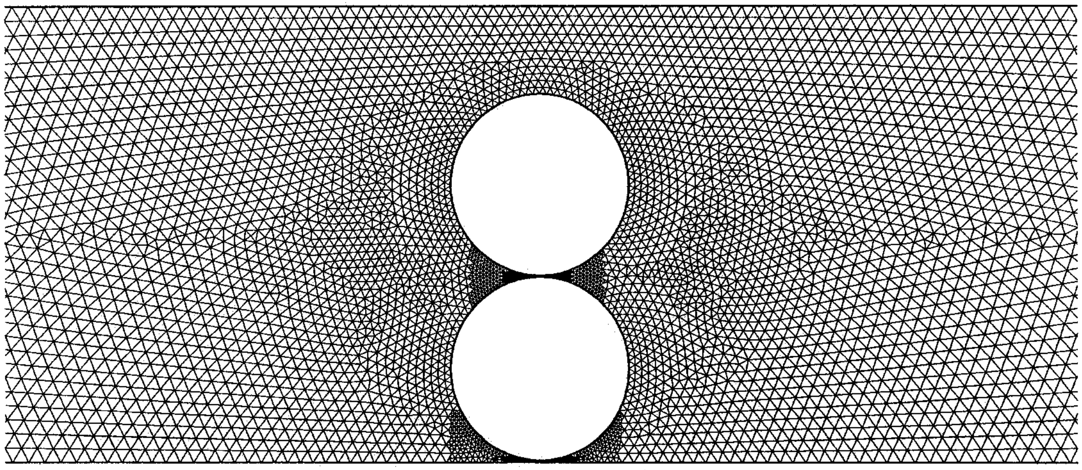

b) 8-shape configuration

Figure 5.12: The two configurations used in the vertical rotor viscous micropump.

5.3.1 Symmetrical dual vertical rotor viscous micropump

In the symmetrical dual rotor viscous micropump, no new geometrical parameters were introduced. The eccentricity, $\in$, is still the only parameter that identifies the position of each cylinder inside the channel. Yet, it has to be mentioned that in the symmetrical dual rotor configuration, the eccentricity of each cylinder is calculated separate from the other one and based on the value of *(S)* equals half the actual channel height. The streamlines in this configuration are nearly the mirror image of the streamlines in the case of the single rotor pump, Figure 5.13. Of course, there are some slight differences due to the fact that the velocity on the centre line in the present case, which corresponds to the upper wall in the single rotor case, is not zero. This is why the two vortices on the centre line in this case are smaller than the two vortices which rest on the upper wall in the single rotor micropump with the same dimensions.

Figure 5.14 shows the average velocity inside micropump for the single rotor and symmetrical dual vertical rotor for $\in = 0.95$ & 0.8. It is clear from this figure that the performance has been much enhanced by the additional rotor. The single rotor pump couldn't overcome the backpressure imposed and backflow occurred, while the dual rotor pump managed to overcome it and supple a net positive flowrate.

The drag coefficient on each rotor compared to the drag coefficient in the single rotor micropump is shown in Figure 5.15. The drag coefficient on both rotors is nearly the same because of the symmetry around the horizontal centerline. It has to be mentioned that this drag coefficient is less than that on the single rotor because of the difference in the eccentricity between both cases. Although the eccentricity is $\in = 0.95$ in both cases, but as mentioned before, in the dual rotor case the eccentricity is based on

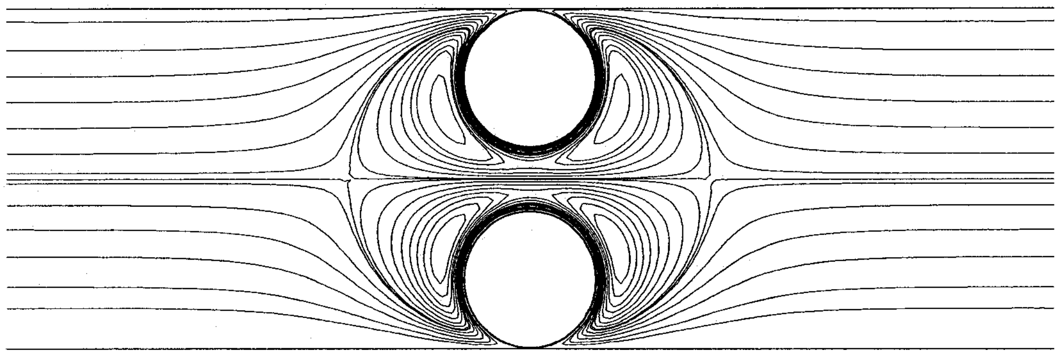

a) t* = 3.198e-3

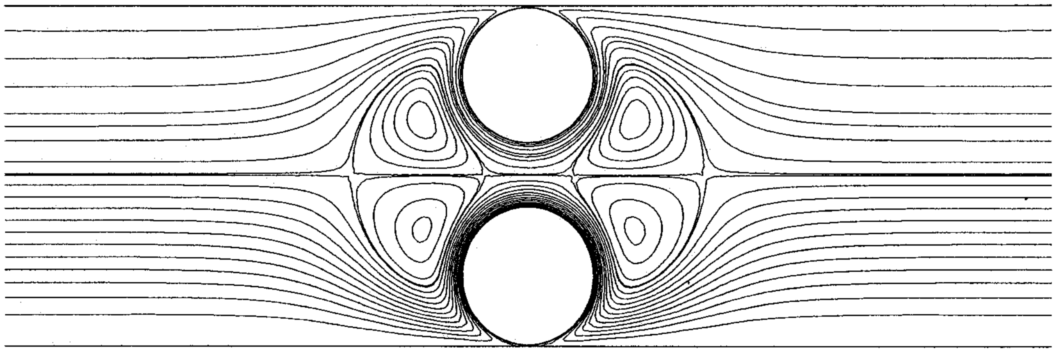

b) t* = 25.58e-3

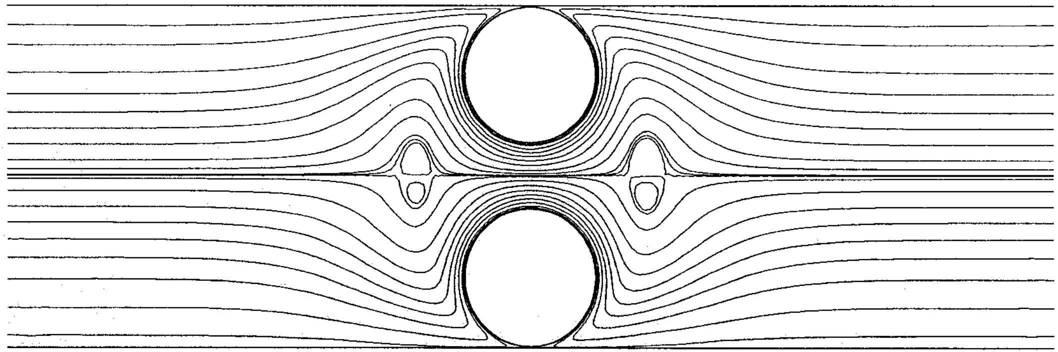

c) Steady state

Figure 5.13: Streamlines inside the symmetrical vertical rotor viscous micropump at different times (S = 2.5, $\in = 0.95$, P* = 10, Re = 1).

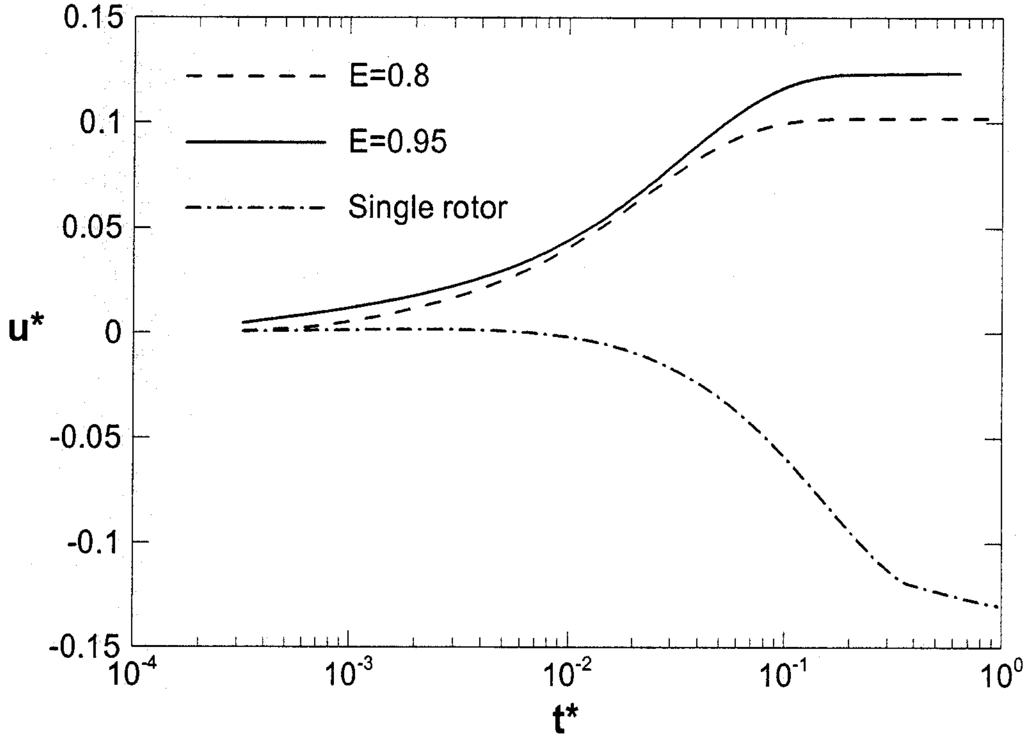

Figure 5.14: Average velocity vs. time for symmetrical vertical rotor viscous micropump (S = 2.5, P* = 10, Re = 1).

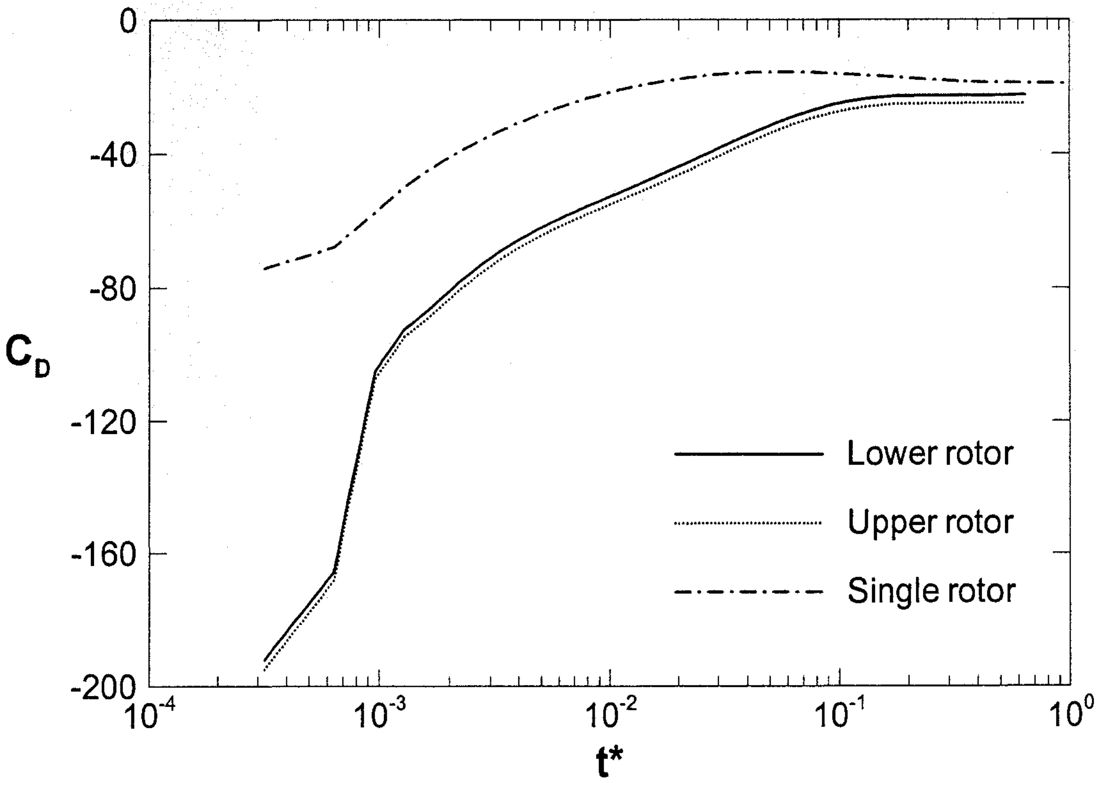

Figure 5.15: Drag coefficient on each rotor compared to the drag on the single rotor ($S = 2.5$, $\epsilon = 0.95$, $P^* = 10$, $Re = 1$).

half the channel height. This makes the actual eccentricity, based on the whole channel height bigger than 0.95.

Because the dual rotor micropump delivers much higher flowrates against higher backpressures, it is expected to have higher total moment coefficient than the single rotor case. This is confirmed by Figure 5.15 which shows the total moment coefficient (the sum of the absolute values of the moment coefficients on both rotors) for the cases where $\in = 0.95$ & $\in = 0.8$. As previously mentioned, increasing the eccentricity increases the moment coefficient, due to the increase in the shear stress on the cylinder surface, this is why the moment coefficient at $\in = 0.95$ is higher than at $\in = 0.8$ and of course, both are higher than the moment coefficient on the single rotor.

The efficiency of the symmetrical dual rotor viscous micropump is shown in Figure 5.16. The corresponding efficiency of the single rotor at the same conditions is not shown here because at this pressure backflow occurs and the efficiency is negative. It has to be mentioned that the efficiency reported in this figure (around 4% at $\in = 0.8$) is higher than all the previously studied cases of the viscous micropump. This may be due to the reduction in the velocity gradient and shear stress on the inward cylinder faces, which reduces the fluid resisting torque. Since the fluid particles on the channel centerline have the highest velocity inside the channel, unlike the case of the single rotor where the velocity of the particle at such distance form the rotor is zero, the velocity gradient will be less on the inward cylinder surfaces.

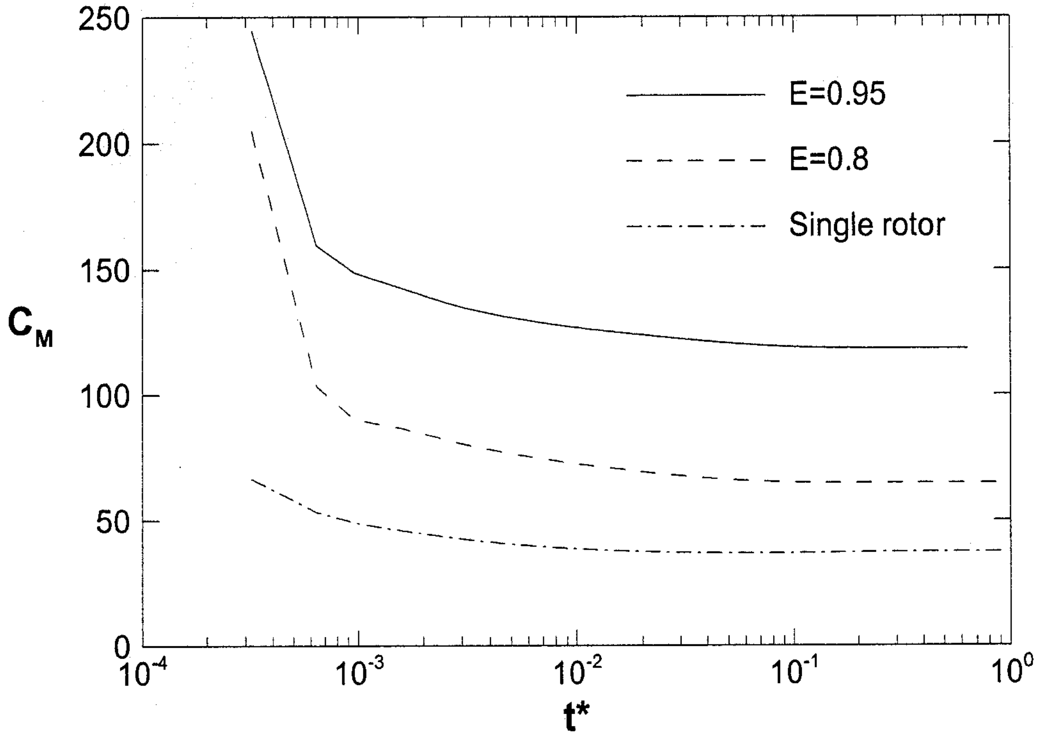

Figure 5.16: Total moment coefficient on rotors at different eccentricities
(S = 2.5, P* = 10, Re = 1)

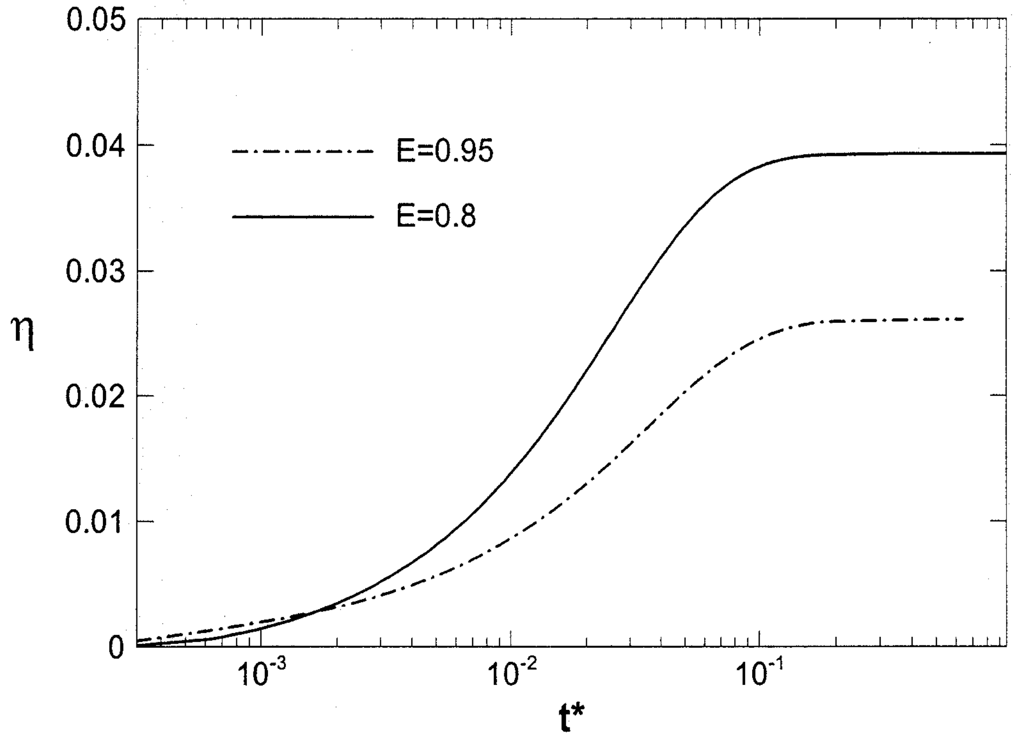

Figure 5.17: Efficiency vs. time at different eccentricities (S = 2.5, P* = 10, Re = 1).

5.3.2 8-shaped dual vertical rotor viscous micropump

In this section, dual vertical rotors are used again but instead of having a symmetrical configuration like in the previous section, the two cylinders will be placed together to form the shape of number (8) vertically placed on the lower wall, Figure 5.12-b. This configuration is not expected to achieve superior performance but it is still studied in order to further enhance our understanding of viscous micropumps. Figure 5.18 shows the streamlines for this configuration at channel heights $S = 2.5$ & $S = 3$. It is clear that at $S = 3$, the pump is unable to sustain a net flow against a pressure of $P^* = 10$, which is not very high relatively, so a backflow occurs and the flow passes from right to left in the passage between the upper wall and the big vortex around the two cylinders.

In such geometrical configuration, it is expected to have a higher resisting torque on the lower rotor because if its position between the lower wall and the upper rotor. This position helps increase the velocity gradient, and the shear stress consequently, on its lower and upper surfaces. Figure 5.19 shows the shear stress distribution on the upper and lower rotors compared to the shear stress on the single rotor. It is very clear from the figure that the shear stress is higher on the lower rotor than on the upper rotor and both are higher than the shear stress on the single rotor. Again it has to be remembered that the actual eccentricity in the dual rotor case is higher than $\in = 0.95$, this is why the shear stress value is higher than the case of the single rotor. Figure 5.20 shows the moment coefficient on the upper and lower rotors compared to the single rotor and it is clear that the resisting torque is higher on the lower rotor.

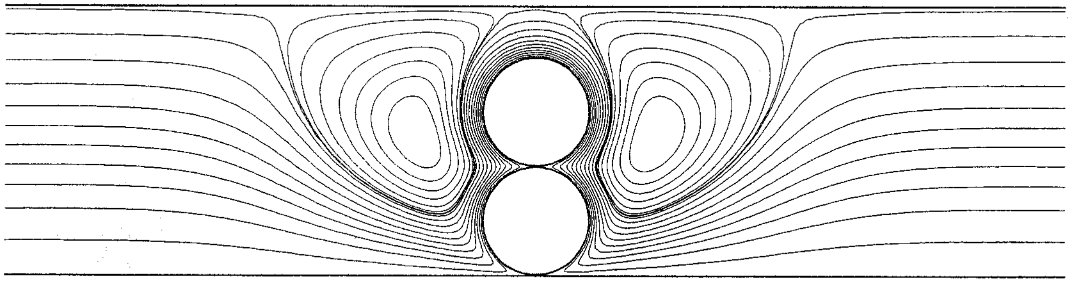

a) S=2.5

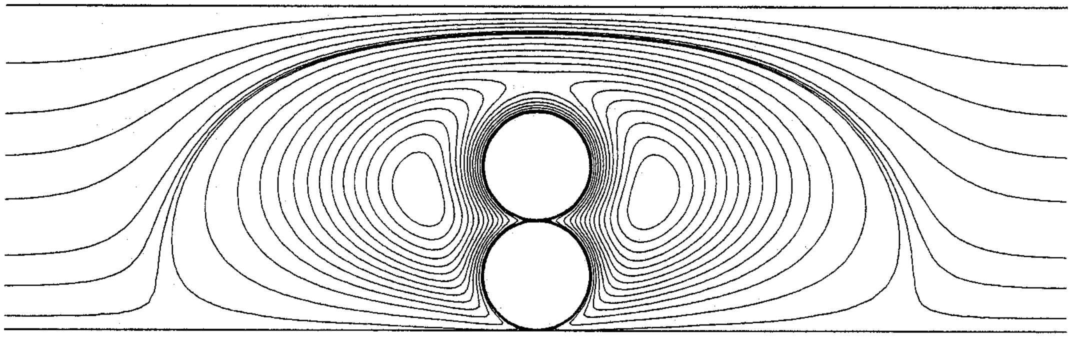

b) S=3

Figure 5.18: Stream lines in the 8-shaped dual vertical rotor micropump at different S ($\in = 0.95$, $P^* = 10$, $Re = 1$)

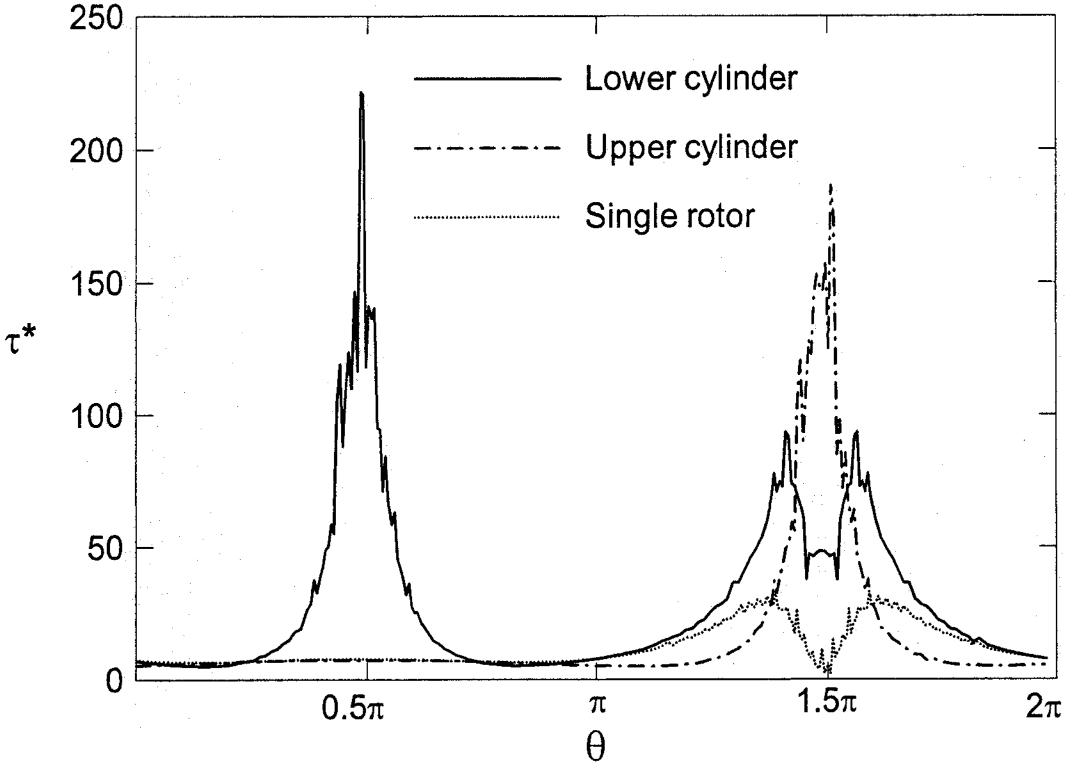

Figure 5.19: Shear stress distribution on lower and upper rotors compared to the single rotor (S = 2.5, $\in = 0.95$, P* = 10, Re = 1).

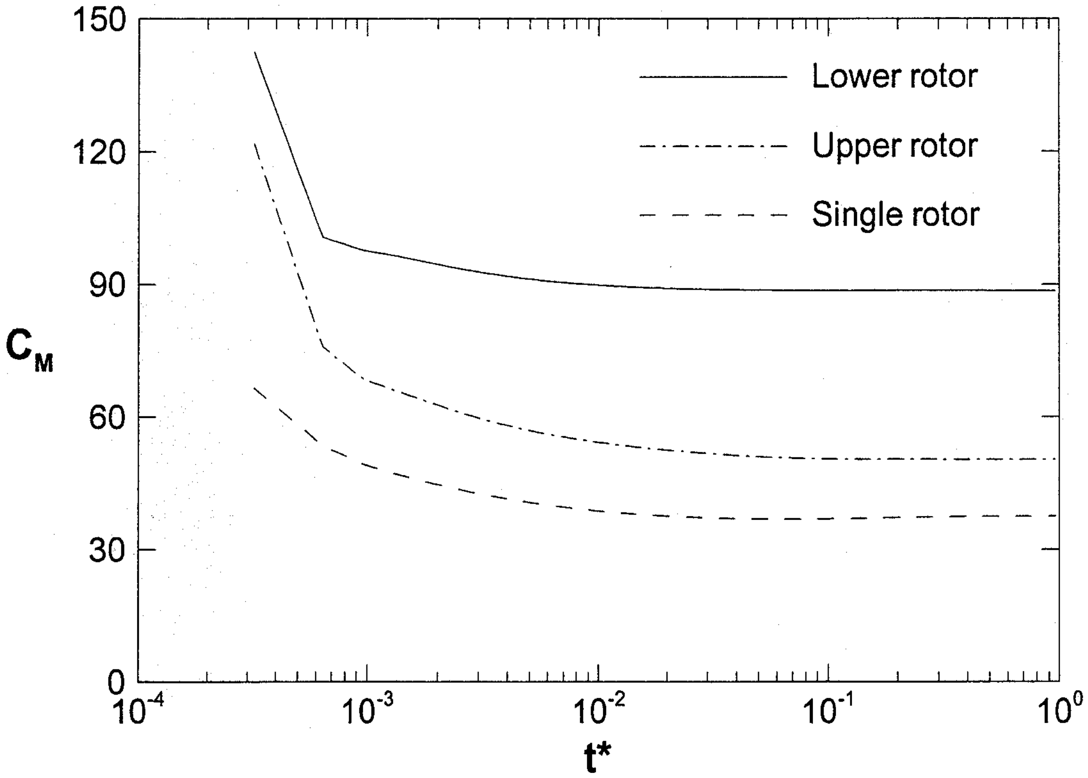

Figure 5.20: Moment coefficient on lower and upper rotors compared with the single rotor ($S = 2.5$, $\in = 0.95$, $P^* = 10$, $Re = 1$).

The efficiency of the 8-shaped dual vertical rotor is much lower than the symmetrical vertical configuration because of the increase in the resisting torque on the lower rotor as mentioned in the previous paragraph. Figure 5.21 compares the efficiency of the 8-shaped and the symmetrical micropumps at the same eccentricity, $\in = 0.95$. As shown in the figure, the efficiency of the symmetrical micropump is three times higher than the 8-shaped one.

To conclude this chapter, an overall comparison of the performance of the different configurations used in the multi-rotor viscous micropump is made in order to know what the best geometry is. Figure 5.22 shows the P*-Q curves of all the different pumps tested compared to the single rotor viscous micropump while Figure 5.23 shows the efficiency of these pumps. As clear from these figures, the symmetrical dual vertical rotor micropump achieves the best efficiency which is expected because of the reduction in the resisting torque on the rotors as explained before. This geometry also achieves the highest flowrate because it is analogous to the use of two pumps in parallel. The dual horizontal rotor has the second best efficiency and it is capable of withstanding a slightly higher backpressure than the symmetrical vertical rotor. The triple horizontal rotor, of course, supports the highest backpressure because it is analogous to three single rotor pumps connected in series, yet its efficiency is much lower than the first two efficiencies. The worst performance is of course that of the 8-shaped dual vertical rotor which has the lowest efficiency and a P*-Q curve nearly the same as the single rotor pump.

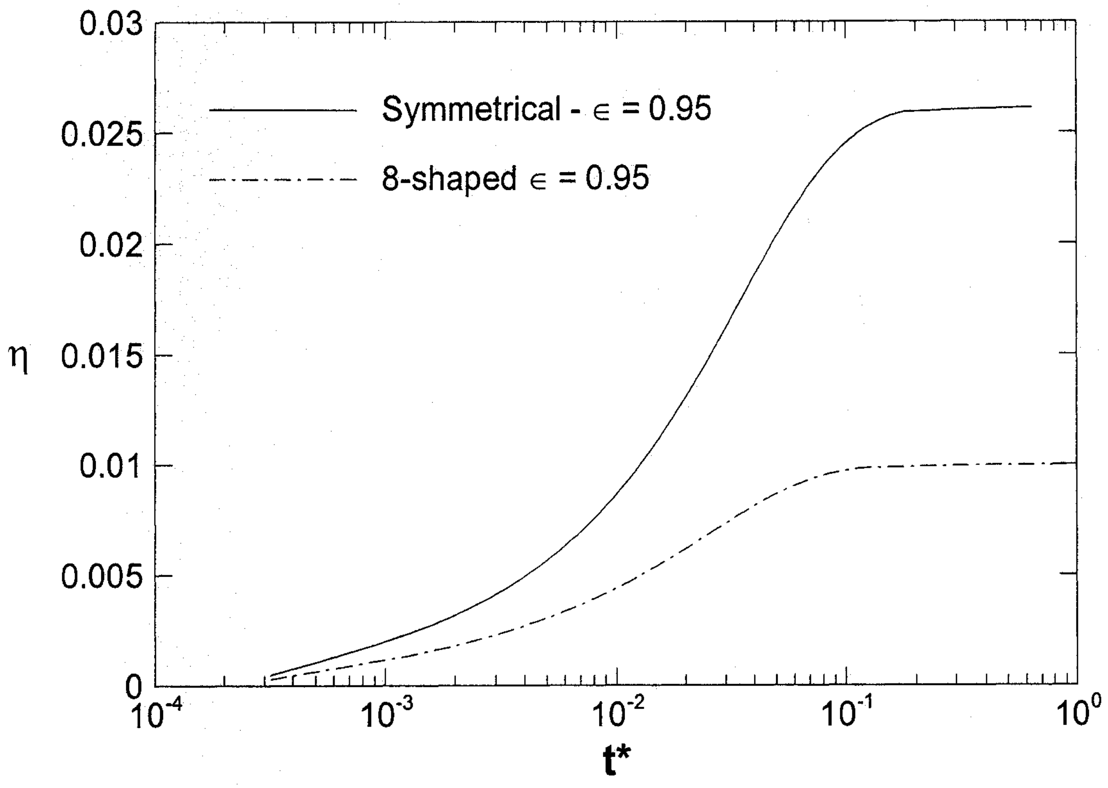

Figure 5.21: Efficiency for symmetrical and 8-shaped dual vertical rotor micropump (S = 2.5, P* = 10, Re = 1).

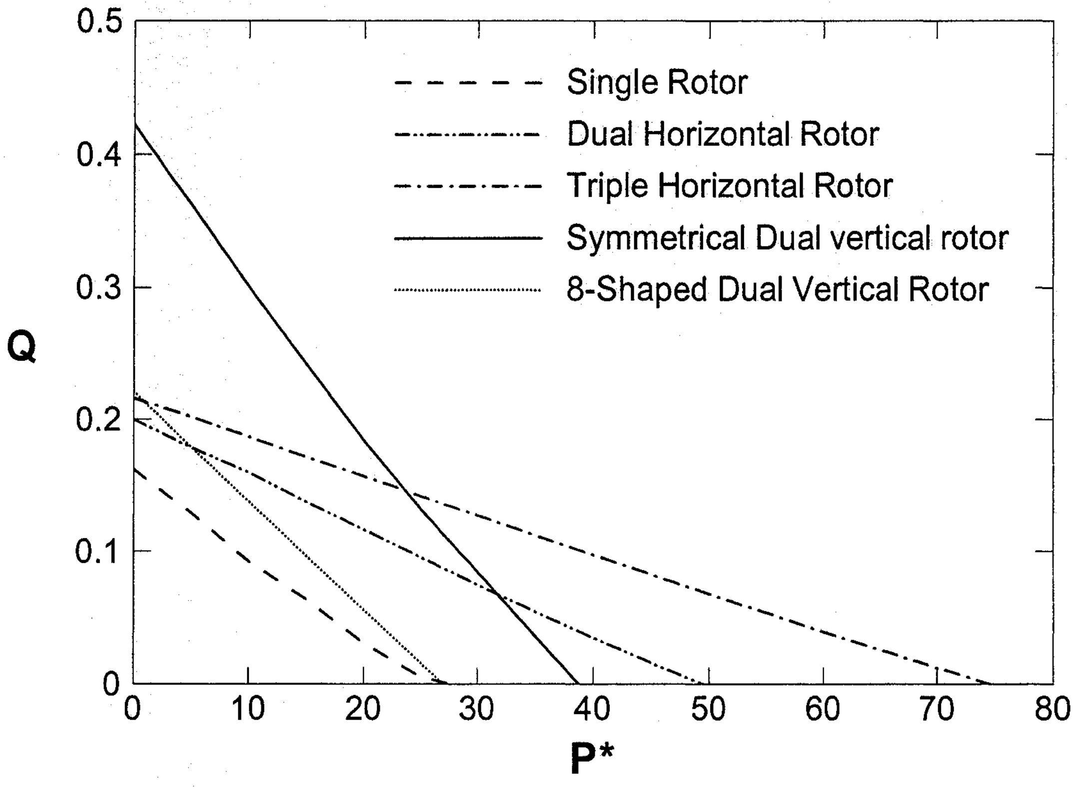

Figure 5.22: P-Q Curves for all tested multi-rotor pumps compared to the single rotor pump.

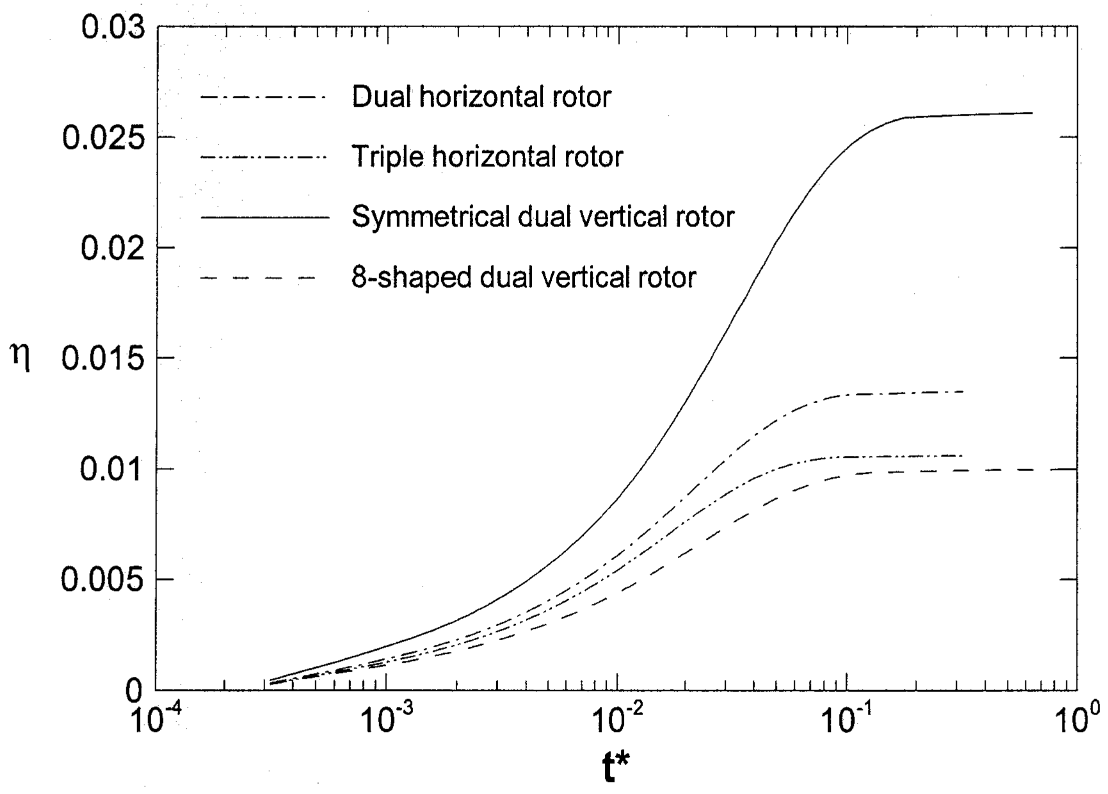

Figure 5.23: Efficiency of all multi-rotor cases tested.

Chapter VI

Conclusion and future directions

6.1 Conclusion

In the present work, the transient performance of the viscous micropump was investigated numerically. Steady state results available in the literature were reproduced and found to be in very good agreement. The effect of changing the geometrical parameters, such as the channel height and cylinder eccentricity, as well as flow parameters, such as the cylinder angular velocity and the backpressure, were studied separately. The time required for the pump to reach steady state operation was calculated, and was found to depend significantly on Reynolds number, channel height, and cylinder eccentricity. Reynolds number affected the time constant the most as it increased the time constant by two orders of magnitude when Reynolds changed from $Re = 1$ to $Re = 100$.

The rotor eccentricity was by far the most important parameter in determining the overall pump transient performance. Higher eccentricities were able to generate high backpressures, yet the pumping efficiency was lower than that for cases of lower eccentricities. Depending on the value of the backpressure and cylinder eccentricity, the pump start-up in some cases was characterized by a backflow followed by a positive flow. It was also determined that the efficiency decreased dramatically with increasing Reynolds number due to the increase in the viscous dissipation.

The development of the drag, lift, and moment coefficients was studied for different geometrical and flow conditions. The drag coefficient was always negative as expected and the pressure contribution to the drag force was always higher than the viscous force contribution, sometimes by one order of magnitude. The lift coefficient is much smaller than the drag coefficient due to the nature of the pressure distribution on the cylinder. At high Reynolds numbers the lift coefficient is much higher than its value at low Reynolds numbers, due to the semi-symmetrical nature of the flow field around the cylinder at low Re. The moment coefficient always decreased with time due to the velocity development around the cylinder, which reduced the velocity gradient, and hence the shear stress, on the cylinder surface over time.

All the micropump calculations are reported in non-dimensional quantities, which allows for the prediction of the micropump performance, regardless of the dimensions or the fluid that are used. The viscous micropump can generate pressures ranging between 0.1 Pa up to 1 kPa or more, with relatively low efficiency, depending on the micropump dimensions and the fluid properties. The average velocity of the fluid inside the micropump reached up to 11% of the cylinder surface velocity for the single rotor micropump. Based on these results, it can be said that the viscous micropump should be intended for very low flowrate applications were the efficiency is not of much importance compared to the accuracy required in delivering this small flowrate.

Multi-rotor micropumps proved to provide higher flowrates and backpressures. They simulate the use of more than one pump either in series or in parallel depending on how they are placed relative to each other inside the micropump. A new geometrical parameter, λ, arises in the case of dual and triple horizontal rotor micropump. Both the efficiency and the flowrate increase when λ increases because of the reduction in the interaction between the rotors.

In terms of performance, the symmetrical dual vertical rotor micropump achieved the best efficiency and highest flowrate, while the triple horizontal rotor achieved the highest backpressure with efficiency less than that of the single rotor. The 8-shaped dual vertical rotor viscous micro pump has the lowest efficiency with a P^*-Q curve very close to that of the single rotor micropump.

In conclusion, the concept of the viscous micropump is promising in terms of applicability and simplicity yet, it needs to be further studied in order to improve the efficiency and increase the pressure rise. The steady state and transient operation of the pump and the parameters that affect them have now been studied. Other geometries that may possess superior viscous driving characteristics need to be suggested and investigated. The simplicity of the viscous micropump design and its size flexibility provides great potential for this device in commercial applications, and is thus worthy of further study in the future.

6.2 Future directions

The field of viscous micropumps and microturbines is still in its early stages and there is a lot to be done in order to incorporate such devices into the commercial applications. For the viscous micropumps, the effect of the rotor shape whether it is square, rectangular or triangular will have a great effect on the pump performance. These shapes may prove to be more efficient in terms of overall operation even if it produced less flowrates as reported by Sen et al. (1996) or maybe they will achieve performances which suit certain applications more than the cylindrical rotor. In a matter of fact, optimum performance may even require the development of a totally new rotor geometry, whether in 2-D or 3-D, that increases the influence of viscous forces which is the main driving force in the viscous micropump. The use of more than one rotor should be more investigated parallel to the development of new rotor geometries. The rotation of all the rotors might be in the same direction or in different directions to achieve best performance.

The 3-D operation of the micro pump was examined by Decourtye et al. (1998) but only in terms of the effect of introducing the side walls of the channel. No 3-D changes to the rotor shape or the upper and lower walls were investigated although such changes will certainly affect the pump performance and may prove to give stronger pumping effect or better efficiency.

Regarding the viscous microturbine, there are only two studies available, namely, the work of Decourtye who suggested the idea and the work of Juarez et al. (2000) who studied a lot of the phenomena that will be associated in any future study relevant to viscous microturbines even though he did not mention microturbines specifically. It is needed to put a layout of the whole project of micro viscous turbines containing all the parameters, phenomena and details that need to be studied in order to pave the way for the choice of the most suitable application of such device. The layout that better covers all the aspects of this research project is divided into some main points which are outlined in the following few paragraphs.

The rotor response at different applied conditions. The output of the viscous microturbine will be the rotary motion of the rotor, which will be converted to a required useful quantity outside the turbine whether this quantity will be a generated power or a number of revolutions indicating a certain amount of fluid flow through the turbine. This rotary motion of the rotor is the response to a combination of the different applied conditions inside the turbine and it was clear from the studies mentioned in the literature review that this response might experience different types of motion depending on the applied conditions. A complete study of micro viscous turbines should include the different types of rotor motion in response to different applied conditions. The studied response should cover:

a) Type of motion (i.e. steady, oscillatory, no motion), direction of rotation and angular velocity of the rotor.

b) Viscous torque on rotor surface, output power, Efficiency and load-flow rate curve.

c) Lift and drag on the rotor.

The effect of the different parameters influencing the rotor response. According to the previous studies, it is expected that the rotor will experience different types of motion depending on the flow pattern inside the turbine. Each one of these motion types is associated with certain input conditions such as the value of Reynolds number, rotor position inside the channel, channel height…. etc. The effect of each one of these variables on the rotor response should be studied thoroughly together with the critical values of these variables at which drastic changes in the flow or rotor response occurs. It is believed that a complete study of viscous micro turbines should cover all the possible changes that might affects the response. These changes are summarized in the following points:

a) Geometrical changes such as changes in the shape of boundaries surrounding the flow field, changes in rotor shape, changes in the size of the rotor relative to the channel size or changes in the position of the rotor relative to the surrounding boundaries.

b) Changes in the upstream flow conditions such as varying Reynolds number or the velocity profile upstream of the rotor.

c) Changes in the interactions between the fluid and the solid surfaces such as the effect of slip and no-slip or penetration and no penetration boundary conditions.

d) Changes in the load applied on the rotor as well as its nature whether to be a constant load or a variable load.

Prediction of the best performing turbine geometry. It is believed that after a full study of the rotor response and the different parameters affecting the performance, the work could be extended to develop a generic code that calculates the optimum geometrical shape (for the rotor and the surrounding boundaries) and optimum flow parameters corresponding to turbine best performance. This step would be very helpful when the viscous turbine is introduced to real applications.

References

1. H. M. Badr, M. Coutanceau, S. C. R. Dennis, and C. Menard, Unsteady flow past a rotating circular cylinder at Reynolds numbers 10^3 and 10^4, *Journal of Fluid Mechanics,* vol. 220, pp. 459-484, 1990.

2. H. M. Badr and S. C. R. Dennis, Time-dependent viscous flow past an impulsively started rotating and translating circular cylinder, *Journal of Fluid Mechanics,* vol. 158, pp. 447-488, 1985.

3. C.C. Beatty, A chronology of thermal ink-jet structures, *Technical Digest IEEE Solid State Sensor and Actuator Workshop,* pp. 200-204, 1996.

4. M. Coutanceau and C. Menard, Influence of rotation on the near wake development behind an impulsively started circular cylinder, *Journal of Fluid Mechanics,* vol. 158, pp. 399, 1985.

5. R. F. Day and H. A. Stone, Lubrication analysis and boundary integral simulations of a viscous micropump, *Journal of Fluid Mechanics*, vol. 416 , pp. 197 , 2000.

6. D. Decourtye, M. Sen, and M. Gad-el-hak, Analysis of viscous micropumps and microturbines, *International Journal of CFD,* vol. 10, pp. 13-25, 1998.

7. Z. L. Demirdzic and M. Peric, Fluid flow and heat transfer test problems for non-orthogonal grids: benchmark solutions, *International Journal for Numerical Methods in Fluids,* vol. 15, pp. 329-354, 1992.

8. S. C. R. Dennis and Gau-Zu Chang, Numerical solutions for steady flow past a circular cylinder at Reynolds numbers up to 100, *Journal of Fluid Mechanics,* vol. 42, part 3, pp. 471-489, 1970.

9. J. Dopper, M. Clemens, W. Ehrfeld, S. Jung, K-P Kamper, and H. Lehr, Microgear pumps for dosing of viscous fluids, *Journal of Micromechanics and microengineering,* vol. 7, pp. 230-232, 1997.

10. J. Feng, H. H. Hu, and D. D. Joseph, Direct simulation of initial value problems for the motion of solid bodies in a Newtonian fluid-Part 1. Sedimentation, *Journal of Fluid Mechanics,* vol. 261, pp. 95-134, 1994.

11. FLUENT 6.0 user guide manual, Fluent Inc, 10 Cavendish Court, NH 0.766-1442.

12. M. Gad-el-Hak, The fluid mechanics of microdevices - the Freeman scholar lecture, *Journal of Fluids Engineering,* vol. 121, pp. 5-33, March 1999.

13. R. Hsu and P. Ganatos, The motion of a rigid body in viscous fluid bounded by a plane wall, *Journal of Fluid mechanics,* vol. 207, pp. 28-72, 1989.

14. D. B. Ingham, Steady flow past a rotating cylinder, *Computers and Fluids,* vol. 11, pp. 351-366, 1983.

15. S. K. Jordan and J. E. Fromm, Oscillatory drag, lift and torque on a circular in a uniform flow, *The Physics of Fluids,* vol. 15, n. 3, March 1972.

16. H. Juarez, R. Scott, R. Metcalfe, and B. Bagheri, Direct simulation of freely rotating cylinders in viscous flows by high-order finite element methods, *Computers and Fluids,* vol. 29, pp. 547-582, 2000.

17. V. Kalro and T. Tezduyar, 3D computation of unsteady flow past a sphere with a parallel finite element method, *Computer Methods in Applied Mechanics and Engineering,* vol. 151, pp. 267-276, 1998.

18. C. J. Kim, Microfluidics using the surface tension force in microscale, *Microfluidic Devices and Systems III, Proceedings of the SPIE,* vol. 4177, 2000.

19. T. Kimura, M. Tsutahara, and Z. Wang, Wake of a rotating circular cylinder, *AIAA Journal,* Vol. 30, n. 2, 1991.

20. R. Kurose and S. Komori, Drag and lift forces on a rotating sphere in a linear shear flow, *Journal of Fluid Mechanics,* vol. 384, pp. 183-206, 1999.

21. W. Liang and J. Liou, Flow around a rotating cylinder near a plane boundary, *Journal of the Chinese Institute of Engineers,* vol. 18, n. 1, pp. 35-50, 1995.

22. L. W. Lin, Microscale thermal bubble formation: thermophysical phenomena and applications, *Microscale Thermophysical Engineering*, vol. 2, pp. 71-85, 1998.

23. R. H. Magarvey and C. S. Maclatchy, Wakes in liquid-liquid systems, *Physics of Fluids,* vol. 4, pp. 800-805, 1961.

24. C. H. Mastrangelo and H. Becker, Microfluidics and BioMEMS, *Proceedings of SPIE,* vol. 4560, pp. 39-52, 2001.

25. N. T. Nguyen, X. Haung, and T. K. Chaun, MEMS-Micropumps: a review, *Journal of Fluids Engineering,* vol. 124, pp. 384-392, 2002.

26. S. V. Patankar, Numerical heat transfer and fluid flow, Taylor and Francis, 1980.

27. M. Sen, D. Wajerski, and M. Gad-el-Hak, A novel pump for MEMS applications, *Journal of Fluids Engineering*, vol. 118, pp. 624-627, September 1996.

28. M. C. Sharatchandra, M. Sen, and M. Gad-el-Hak, Navier-Stokes simulation of a novel viscous pump, *Transaction of the ASME, Journal of Fluids Engineering,* vol. 119, pp. 372-382, 1997.

29. M. C. Sharatchandra, M. Sen, and M. Gad-el-Hak, Thermal aspects of a novel viscous pump, *Journal of Heat Transfer,* vol. 120, pp. 99-107, 1998.

30. A. Sohankar, C. Norberg, and L. Davidson, Simulation of three-dimensional flow around a square cylinder at moderate Reynolds numbers, *Physics of Fluids,* vol. 11, n. 2, pp. 288-306, February 1999.

31. T. Tamura, T. Miyagi, and T. Kitagishi, Numerical prediction of unsteady pressures on a square cylinder with various corner shapes, *Journal of wind Engineering and Industrial Aerodynamics,* vol. 74-76, pp. 531-542, 1998.

32. D. F. Young and F. Y. Tsai, Flow characteristics in models of arterial stenoses-I. steady flow, *Journal of Biomechanics,* vol. 6, pp.395-410, 1973.

Appendix

Benchmark cases

The CFD package Fluent 6.0 has been used in the numerical simulation of the viscous micropump. In order to test the accuracy of Fluent, before the micropump problem was simulated, several benchmark cases, whose solutions are already available to a high degree of accuracy, were solved. The results were compared together. In this section, some of the benchmark cases that were used in the validation process will be presented.

Lid-driven cavity flow

The lid-driven cavity flow is a classical benchmark case that is used frequently in the validation of the in-house codes developed to solve flow problems. This benchmark case is concerned about studying the flow in a cavity induced by the translational motion of the upper plate (lid). The cavity sides might be at right angles with the top and bottom or they might be inclined at an arbitrary angle to test the accuracy of the code in non-orthogonal grid cases. This benchmark case was chosen to test the accuracy of the software in the present work as well. The results obtained using Fluent were compared with the results produced by Demirdzic et al. (1992). Of the four cases that Demirdzic studied, only the first case has been studied and its results have been reproduced by Fluent.

In the concerned case Demirdzic studied the flow inside a 45 ° inclined cavity at Reynolds number equals 1000. Reynolds number definition was based on the cavity wall length and the lid speed ($\text{Re} = \frac{U\,l}{\nu}$). In his calculations, Demirdzic used a non-uniform grid with different mesh sizes from 10x10 to 320x320 doubling the mesh size in each step. The grid was expanding symmetrically toward the centre of the cavity with an expansion ratio of 1.0096 on the finest grid. When the number of cells was increased from 160 x 160 to 320 x 320 very slight differences were noticed in the results, thus indicating a mesh independent results. Demirdzic code was run continuously till his results were accurate up to the six most significant digits. He used under-relaxation factors of 0.7-0.8 for velocities and 0.3-0.4 for pressure. The multigrid method was also used where the equations have been first solved on the coarsest grid and then interpolated to the finer grid and solved again and so forth till the equations are solved for the fines grid.

In the reproduction of the results, a 200 x 200 non-uniform grid expanding toward the centre of the cavity with the same expansion ratio of 1.0096 was used. The SIMPLE algorithm was used for solving the Navier-Stokes equations. Second order upwind and power-law descretization schemes were used in the solution with under-relaxation factors of 0.3 for the pressure and 0.5 for momentum. The multi-grid method was used in the solution in a V cycle form. The convergence criterion was set to be 10^{-4} for the normalized residuals of the continuity and momentum equations. Figures A.1 & A.2 show the stream lines inside the cavity using the second order upwind scheme and power law scheme. Figures A.3 & A.4 compare the velocity profiles on the horizontal and vertical centre lines inside the cavity from Demirdzic with those of FLUENT. It is clear how the results using power law scheme are in excellent agreement with those of Demirdzic.

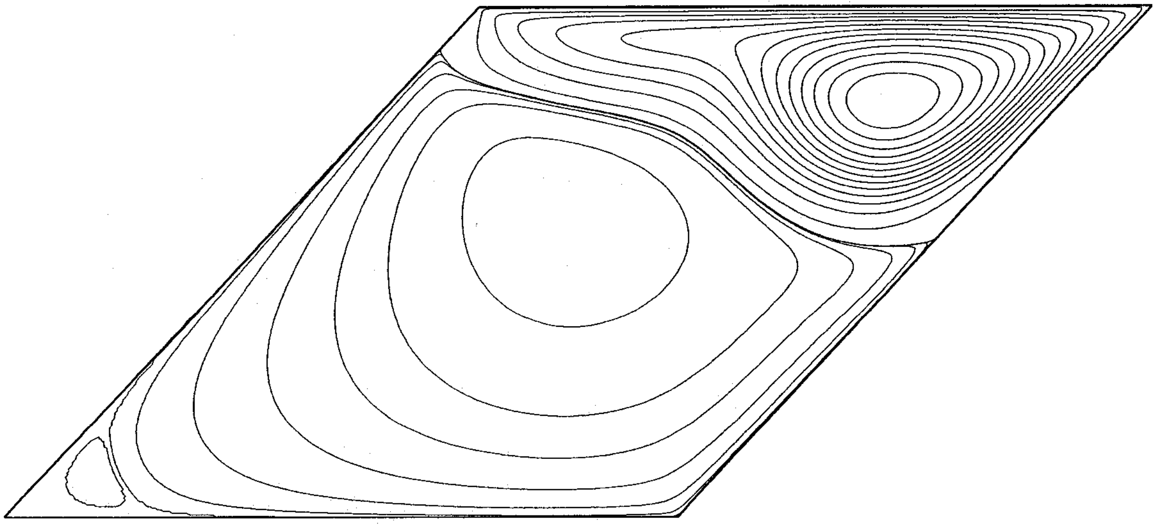

Figure A.1: Stream lines Re = 1000 β = 45 Second order upwind scheme.

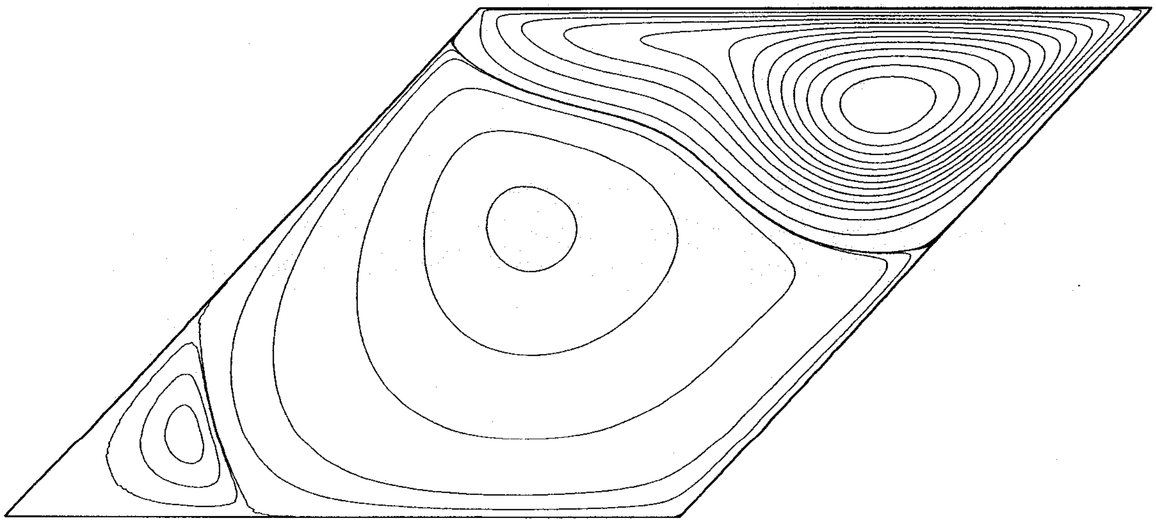

Figure A.2: Stream lines Re = 1000 β = 45 Power law scheme.

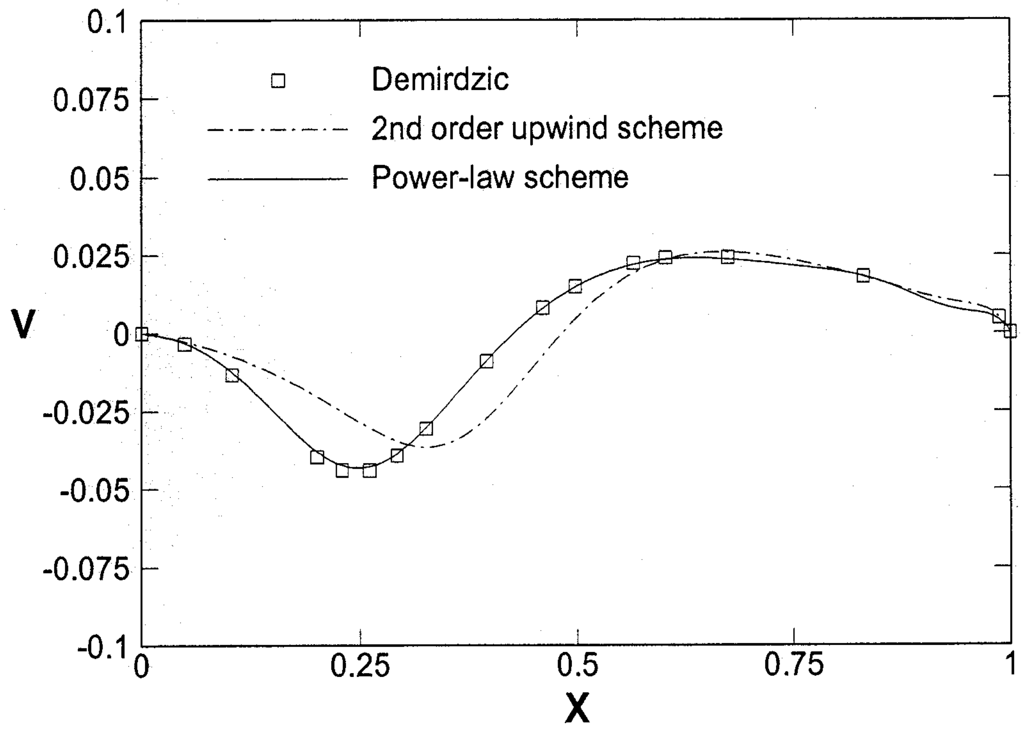

Figure A.3: V velocity component on the horizontal centre line.

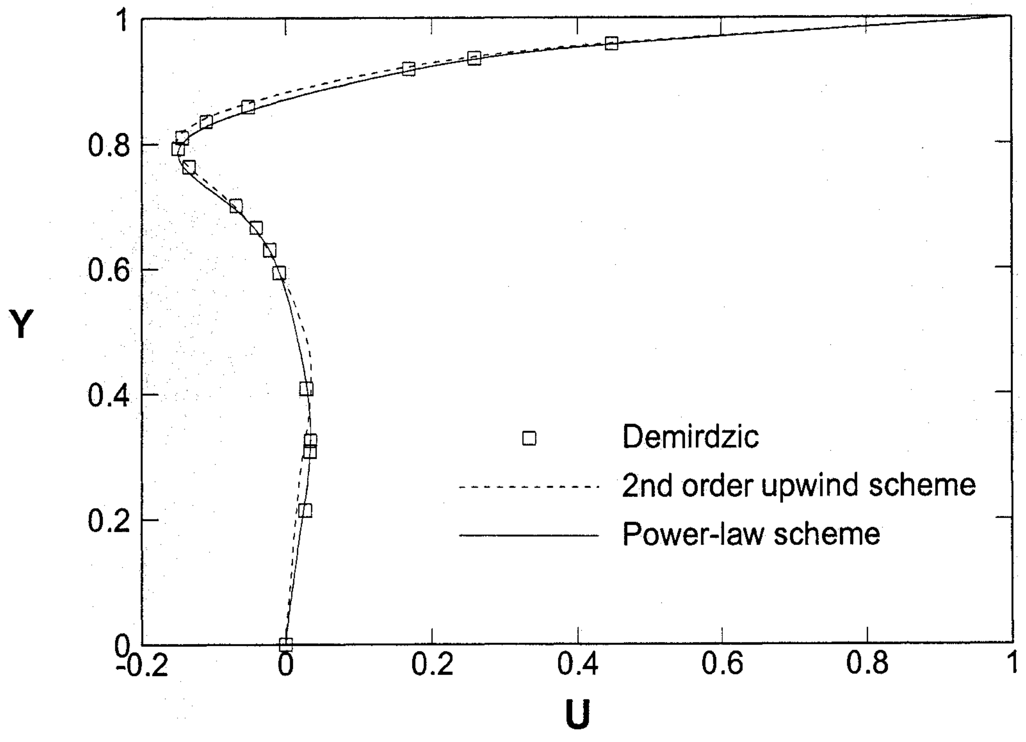

Figure A.4: U velocity on the vertical centre line.

Laminar flow through a tube with a constriction

The second case we studied to validate the software was laminar flow inside a tube with a constriction. The reference results were taken from Young et al. (1973) where he studied experimentally steady flow inside a pipe with both axis-symmetric and non axis-symmetric constrictions. The shape of the constriction in the axis-symmetric cases was specified as a cosine curve in the form

$$\frac{R}{R_0} = 1 - \frac{\delta}{2R_0}(1 + \cos\frac{\pi z}{Z_0})$$

The length of the constriction is 2 Z_0 and its height δ were varied to give different relative flow geometries, Figure A.5.

The case studied had the following dimensions: R_0 = 0.372 in, δ = 0.248 in, $Z_o / R_o = 4$. Since the flow is axis-symmetric, only the upper half of the pipe was simulated. A non-uniform 20 x 160 grid was used with the mesh size smaller in the constriction area and near the walls and expanding toward the pipe inlet and outlet. The SIMPLE algorithm with the second order upwind scheme was used to reproduce the data . Under relaxation factors were 0.3 for pressure and 0.7 for momentum. A V-cycle multi-grid was used to enhance conversion. The convergence criterion was set to 10^{-3} for the scaled continuity and momentum residuals. The position of the separation point and re-attachment points of the flow behind the constriction were taken as the criteria for the comparison between the analytical and experimental solutions. The results of the comparison are shown table A.1.

Table A.1: Experimental and analytical values of the separation and re-attachment distances

Re	Separation point		Re-attachment point	
	Experimental	Analytical	Experimental	Analytical
50	0.33	0.33	2.28	2.14
100	0.34	0.33	4.19	4.02

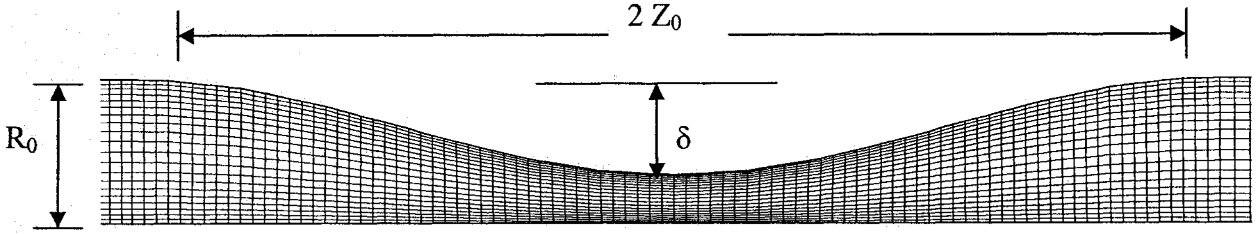

Figure A.5: Mesh of the constriction part in the pipe

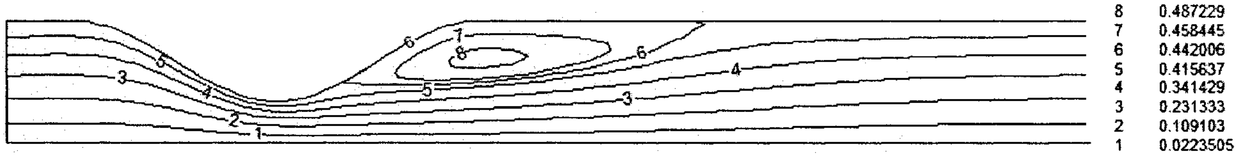

Figure A.6: Stream lines near the constriction (drawing not to scale)